

Fiber-optic sensor cable for simultaneous distributed measurement of multiple physical quantities.

Bašić, Petar

Doctoral thesis / Disertacija

2019

Degree Grantor / Ustanova koja je dodijelila akademski / stručni stupanj: **University of Zagreb, Faculty of Electrical Engineering and Computing / Sveučilište u Zagrebu, Fakultet elektrotehnike i računarstva**

Permanent link / Trajna poveznica: <https://urn.nsk.hr/urn:nbn:hr:168:385977>

Rights / Prava: [In copyright](#) / [Zaštićeno autorskim pravom.](#)

Download date / Datum preuzimanja: **2024-12-11**



Repository / Repozitorij:

[FER Repository - University of Zagreb Faculty of Electrical Engineering and Computing repository](#)





University of Zagreb
FACULTY OF ELECTRICAL ENGINEERING AND COMPUTING

Petar Bašić

**FIBER-OPTIC SENSOR CABLE FOR
SIMULTANEOUS DISTRIBUTED MEASUREMENT OF
MULTIPLE PHYSICAL QUANTITIES**

DOCTORAL THESIS

Zagreb, 2019



University of Zagreb

FACULTY OF ELECTRICAL ENGINEERING AND COMPUTING

Petar Bašić

**FIBER-OPTIC SENSOR CABLE FOR
SIMULTANEOUS DISTRIBUTED MEASUREMENT
OF MULTIPLE PHYSICAL QUANTITIES**

DOCTORAL THESIS

Supervisor:
Professor Zvonimir Šipuš, Ph.D.

Zagreb, 2019



Sveučilište u Zagrebu
FAKULTET ELEKTROTEHNIKE I RAČUNARSTVA

Petar Bašić

**SVJETLOVODNI SENZORSKI KABEL
ZA ISTODOBNO DISTRIBUIRANO MJERENJE
VIŠE FIZIKALNIH VELIČINA**

DOKTORSKI RAD

Mentor:
Prof. dr. sc. Zvonimir Šipuš

Zagreb, 2019.

This Doctoral thesis has been made at the University of Zagreb, Faculty of Electrical Engineering and Computing, Department of Wireless Communications and at STE d.o.o.

Supervisor: Professor Zvonimir Šipuš, Ph.D.

This doctoral thesis has: 117 pages

Doctoral Thesis No.: _____

ABOUT THE SUPERVISOR

Zvonimir Šipuš was born in Zagreb, Croatia, in 1964. He received both the B.Sc. and M.Sc. degrees in electrical engineering from the University of Zagreb, Croatia, in 1988 and 1991, respectively. He then gained his Ph.D. degree in electrical engineering from Chalmers University of Technology, Gothenburg, Sweden, in 1997. From 1988 to 1993, he worked at Ruđer Bošković Institute, Zagreb, Croatia, as a research assistant, involved in the development of detectors for explosive gases. In 1994, he joined the Antenna Group at Chalmers University of Technology, where he was involved in research projects concerning conformal antennas and soft and hard surfaces. In 1997, he joined the Faculty of Electrical Engineering and Computing at the University of Zagreb, where he is currently a professor. From 1999 to 2005, he was also an adjunct researcher in the Department of Electromagnetics, at Chalmers University of Technology. Since 2006, he has been engaged in teaching in the European Doctoral School of Antennas (ESoA). His current research interests include analysis and design of electromagnetic structures with application to antennas, microwaves, and optical communication and sensor systems. He is the author or coauthor of more than 60 papers published in scientific journals. Professor Šipuš received the annual national science award in 2006 for his research in conformal antennas and periodic structures.

O MENTORU

Zvonimir Šipuš rođen je 12. ožujka 1964. godine u Zagrebu. Diplomirao je i magistrirao na Elektrotehničkom fakultetu u Zagrebu 1988. godine, odnosno 1991. godine, a doktorirao je 1997. godine na Chalmers University of Technology u Göteborgu u Švedskoj. Od prosinca 1988. godine do srpnja 1993. godine radio je na Institutu Ruđer Bošković u Zagrebu u laboratoriju za poluvodiče. Sudjelovao je u razvoju uređaja za mjerenje koncentracije eksplozivnih plinova zasnovanih na poluvodičkim senzorima. Od kolovoza 1993. godine radi na Zavodu za radiokomunikacije na Fakultetu elektrotehnike i računarstva u Zagrebu, gdje je i danas prisutan u svojstvu redovitog profesora. Od rujna 1994. godine do listopada 1997. godine bio je na znanstvenom usavršavanju na Department of Microwave Technology, Chalmers University of Technology u Göteborgu u Švedskoj, gdje je bio doktorski student. Na istom je sveučilištu na jesen 1999. godine izabran u zvanje gostujući istraživač (Adjunct Researcher) i tu je aktivnost obavljao do 2005. godine. Od 2006. godine predaje i u Europskoj

doktorskoj školi antena (European School of Antennas). Znanstveno istraživačka djelatnost Zvonimira Šipuša vezana je uz analizu mikrovalnih antena i antenskih nizova, uz numeričke metode u elektromagnetizmu te uz svjetlovodne komunikacijske i senzorske sustave. Autor je ili koautor više od 60 znanstvenih radova objavljenih u znanstvenim časopisima. Zvonimir Šipuš dobitnik je državne godišnje nagrade za znanost za 2006. godinu, za istraživanja komformnih antenskih i periodičnih struktura.

ACKNOWLEDGEMENTS

I would like to express all my gratefulness to the following list of people that specially contributed to this work, support me in difficult times and helped me taking large steps in academic and professional life:

- To my mentor prof. dr. Zvonimir Šipus, and the colleagues at FER who contributed in different ways. Thank you Zvonimir for believing in me and bringing me gently back to the academic objectives when I was fully focused on my job. Thanks to doc. dr. Marko Bosiljevac for finding my mistakes and giving useful suggestions.
- To prof. Alan John Rogers with who my journey in optical fiber sensing started. Who would ever imagine that this professional and academic life will start with discovering the right book on a wrong shelf in an art shop? I am grateful for all our talks and walks and tennis games in the UK, Croatia and Austria.
- To Karl Bauer, the whole Bauer family, and the whole NBG Team. Thanks for the courage of listening and accepting my advices even for those I wasn't always sure of.

Special thanks to my family, without their contribution this work would not be possible:

- To my beloved wife Mirjana and our children; Marukina, Jeronim and Marčelina for their understanding, support and patience. Thank you, Mirjana, for all your strength that you are given and using for our family in spite of all difficulties and pain.
- To my mother Margareta and father Šime. Thank you for all what I am today.
- To my brother Ivan, my sister-in-law Ivana, my sister Katarina and brother-in-law Domagoj and all their families. There was always a warm bed and lunch for me during my studies and stay in Zagreb.
- To my father, mother and brother in law; Zvonimir, Vesna and Zoran. Thanks for all the support we received during master and doctoral study.

And finally, I am grateful to our Heavenly Father who cannot be detected and measured with the instrumentation we use but can be found deep in everyone's heart and who always finds the most astonishing ways to use us imperfect humans as a tool for the good. I am grateful for all I have and receive from you, and all your guidance so far. Please correct and route our ways in the future too. I am yours.

ABSTRACT

Fiber optic sensor cable technology is a relatively new research area that combines a set of scientific and technical disciplines in order to meet distributed sensor systems needs and quality standards. This thesis discusses a particular fiber optic cable design with three tightly encapsulated fibers for multipurpose and multivalent sensing, presently commercialized for temperature, strain and acoustic measurements. Furthermore, it introduces a mechanism for birefringence change as a function of outer perturbations, such as pressure and cable bending, as a new capability and potential feature for future optical sensor products. The concept is based on using cable raw materials (optical fiber, stainless steel strips, matured manufacturing procedures) with standard geometries produced and commercialized in high volumes nowadays. It uses symmetrical elements only and it exploits the geometrical configuration of equilateral triangle with optical fibers in each vertex that are tight buffered within the stainless-steel tube. This results with unsymmetrical loading of the optical fibers when exposed to external hydrostatic pressure thus giving rise to the birefringence change in the optical fibers. In this way the hydrostatic pressure as external mechanical measurand is coupled with optical parameters inside the interior optical fibers hermetically closed inside the stainless-steel tube. The concept was first evaluated with the Finite Element Analysis (FEA) commercial software tool resulted in proving the concept and giving the insight into the magnitude of tube compression.

The prototype of the cable 1.24mm in diameter was manufactured and tested up to 1200bar in a 24m long high-pressure chamber, especially designed for such purposes, enabling both mechanical and optical characterization of the sensor cable. The polarimetric method was chosen to prove the concept of changing birefringence properties of optical fiber. Although non-linear and irreversible, it demonstrated a strong change in Stokes parameters during both, pressure increase as well as pressure decrease cycles. Furthermore, the high-pressure facility is further used for evaluation of tube compression without optical fibers. The compression of the tube 2.1mm in diameter and steel wall thickness of 0.4mm, steel grade 316L was measured and thus exhibited linear characteristics for the pressure range from 0 to 1200bar. Due to off-the-center positions of optical fibers, the construction has the intrinsic capability to measure cable bending. The information on bending is always available since there is always at least one fiber in the compression zone and one in the extension zone. The sensor fibers were interrogated with

the Brillouin Optical Time Domain Analysis (BOTDA) interrogation method. For testing purpose, a 20m long sample was produced and arranged in a coil of different diameters, and BOTDA measurements demonstrated shift in Brillouin peak frequency for all three observed fibers. In this way it was confirmed that optical fibers 0.455mm in diameter, placed off-the-center inside the stainless-steel tube of 1.25mm in diameter, can be used for fiber optic distributed pressure and/or cable bending evaluation using stimulated Brillouin scattering technique.

Keywords: *optical fiber, fiber optic measurements, monitoring systems, fully distributed optical fiber sensor, fiber in metal tube (FIMT), pressure sensors, acoustic sensors, strain sensors, temperature sensors, distributed optical fiber sensors, Brillouin effect, Brillouin Optical Time Domain Analysis (BOTDA)*

Svjetlovodni senzorski kabel za istodobno distribuirano mjerenje više fizikalnih veličina

U svijetu koji se digitalizira i u kojem količina podataka eksponencijalno raste i u kojem svi i sve dobivaju ulogu izvora ili korisnika podataka mjerna osjetila i mjerne metode nalaze se na samom početku tog lanca. Jedan od glavne ciljeva digitalizacije su dovoljna količina podataka korištenjem cjenovno i ekološko prihvatljivih tehnologija. Uz tradicionalne senzorske tehnologije koje se koriste u praćenju fizikalnih veličina koje se temelje na mehaničkim, električnim, magnetskim, kemijskim i biokemijskim i ostalim metodama i koji su uglavnom diskretnog tipa tj. ostvaruju mjerenje na jednom mjestu, pojavom svjetlovoda uvele su se nove mogućnosti u industriji. Niskih gubici, golemi mjerni doseg kao i neosjetljivost na elektromagnetsko okruženja, galvanske uvjete, postojanost na povišenim temperaturama i mogućnost ostvarivanja osjetilnih mikrostrukture u velikim nizovima u jezgru i omotač svjetlovoda ponudili su novi pristup i tip mjerenja – kvazi i potpuno distribuirano mjerenje. Ostvarene prednosti ovakvog pristupa koja su prepoznata u industriji su:

- upotreba cjenovno jeftinih standardnih telekomunikacijskih vlakana u velikom broju primjena drastično pojeftinjuje mjerenja
- gdje god se polaže svjetlovodna telekomunikacijska mreža moguće je iskoristiti vlakna i za razna mjerenja za vrijeme rada telekomunikacijskog sustava koristeći se neosvijetljenim vlaknima ili nekorištenim valnim duljinama u osvjetljenim vlaknima
- senzorski svjetlo vodi mogu se zajedno sa ostalim standardnim vlaknima i metalnim vodičima integrirati u kabele koji se polažu i ugrađuju na poznate i rutinirane načine u zemlju, objekte, infrastrukturu itd.
- broj mjernih točaka uzduž istog mjernog svjetlovodnog kabela može biti i do nekoliko stotina tisuća što donosi posebno povoljan odnos cijene po 1km instaliranog sustava

Tehnologije koje se koriste za distribuirana mjerenja temelje se na nekoliko fizikalnih principa svjetlosnog raspršenja u svjetlovodnom vlaknu; Ramanovo, Rayleighovo i Brillouinovo raspršenje te na uvođenju mikrostrukture u staklenu strukturu svjetlovoda. Ova doktorska disertacija obrađuje posebnu konstrukciju svjetlovodnog kabela sitnih dimenzija i trima stiješnjeh svjetlovoda, izrađenog tehnologijom laserskog varenja čelične cjevčice i koji u sebe može integrirati sva tri mjerna postupka i time ponuditi ne samo jedno nego minimalno 3 mjerna postupka.

Ova teza organizirana je u 5 glavnih poglavlja. Budući da je temeljna ideja bila fizički razviti kablanski senzor, ispitivanja i predložiti tehnike ispitivanja, organizacija poglavlja odraziti će tipičan razvoj proizvoda.

Teza započinje uvodnim poglavljem koje daje detaljan opis učinaka dvolomnosti u jednomodnim optičkim vlaknima te mehaničkih i toplinskih poremećaja koji ga dovode do toga. Također je prikazan opis vlakana u tehnologiji proizvodnje metalnih cjevčica.

U drugom poglavlju detaljnije je prikazana teorijska pozadina stimuliranog Brillouinovog raspršenja u svjetlovodu. Ono potom pregled neelastičnog optičkog raspršenja i uvodi relevantne zakone fizike koji opisuju ove učinke. Teorijska analiza započinje mikroskopskim opisom dielektričnog medija, električnom polarizacijom, protupropagirajućim elektromagnetskim valovima i efektom elektrostrikcije koja uzrokuje promjenu gustoće mase i pojavu akustičnog vala, zatim opisom Brillouinovog međudjelovanja i parametara bitnih za njegovu karakterizaciju i mjerenja koja su također data u poglavlju.

Koncept kabela predložen je i detaljno obrazložen u Poglavlju 3. mehanizam utjecaja vanjskog hidrostatskog tlaka na svojstva dvolomnosti svjetloveda predstavljen principima Newtonove mehanike. Koncept se zatim kvantitativno ispituje metodama analize konačnih elemenata koji pokazuju asimetrično opterećenje svjetloveda i time dokazuje koncept. Proizvodnost konstrukcije prvo se ispituje i objašnjava mjerenjima slabljenja optičkog vala. Ispitivanja se nastavljaju uvođenjem Stokesovih polarimetrijskih parametara te polarimetrijskim mjerenjima koja se provode u komori visokog tlaka (posebno razvijena za visokotlačno i visokotemperaturno ispitivanje i ukratko predstavljena u poglavlju). Polarimetrijska mjerenja pokazuju snažnu ovisnost o promjenama tlaka. Poglavlje se završava testom kompresije cijevi koji pokazuje linearnu promjenu promjera metalne cijevi kao funkciju hidrostatskog tlaka.

Poglavlje 4 predlaže, analizira i raspravlja o novoj metodi ispitivanja raspodijeljenog tlaka zasnovanoj na tzv. polarizacijskoj učinkovitosti polarizacije kod Brillouin-Lorentzianove dobitka i njezinoj ovisnosti o konstanti širenja i poziciji na ispitivanom vlaknu. Poglavlje objašnjava slabu ovisnost konstante širenja za slučaj uskog raspona valnih duljina kod interakcije protupropagirajućih valova stimuliranog Brillouinovog raspršenja te objašnjava snažnu ovisnost o vrijednosti vanjskog tlaka. Metoda ekstrakcije parametara dvolomnosti razvijena je u spektralno-prostornom domeni pomoću tehnike pretraživanja ekstrema. Poglavlje 5 govori o prednostima predložene konstrukcije kabela koja sadrži tri optička vlakna

koja su u ovom slučaju koristi za procjenu promjera savijanja svjetlovodnog kabela. Poglavlje daje opis koncepta ispitivanja primjenom tehnike stimulirane Brillouinovog raspršenja te razvijenog uzorka kao i dobivenih podataka mjerenja.

Konstrukcija i mjerne metode obrađene u ovoj disertaciji predstavljaju osnovu za nove srodne konstrukcije i mjerne metode koje će biti predmet industrijskog razvoja u skorijoj budućnosti. Budući se radi vjerojatno o najučinkovitijoj i cjenovno najprihvatljivijoj tehnologiji i načinu za digitalizaciju velikih i dugih infrastrukturnih objekata, većih i manjih geografskih površina i geofizičkih polja očekuje se da će distribuirane senzorske svjetlovodne kabela konstrukcije i nadalje biti predmet investicija i razvoja industrije svjetlovodnih kabela, specijalnih optičkih vlakana i svjetlovodnih mjernih metoda.

CONTENTS

1. INTRODUCTION	2
1.1. Step-index optical fibers.....	4
1.2. Introduction to birefringence in optical fibers.....	8
1.3. Fiber in Metal Tubes (FIMT)	12
1.4. Structure of the thesis	15
2. STIMULATED BRILLOUIN SCATTERING	17
2.1. Light in dielectric medium	19
2.2. Case study: two counterpropagating lightwaves	23
2.2. Polarization nonlinearity of 2nd order.....	26
2.3. Evolution of acoustic wave	27
3. FIBER OPTIC PRESSURE SENSING CABLE	37
3.1. Sensing cable construction and verification methods.....	37
3.2. Three optical fibers working together	38
3.3. Optical loss consideration for the cable design	41
3.4. Validation of impact on birefringence and pressure sensitivity using FEM	42
3.5. Validation using polarization measurements and Stokes parameters.....	44
3.6. Compression of the stainless-steel tube in the high-pressure condition.....	50
4. FULLY DISTRIBUTED PRESSURE INTERROGATION METHODS USING STIMULATED BRILLOUIN SCATTERING	55
4.1. Brillouin-Lorentzian profile and the investigation of polarization efficiency ξ application in distributed pressure measurements.....	65
4.2. Extraction method 1: finding extremes of ξ in spectral domain.....	70
4.3. Extraction method 2: finding extremes of ξ in spatial domain	75
4.4. The measurement set-up and results.....	82
5. BENDING OF THE CABLE.....	90
CONCLUSIONS.....	108
REFERENCES	110
BIOGRAPHY	115
ŽIVOTOPIS.....	117

1. INTRODUCTION

In Internet of Things (IoT) systems and massive digitalization of physical objects and infrastructure are the industry of the 21st century. There are different approaches to this call. All systems and solutions are based on either wireline, or wireless systems or a combination of the two. Among these two approaches, there are a few different technologies using photonic phenomena and employing optical fibers and cables of different types and sizes - such as measurement probes and sensors providing detection and measurement data at each segment in the length. They are referred to as distributed fiber optic sensors [1]-[3]. As such they add contribution to the digitalization efforts, especially in cases when measurement can be conducted only from one end of the long linear asset, i.e. long infrastructural object. Since detection and measurement regime is distributed by vocation, their costs are considered per-meter or per-kilometer. This is where optical fiber sensing systems offer unmatched price-performance ratio. It is also the reason for their growing success in the industry in the last decades. They have become the essential digitalization tools in energy discovery, production and transportation. Examples of this are: distributed temperature sensor (DTS) [4], [5] distributed temperature and strain sensor (DTSS) [6]-[10] and distributed acoustic sensor (DAS) systems [11]-[14]. Their further advantages are related to high sensitivity, electromagnetic and galvanic transparency, small size and weight etc.

Meeting strict industrial and environmental standards represent engineering challenges on both - system and sensor design. It starts with material composition and selection, sensor construction, manufacturing processes and testing methods and procedures. These results are in need of constant improvements and specialization in all: sensing optical fiber, sensor cable design, interrogation hardware, as well as in signal processing, interpretation and visualization techniques. The smart design of optical fiber and cable constructions can dramatically impact and reduce the degree of complexity in upper layers of the measurement system, such as the one in the optical and signal processing layer. On the other hand, system designers must be aware of the system applicability on sites, too. This is especially true for sensing cables as they are set in contact with the physical environment and quantities that are referred to as measurands. Working on deployment sites in many cases involves harsh and extreme conditions. The best examples are geophysical and civil construction sites in which open optical fibers are exposed to water, hydrogen rich chemicals and mechanical stress. Therefore, they differ largely from laboratory conditions in which the systems are conceptualized and

constructed. The manipulation of fiber optic sensing cables that include working with sensitive optical fibers under such circumstances represents a constant challenge, and it very often requires special skills and experience from the technicians. On the other hand, the designers of sensor interrogation equipment, cables and application solutions must be aware of their applicability on sites.

Fully distributed fiber optic detection and measurement systems are relatively new to the industry, yet they always play increasing roles in it. The reason for this is unique properties of optical fibers against other available technologies when it comes to long-range detection and measurements. There are more advantages but the most important are low loss and independence from environmental galvanic and electromagnetic circumstances. This is especially true for linear structures such as overhead lines, roads, pipelines and geophysical structures. There are also other non-fully distributed sensing and measurement techniques available in the industry today using 1D microstructures such as Fiber Bragg Grating (FBG) and punctual or quasi distributed systems. Nevertheless, industry recognized distinctive qualities of distributed measurements using optical fibers. From the technical point of view, this is long distance spatial profiling of physical quantities, from the interrogator set at one end of fiber optic sensing cable. From the economical point of view, it is its unique price per kilometer parameter making it very interesting for commercial deployment. Perhaps the best example of this is the industrial success of Raman based distributed temperature sensors [15]-[17] which nowadays is standard equipment in many applications. Distributed strain and temperature sensors based on Brillouin scattering [18]-[21], [51], [52] and distributed acoustic sensors (DAS) [12]-[14], [21]-[24] are installed in monitoring systems of various long infrastructures, such as subsea and land pipelines, dams, dikes etc. The deployment site in many cases involves harsh and extreme conditions such as in geophysical and civil construction sites. They therefore differ largely from laboratory conditions where the systems are conceptualized from scratch. The manipulation of fiber optic sensing cables that include sensitive optical fibers in such circumstances represents a constant challenge, and it very often requires special skills and experience from technicians.

This thesis presents and discusses a unique sensor cable design [29] presently used in industry in distributed strain and acoustic measurements. The thesis will show that this concept has the potential to be deployed in distributed pressure measurements as well, for example, by means of birefringence change techniques [30]-[32]. The cable sensor hereby proposed is based on

common industrial elements and raw materials with manufacturing conform geometries and is aimed for multipurpose and configuration multivalent distributed optical fiber sensing techniques, and among them, distributed pressure sensing which is considered as the largest technical challenge. Although various activities on distributed pressure sensing have been reported from all around the world, many of them refer to optical fiber only [25]-[28], [30]-[32] the fully & truly distributed pressure cable sensor and interrogation systems, in their industrial acceptable versions, which is still not commercially available to our knowledge, and it remains a challenge. In this thesis, it will be approached by means of the so-called Stimulated Brillouin Scattering Technique.

Step-index optical fibers

Optical fiber is a light guiding structure made of three or more layers; a waveguiding glass structure, protective coating made of a soft primary coat and a hard secondary coat on top of which there are one or more harder outer polymer jackets added as an option for more mechanical protection and robustness. Fig.-1.1 shows the typical geometry of optical fiber.

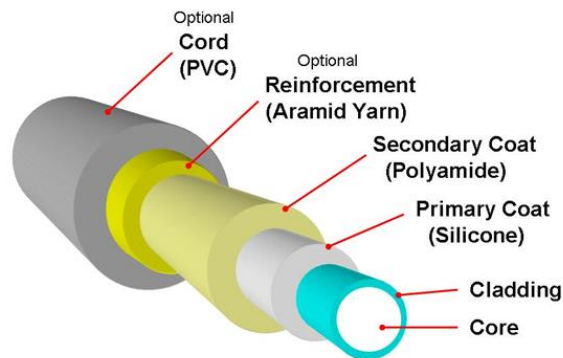


Figure-1.1: Construction of optical fiber must meet mechanical and optical requirements. The coatings bring mechanical stability to the glass without compromising optical performance while buffering brings strength

Inside the optical fiber the wave can propagate in more modes or in just one mode. In that respect, we distinguish multimode and single-mode propagation regime. Although both multimode and single-mode fibers are used in distributed sensing industry, we will focus on

single-mode optical fibers and propagation regime necessary for sensing techniques addressed in this thesis.

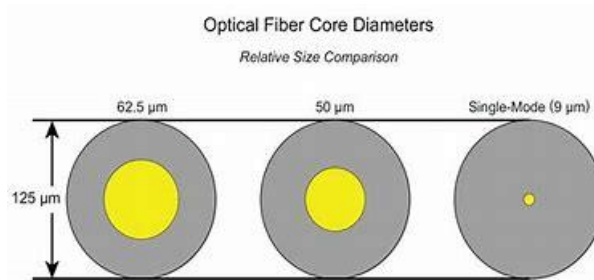


Figure-1.2: Multimode and single-mode fibers

All the standard optical fibers in their single-mode propagation regime are designed for the so called weakly-guiding condition, in which light is confined and therefore guided in two geometrically orthogonal propagation modes with an almost linearly polarized EM field, both of which comprise the single guiding mode designated as HE_{11} . The component in which the magnetic field is a dominant field, and aligned with x-axis and y-axis, is called HE_{11}^x and HE_{11}^y respectively. In dielectric waveguides not all power is confined within the core - some of it exists in the cladding too, although rapidly decaying with the radius, so-called evanescent field. Bringing more light power in the cladding can be done by choosing a relatively small numerical aperture NA that reflects a small difference in refractive indexes between the core and the cladding. Figure-1 shows propagation modes in weakly guiding regime in optical fiber with $NA=0.11$.

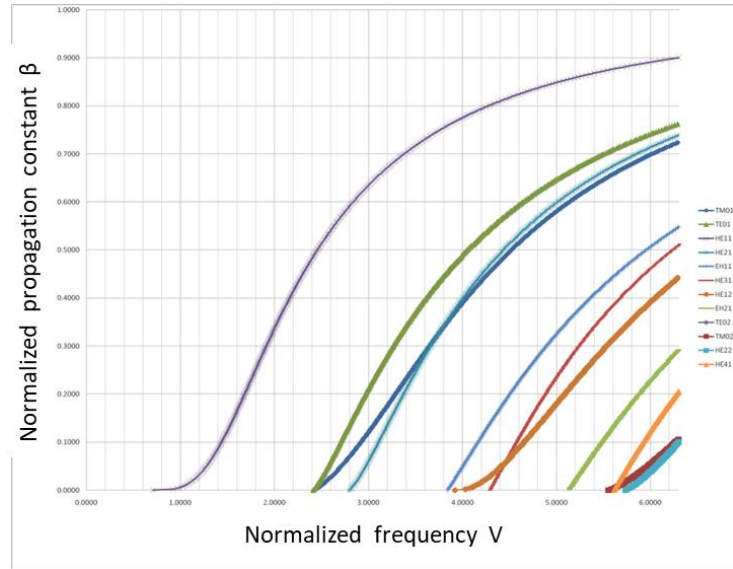


Figure-1.3: Propagation modes in non-weakly guiding fibers, in this case $n_1=1.45$, $n_2=1.00$

In the analysis of propagating modes in cylindrical structures, frequency appears as the most important parameter. In optical fiber, this role has taken the parameter called normalized frequency, or V-number. It contains all important parameters of a step-index construction and it defines the propagating modes. In other words, only one parameter is needed to characterize the fiber properties. It is proportional to the frequency, thus the name normalized frequency. It reveals cut-off frequency/wavelength – that separates the multimodal regime from the single-modal propagation regime for the step index design. Normalized frequency is defined with:

$$V = \frac{\omega a}{c} \sqrt{n_c^2 - n_{cl}^2} = \frac{2\pi a}{\lambda} \sqrt{n_c^2 - n_{cl}^2} = \frac{2\pi a}{\lambda} NA \quad (1.1)$$

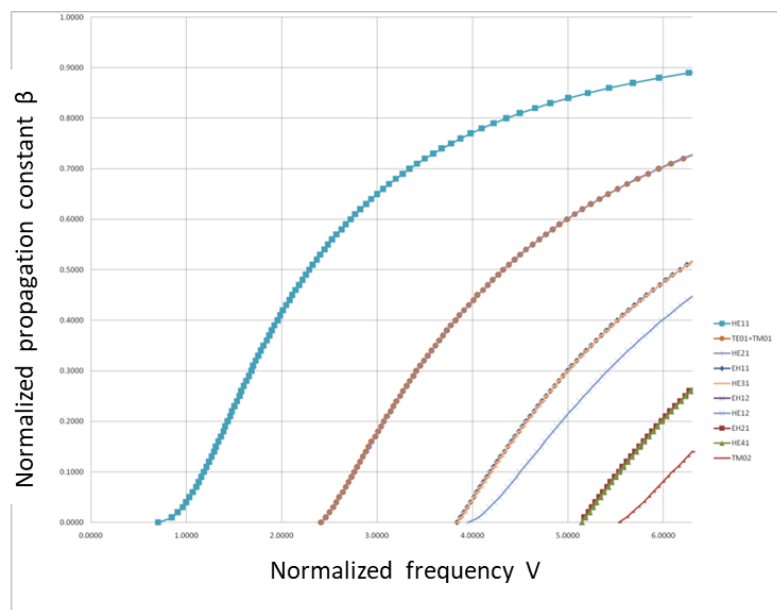
where:

- a – radius of optical fiber
- ω – angular frequency of mode
- n_c - refractive index of core
- n_{cl} - refractive index of cladding
- λ – wavelength of light in vacuum
- $NA = \sqrt{n_c^2 - n_{cl}^2}$ - numerical aperture of fiber.

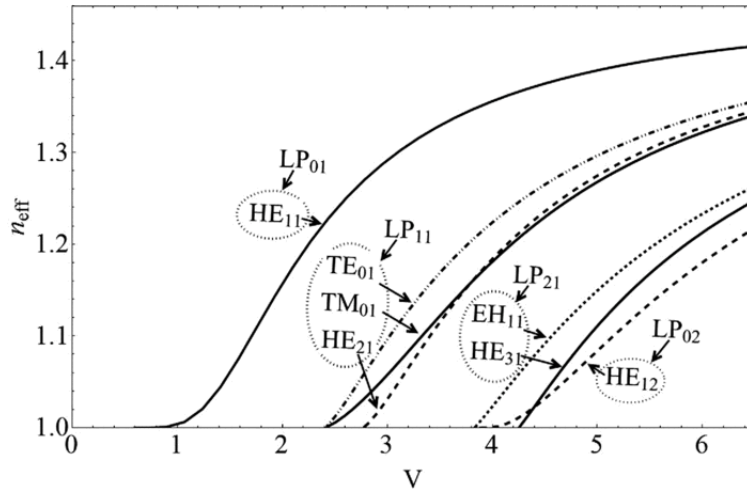
One another parameter important in analysis and design of single-mode optical fibers is Δ and is defined as:

$$\Delta = \frac{n_1 - n_2}{n_1} \ll 1 \quad (1.2)$$

In practice, the difference $n_1 - n_2$ is very small, typically of the order of 10^{-3} and 10^{-4} . The lower Δ means that light approaches transverse electromagnetic waves and in this case electric and magnetic components in the direction of propagation, E_z and H_z , get very small compared to transverse components - but still non-zero. In this weakly propagating regime with lower Δ the modes form clusters of linear polarization modes or LP_{lp} (Figure). l represents the number of zero crossings in the whole azimuthal range divided by two, and p represents the number of intensities in radial direction. LP_{lp} modes exhibit an amplitude of an exceptional symmetry and may be linearly polarized either along the x or the y axis. LP_{01} mode is solely made of HE_{11} mode. For example, for the LP_{01} mode: its two degenerated polarization modes LP_{01}^x and LP_{01}^y exhibit the same propagation constant in a perfect cylindrically symmetric fiber.



(a)



	HE11	TE01	HE21	TM01	HE31	EH11	HE12
Exact modes							
LP modes	LP01	LP11		LP21		LP02	

(b)

Figure-1.4: Weakly guiding propagation regime - modes forms clusters of linear polarized modes; modes merging depicted in $\beta - V$ graph (a), and evolution of linear polarization in the modes (b). Among all the modes, LP_{01} is the most important in the applications

Liner polarization and symmetrical propagation constant in both axes open a new range of application possibilities. Nowadays, all existing interferometric and polarimetric high speed telecommunication and sensing systems exploit these features.

1.2 Introduction to birefringence in optical fibers

In the ideal case, in which the fiber cross-section is perfectly circularly symmetric and optical properties in both axes are equal, light propagates with the same conditions in both axes, and therefore at the same velocity. Any perturbation that gives rise to asymmetry in optical or geometrical properties shall cause birefringence in the fiber. In such case, both characteristic components of lightwave that are launched at the same time through the fiber shall arrive at different times to the other end. This is called modal dispersion due to birefringence. Birefringence can therefore arise from the difference in refractive indices, or non-concentricity

and elliptical deformation of the fiber cores. In general, the stress-induced birefringence dominates the geometry-induced one. In real practical fibers, birefringence is always present to some extent, and it impacts polarization states in optical fibers. Figure 2 depicts general spatial polarization evolution in the optical fiber core.

There are two kinds of optical birefringence in optical fiber; linear and circular birefringence. Linear birefringence is defined as:

$$\Delta n = n_e - n_o \quad (1.3)$$

where n_e and n_o are two effective refractive indices in two orthogonal directions in the cross-section of optical fiber. Because of the difference in refractive indices, light shall travel with different propagation constants in two axes. Linear birefringence is therefore highly susceptible to mechanical stresses, such as bending and asymmetric pressure. To some extent, there is also circular birefringence always present in propagation of the lightwave. This physical background lies in the structure of fiber material, i.e. helix in molecular structure, and this phenomenon is referred to as optical activity, in which molecular electrons are subjected to different properties in rotational motions along the longitudinal propagation axis. Another cause of difference in rotational properties with the same repercussions can be due to an external longitudinal magnetic field. This all results in an effect in which the rotation of an electron is easier in one direction than in the other. It shall therefore introduce phase difference between orthogonal polarization states giving rise to a spiral rotation resulting in a transverse electric field either clockwise or counterclockwise. Because linear birefringence and circular birefringence are superimposed in optical fiber, the general polarization state shall be elliptical, changing its properties and shape along the length, being highly susceptible to mechanical stresses and magnetic fields.

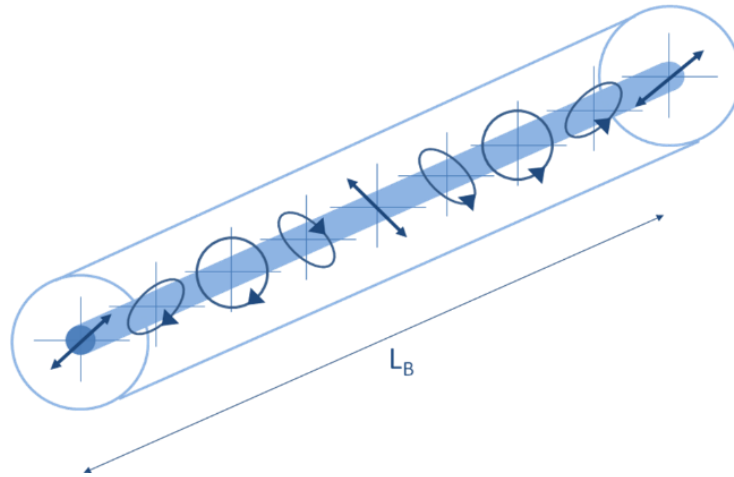


Figure-1.5: Polarization evolution in single-mode optical fiber. Beat Length L_B represents one cycle in which the polarization state makes one full circle across the fiber length

Birefringence; linear, circular or elliptical $\Delta n = n_e - n_o$ introduces phase change between two principal axes – the fast and the slow axis. This phase change is:

$$\theta = \frac{2\pi l}{\lambda} \Delta n \quad (1.4)$$

where λ is the signal wavelength in free space and l is the fiber length. Longer optical fiber and/or larger refractive index differences cause larger phase shifts. This needs to be considered during fiber design. The length that represents the phase change of $\theta = 2\pi$ is called polarization beat length L_B , and it can vary in an optical fiber.

$$L_B = \frac{\lambda}{\Delta n} \quad (1.5)$$

From (1.5) we see that the smaller the refractive index difference increases polarization beat length. Several methods are typically used in the measurement of L_B . Taking the beat length from the measurements and knowing the wavelength used, we can calculate Δn .

Birefringence itself is sensitive to many physical quantities [37]-[42]. We will here name a few of them, and they are:

1. Noncircular core – if fiber is elliptical, the lightwave propagates in one principal axis for a longer time and in the other for a shorter time. This causes phase spatial mismatch and therefore this birefringence is referred to as geometrical birefringence

2. Presence of stresses

- a. Internal stress – stress introduces variations in the refractive index in silica over due to the elasto-optic effect. By means of specialty designs, such as the panda and bow-tie designs, internal stress is the method used to build highly birefringent fibers.
- b. External stresses - bending introduces stress birefringence due to introduction of asymmetry in the refractive index in sections with bending radii smaller or larger than the one of the neutral axes. This effect can be used for the evaluation of the cable bending radius using the cable design proposed in this thesis which is discussed in Chapter-5
- c. Twisting - introduces circular birefringence as it changes phase retardance between the fast and slow axis. Generally taken, the State-Of-Polarization (SOP) in the fiber is elliptical. In an ideal optical fiber, left-handed and right-handed eigenmodes are balanced. The twisting makes one eigenmode propagate at a different speed compared to the other introducing retardance. Thus, the polarization ellipse changes its form at the position of the twist.

3. Presence of electromagnetic fields

- a. transversal electric fields – a very strong electric field perpendicular to the fiber axis (by means of the electro-optic Kerr effect) can introduce birefringence in optical fiber. Phase delay between the eigenmodes is proportional to the square of the electric field amplitude.
- b. longitudinal magnetic field – additional retardance in circular polarization is introduced in the optical fiber if a longitudinal magnetic field is present via Faraday magneto optic effect.

This thesis will discuss how stress induces birefringence changes in linear polarization of a propagating lightwave by means of cable design that is explained in detail in the following chapters.

1.3 Fiber in Metal Tubes (FIMT)

Measurement of physical quantities (so-called ‘the measurands’) such as temperature, strain and pressure set special requirements on sensing optical cables. On one hand, the cable must be designed to protect optical fibers against the environment and measurands, and on the other hand, it must expose the fibers to the environment and the measurands, but within acceptable limits. Optical fiber alone is too fragile and too sensitive for these requirements and it needs mechanical and chemical protection. For example, the lifetime of an optical fiber exerted to few percent of strain can be in the range of days or weeks. The standard optical fibers installed in a borehole conditions and operation will have an increase in attenuation, and finally, it will ‘get dark’ in hours or days due to hydrogen ingress. In ~~the~~ temperature measurements it is sufficient to encapsulate optical fibers inside robust metallic constructions in a loose way, as metallic encapsulations bring good mechanical and chemical protection and rapid transfer of thermal energy. Nevertheless, unlike temperature measurement in which optical fibers must reside loosely within the cable, in strain and pressure measurements it is necessary to bring optical fibers in physical contact with protective layers on top of them in order to ensure the transfer of mechanical quantities to the optical fiber. Fig-1.6 shows a few versions made for different kinds of optical fibers and tubes.

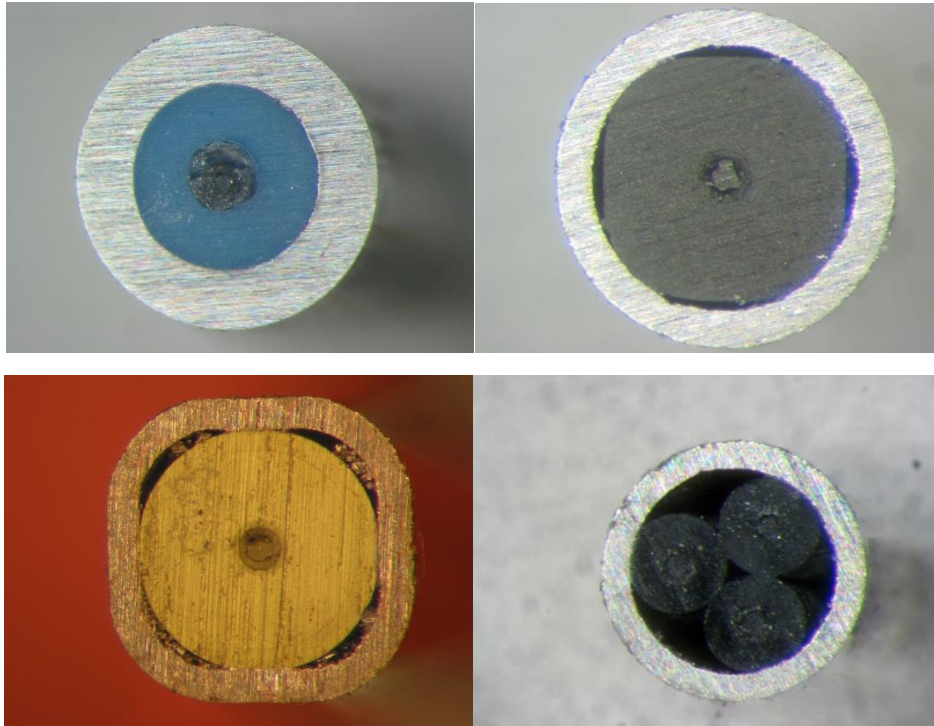


Figure-1.6: Various tight buffer constructions; top-left: all round watertight construction, top-right: rectangular fiber with round encapsulation tube with voids included, bottom-left: round fiber in rectangular tube, and bottom left: multifiber construction (three round fibers) within round tube

These protective layers now have an additional task – they need to scale the magnitudes of the measurands to ranges acceptable for the normal operation of optical fibers. The way these requirements are realized determines the crucial sensing cable parameters and its success in the deployment. Conceptually it can be realized in different ways with a variety of materials and construction purposes. Since optical fiber is now tightly encapsulated in a more robust cable construction, it is not only mechanical properties of optical fibers that matters - now the whole construction is responsible for the performance. This represents a challenge, as the material properties are never ideal, and have hence become the source of ambiguities and inaccuracies in the measurements. This is the reason why sensing cables that are aimed for distributed strain and pressure measurements are far more difficult to design and manufacture than all loose tube designs constructed for telecom and temperature measurement applications. Since optical fibers are mechanically and chemically fragile in respect to the fields in which they must be deployed, the fiber in metal tubes (FIMTs), and especially their more specialized versions, are considered as the main and fundamental encapsulation techniques, the quality of which impacts all other cable making proceeding procedures. On the other hand, if these challenges in all strategic fields; specialty optical fiber, FIMT, sensing cable designs and manufacturing processes are

addressed with provable innovative approaches leading to solutions, then the industrial fruits of it can be numerous. The objective of this thesis goes in such direction – it shall suggest a new way toward distributed pressure measurements (DPS) techniques by means of combination of both; special cable design and the methods to interrogate them. It shall prove once again that the real solution with acceptable time-to-market approach is a multidisciplinary field requiring strong collaboration.

FIMT production line [Fig.-1.7] comprises of several modules set inline along the production line. All the details of the production are out of scope of this thesis and hence will only be briefly explained. The line is basically segmented into 3 parts:

- feed-in modules for the metal strip and optical fiber
- main module with a jelly filling device, laser welding station, tube forming station, and tube reduction station
- lead out modules with disk capstan, a seam testing unit and FIMT take up

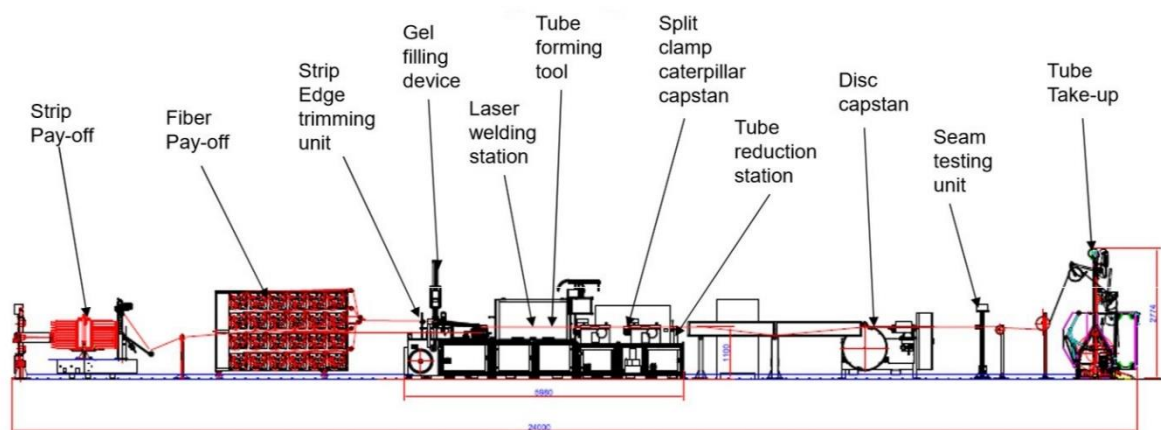


Figure-1.7: Fiber in Steel Tube production line [manufacturer Nexans - www.nexans.de]

The production starts with purchasing the steel strips and mounting them on the payoff module – a vertically or horizontally module with a rotatable wheel that in a controllable way releases the strip into the line. Between the strip payoff module and strip edge trimming unit there is a fiber payoff module – a rack built for hosting the matrix of fibers spools. It unwinds optical fibers and can arrange them in bunches and lead them into the main station. Once the strip and optical fibers bunches reach the main module, the strip will be processed and final encapsulation of optical fibers with target diameter can take place. The strip edges are trimmed at the

beginning of the module, hence prepared for the welding process that must run smoothly and uneventfully for many kilometers. Within the tube forming tools the strip is (in more stages) formed into a closed pear-like form, now with optical fibers encapsulated within. The tube is then laser welded. The welding process is done using inert gasses (Helium, Argon) assuring quality welding and it is always monitored and welding parameters are documented. The split-clamp capstan helps driving the process and mechanically stabilizes it. The ‘early FIMT’, now welded, is brought through a series of dyes in a tube reduction station to reach the target outer diameter (OD). After OD reduction the tube is eventually cleansed in a washing bath from all the residues of industrial lubricants and then dried. At this stage the tube leaves the main module and is forwarded to the disc capstan – the main pulling/driving module. The disc of the capstan hosts few windings on its circumference assuring enough friction required to transfer the rotational momentum into pulling force with good stability. After leaving the capstan the tube is checked at the seam testing unit performing the Eddy current check procedure and seeking in-homogeneities in the outer surface of the tube. After the test, the FIMT is wound onto a production reel at tube take-up system. This has been a description of the production line in general and specific production processes in production facilities around the world can be different, and additional modules can be seen in the premises, all according to industrial specialization of the actual production line and the needs in the market.

1.4 Structure of the thesis

This thesis is organized in the 5 main chapters. Since the essential idea was to physically develop a cable sensor, the tests and to propose novel interrogation techniques, the organization of chapters shall reflect typical product development.

The thesis starts with the introductory chapter which provides a detailed description of birefringence effects in single-mode optical fibers, and of mechanical and thermal perturbations giving rise to it. The description of fiber in metal tube production technology is also presented.

Chapter 2 presents the theoretical background of stimulated Brillouin scattering effects in more details. It gives an overview of inelastic optical scattering and introduces relevant laws of physics describing these effects. Theoretical analysis starts with a microscopic scale description of dielectric medium, electric polarization, counter-propagating electromagnetic waves and

electrostriction effect giving rise to the change in mass density and acoustic wave, the description of Brillouin interaction and of parameters relevant for its characterization and for the measurements are also given in the chapter.

The cable concept is proposed and explained in detail in Chapter 3. The mechanism of the impact of external hydrostatic pressure on the birefringence properties of optical fibers is presented using Newtonian mechanics. The concept is then quantitatively tested using Finite Element Analysis methods exhibiting asymmetrical loading extorted to the optical fibers and proving the concept. The producibility of the construction is first tested and explained with optical loss measurements. The tests are proceeded with the introduction of Stokes polarimetric parameters and with polarimetric measurements conducted in the high-pressure chamber (specially developed for high-pressure and high-temperature testing and briefly presented in the chapter). The polarimetric measurements show strong dependence on pressure variation. The chapter concludes with the tube compression test showing linear change in metal tube diameter as a function of hydrostatic pressure.

Chapter 4 proposes, analyzes and discusses a novel distributed pressure interrogation method based on polarization efficiency of the Brillouin-Lorentzian gain and its dependence on the propagation constant and position along the tested fiber. The chapter explains weak dependency of the propagation constant for a case of narrow wavelength range, such as one in the Brillouin interaction process, and explains strong dependency on external pressure value. The method of extraction of birefringence parameters is developed in the spectral-spatial domain using extremes searching technique.

Chapter 5 discusses the benefits of the proposed cable construction containing three optical fibers set for evaluation of cable bending. The chapter gives a description of the interrogation concept using the stimulated Brillouin technique, and of the developed sample as well as the obtained measurement data.

2. STIMULATED BRILLOUIN SCATTERING

The scattering in optical fibers can be elastic and inelastic. Elastic scattering is such a kind of scattering in which the scattered wave has the same wavelength and frequency as the incident wave. An example of elastic scattering is Rayleigh scattering. An inelastic scattering is a kind of scattering where the wavelength or frequency of the scattered wave is different for the incident wave. An example of inelastic scattering is Raman and Brillouin scattering; the latter being the subject of this chapter. Scattered light is frequency shifted and these frequencies can be downshifted and upshifted, all in accordance with energy transition relative to ground states. In quantum physics such scattering processes are depicted in Fig.-2.1. Incident pumping photons are absorbed by molecules in an optical medium populating (a) few ground energy states. These molecules making upward transition to the higher quasi-stable virtual states can reside only shortly there and they transit back to ground energy states. In the downshifting process, a photon in elastic transition is emitted at the same wavelength as an incident photon, whereas in inelastic transitions, such as Brillouin, the photon is emitted at a different wavelength. In an inelastic Brillouin transition, two photons can be emitted; the Stokes and anti-Stokes photons.

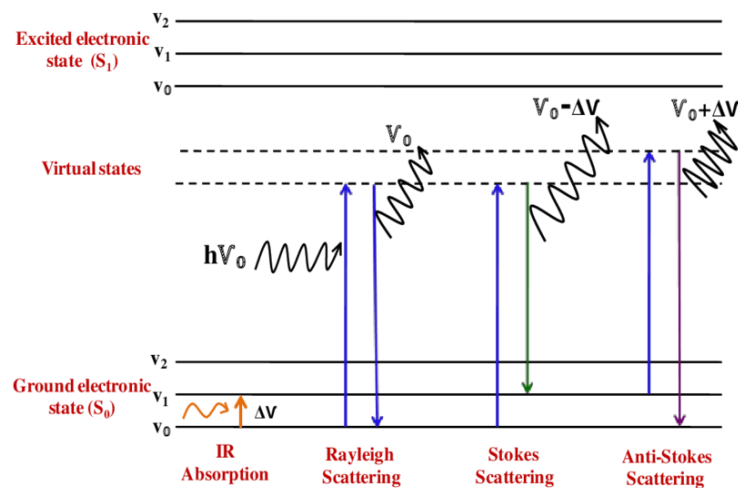


Figure-2.1: Photon absorption and emission processes in optical medium

Photon emission, having lower frequency and therefore energy than pumping light, is referred to as Stokes emission, whereas emitted light with larger energy than the pumping energy is referred to as anti-Stokes emission. There is a fundamental difference between Raman and Brillouin scattering and it reflects the nature of these two physical effects; Raman scattering

reflects thermomechanical vibration and rotation perturbations in the atom bonds of an optical medium interacting with photons, thus causing frequency shifts. The source of frequency shifts in Brillouin effects are electric fields and the changes of density of the optical medium by means of electrostriction effect giving rise to an acoustical wave. Because of its nature, the frequency and wavelength shift in the Raman effect are much larger than shifts in Brillouin effects. The Raman wavelength shifts amount to several tenths of nanometers, while wavelength shifts in Brillouin amount to a few picometers. The wavelength measurements of the emitted lightwave reveals the thermal and mechanical conditions of optical fiber in Raman and Brillouin processes, respectively.

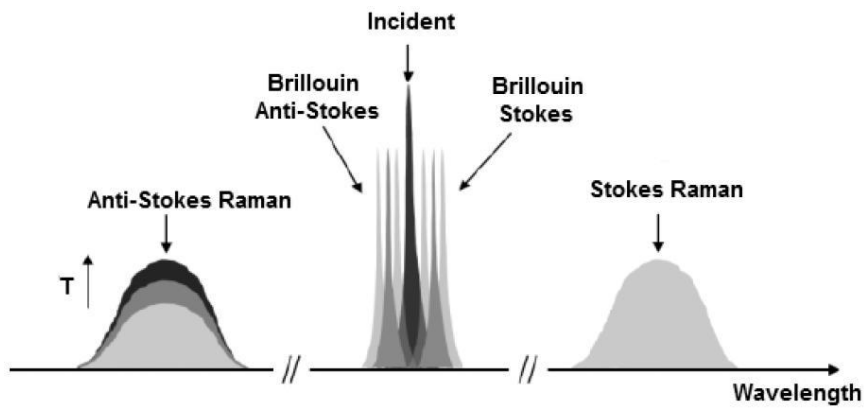


Figure-2.2: Emission spectrum of optical medium for Raman and Brillouin scattering

All energy transitions of photons and electrons in optical fibers obey the following physical laws crucial to understanding the processes

1. From conservation of energy stating that energy emission is the transition from higher energy levels (higher frequencies shorter wavelengths) to lower energy levels (lower frequencies longer wavelengths). For the Stokes wave and anti-Stokes we have:

$$\Omega = \omega_p - \omega_s \quad (2.1a)$$

$$\Omega = \omega_{as} - \omega_p \quad (2.1b)$$

2. Conservation of momentum stating that the propagation constant of a resulting wave equals the difference of the incident wave propagation constant and wavelength upshifted scattered wave. Again, for Stokes and anti-Stokes we have:

$$\vec{q} = \vec{k}_p - \vec{k}_s \quad (2.2a)$$

$$\vec{q} = \vec{k}_{as} - \vec{k}_p \quad (2.2b)$$

In case of Stimulated Brillouin Scattering (SBS) we will use two counter-propagating waves. In that case for Stokes we have:

$$q = \beta_p + \beta_s \quad (2.2c)$$

whereas for anti-Stokes we have:

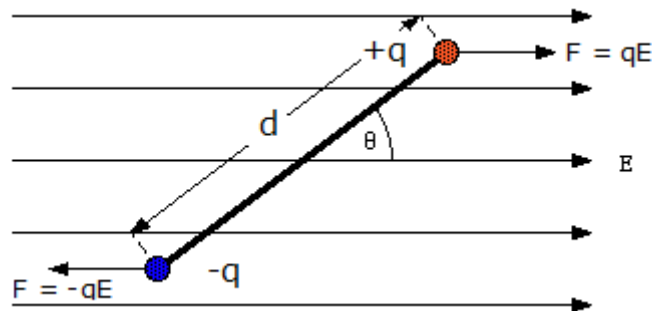
$$q = \beta_{as} + \beta_p \quad (2.2d)$$

Here $\beta_i = |\vec{k}_i|$.

The Pump and the Stokes waves will give rise to a low frequency beating wave that travels in the direction of that component having a larger frequency and shorter wavelength. The beating wave is the course of the acoustic wave that will be described here in more details.

2.1 Light in dielectric medium

In order to analyze physical phenomena of interaction of light with an optical medium, we must take a look at it on the microscopic scale. We consider a molecule subjected to an electrical field \mathbf{E} turning to polarization dipole and developing the electric dipole moment \vec{p} , as depicted in figure 5.3.



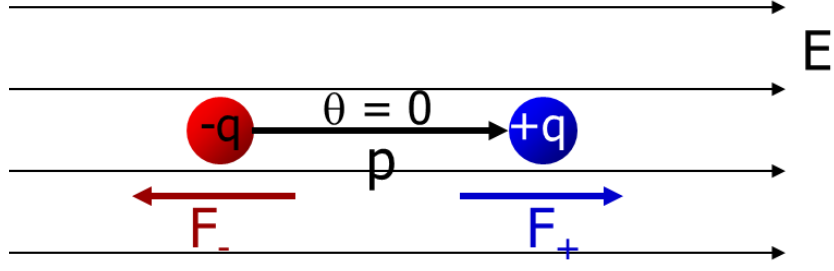


Figure-2.3: Mechanism of molecular polarization in electric field

The positive and negative microscopic charges are separated by an electrical force when a molecule is found in the electrical field. The concept of the molecular dipole moment \vec{p} can be defined as:

$$\vec{p} = q \cdot \vec{d} \quad (2.3)$$

where q is the charge of molecule and \vec{d} the displacement vector. Molecular polarizability α is 3x3 tensor characteristic of a medium. It links the electric dipole moment \vec{p} with the electrical field \vec{E} :

$$\vec{p} = \epsilon_0 \alpha \vec{E} \quad (2.4)$$

being in an E-field, it makes sense for a dipole to define its potential energy:

$$dU = -\vec{p} \cdot d\vec{E} \quad (2.5)$$

Therefore, the total work and potential energy stored is related to bringing the charges and dipole to the position and state of a uniform E-field \vec{E} :

$$U = - \int_0^E \vec{p} \cdot d\vec{E}' = -\frac{1}{2} \epsilon_0 \alpha E^2 \quad (2.6)$$

The force exerted on a single dipole/molecule can be calculated using the gradient of potential energy:

$$\vec{F} = -\nabla U = \frac{1}{2} \epsilon_0 \alpha \nabla(E^2) \quad (2.7)$$

The direction of force \vec{F} of a molecule dipole is in the direction of the increasing E-field.

This was from the microscopic point of view of a single molecule as a dipole. Now, for a much larger number of dipoles involved, we will continue with the derivation using the macroscopic point of view relevant to our case. Let us define a dipole moment per unit volume $\vec{P}(\vec{r})$ as:

$$\vec{P}(\vec{r}) = \sum_i N_i \langle \vec{p}_i \rangle \quad (2.8a)$$

$$\vec{P}(\vec{r}) = \chi \epsilon_0 \vec{E} \quad (2.8b)$$

where:

- $\langle \vec{p}_i \rangle$ is average dipole moment of the i -th of molecule making up the medium, and
- N_i is the average number of such molecules per unit volume in the vicinity of point \vec{r}
- χ is electrical susceptibility

The connection between molecular polarizability α and the dielectric constant is described by the Clausius-Mossotti relation:

$$\frac{\epsilon - 1}{\epsilon + 1} = \frac{N\alpha}{3\epsilon_0}. \quad (2.9)$$

Now, for very strong fields such as those generated by laser lights, electric polarization (dipole moment per unit volume) becomes nonlinear. The concept of electric polarization can be modelled by linear and nonlinear susceptibility using Taylor expansion applied to (2.4). $\chi^{(1)}$ represents linear susceptibility and all the others are nonlinear susceptibilities $\chi^{(n)}$, ($n > 1$). Therefore, the density of the dielectric medium and dielectric constant change and can be described with $\rho = \rho_0 + \Delta\rho$ and $\epsilon_r = \tilde{\epsilon}_r + \Delta\epsilon_r$ respectively. The link between change in the dielectric constant and change of density of the dielectric medium can be defined with the introduction of electro-strictive constant:

$$\Delta\epsilon = \frac{\delta\epsilon}{\delta\rho} \Delta\rho = \frac{1}{\rho_0} \zeta_e \Delta\rho \quad (2.10)$$

Where $\zeta_e = \rho_0 \left(\frac{\delta\epsilon}{\delta\rho} \right)$. It defines the amount of change in the dielectric constant due to change of density of the optical material. Electrostatic energy density inside dielectric medium is given by:

$$U = \frac{1}{2} \vec{E} \cdot \vec{D} = \frac{1}{2} \varepsilon_0 (\tilde{\varepsilon}_r + \Delta\varepsilon_r) E^2. \quad (2.11)$$

So, the change in electrostatic energy due to change of the dielectric constant is:

$$\Delta U = \frac{1}{2} E^2 \Delta\varepsilon = \frac{1}{2} \frac{\varepsilon_0 \zeta_e E^2}{\rho_0} \Delta\rho. \quad (2.12)$$

The work done per unit volume is:

$$\Delta W = p_{st} \frac{\Delta V}{V} = -p_{st} \frac{\Delta\rho}{\rho_0} \quad (2.13)$$

where p_{st} is stricitive pressure.

The change in energy must equal the work done or $\Delta U = \Delta W$. Therefore, we get the expression for stricitive pressure:

$$p_{st} = -\frac{1}{2} \varepsilon_0 \zeta_e E^2. \quad (2.14)$$

Stricitive pressure as a mechanical quantity cannot oscillate with the rate of the rapidly changing electrical field \vec{E} oscillation in terahertz ranges. The power (E^2) will have its low frequency components that can be followed by stricitive pressure. Therefore, in further analysis we will use the time averaged field:

$$p_{st} = -\frac{1}{2} \varepsilon_0 \zeta_e \langle E^2 \rangle. \quad (2.15)$$

Now we can relate force-per-unit-volume to the intensity of the electric field:

$$\mathbf{f} = \nabla p_{st} \quad (2.16)$$

$$\nabla \mathbf{f} = \nabla^2 p_{st} = -\frac{1}{2} \varepsilon_0 \zeta_e \nabla^2 \langle E^2 \rangle \quad (2.17)$$

Here we need to make a digression and dig into the analysis of an electrical field of a propagating wave:

1.2. Case study: two counter-propagating lightwaves

We have two lightwave counter-propagating;

- \vec{E}_p electrical field of pump wave propagating in +z direction

$$\vec{E}_p(z, t) = \vec{e}_p A_p \cos(\beta_p z - \omega_p t + \theta_p)$$

$$\vec{E}_p(z, t) = \vec{e}_p (\tilde{A}_p e^{i[\beta_p z - \omega_p t]} + \tilde{A}_p^* e^{-i[\beta_p z - \omega_p t]}) \quad (2.18)$$

- \vec{E}_s electrical field of Stokes wave propagating in -z direction

$$\vec{E}_s(z, t) = \vec{e}_s A_s \cos(-\beta_s z - \omega_s t + \theta_s)$$

$$\vec{E}_s(z, t) = \vec{e}_s (\tilde{A}_s e^{i[-\beta_s z - \omega_s t]} + \tilde{A}_s^* e^{-i[-\beta_s z - \omega_s t]}) \quad (2.19)$$

Where $\tilde{A}_p = A_p e^{i\theta_p}$, $\tilde{A}_s = A_s e^{i\theta_s}$ are phasors and $\beta_p = \frac{2\pi}{\lambda_1}$; $\beta_s = \frac{2\pi}{\lambda_2}$ are propagation constants.

Now the summing electrical field is:

$$|\vec{E}|^2 = |\vec{E}_p(z, t) + \vec{E}_s(z, t)|^2 = \quad (2.20)$$

$$= \left| \vec{e}_{p1} \frac{1}{2} (\tilde{A}_p e^{i[\beta_p z - \omega_p t]} + \tilde{A}_p^* e^{-i[\beta_p z - \omega_p t]}) + \vec{e}_{s1} \frac{1}{2} (\tilde{A}_s e^{i[-\beta_s z - \omega_s t]} + \tilde{A}_s^* e^{-i[-\beta_s z - \omega_s t]}) \right|^2$$

$$|\vec{E}|^2 =$$

$$= \left| \vec{e}_{p1} \frac{1}{2} \tilde{A}_p e^{i[\beta_p z - \omega_p t]} + \vec{e}_{p1} \frac{1}{2} \tilde{A}_p^* e^{-i[\beta_p z - \omega_p t]} + \vec{e}_{s1} \frac{1}{2} \tilde{A}_s e^{i[-\beta_s z - \omega_s t]} + \vec{e}_{s1} \frac{1}{2} \tilde{A}_s^* e^{-i[-\beta_s z - \omega_s t]} \right|^2$$

$$(2.21)$$

Physically only a few components fall into the detectable/measurable range;

1. rectification summands and
2. summands containing $(\omega_p - \omega_s)$

Therefore, we can continue:

$$|\vec{E}|^2 = |\tilde{A}_p \tilde{A}_p^* + \tilde{A}_s \tilde{A}_s^* + \xi (\tilde{A}_p \tilde{A}_s^* e^{i[(\beta_p + \beta_s)z - (\omega_p - \omega_s)t]} + c. c.)| \quad (2.22)$$

where $c. c.$ stands for complex conjugate. We have introduced the following substitutions:

- $\Omega = \omega_p - \omega_s$ being angular frequency of a new low frequency wave (phonon)
- $q = \beta_p + \beta_s$ being wavevector of low frequency slowly changing wave
- $\xi = (\vec{e}_p \cdot \vec{e}_s)$ is polarization efficiency

$$|\vec{E}|^2 = \left| \tilde{A}_p \tilde{A}_p^* + \tilde{A}_s \tilde{A}_s^* + 2\xi \frac{1}{2} (\tilde{A}_p \tilde{A}_s^* e^{i[qz - \Omega t]} + (\tilde{A}_p \tilde{A}_s^*)^* e^{-i[qz - \Omega t]}) \right|. \quad (2.23)$$

Written otherwise for electric field E :

$$|\vec{E}|^2 = \left| \underbrace{\tilde{A}_p \tilde{A}_p^* + \tilde{A}_s \tilde{A}_s^*}_{\text{Rectification}} + \underbrace{2\xi \tilde{A}_p \tilde{A}_s^* \cos(qz - \Omega t)}_{\substack{\text{Phonon with angular frequency} \\ \Omega = \omega_p - \omega_s}} \right| \quad (2.24a)$$

$$|\vec{E}|^2 = |A_p^2 + A_s^2 + 2\xi \tilde{A}_p \tilde{A}_s^* \cos(qz - \Omega t)|. \quad (2.24b)$$

The resulting optical power made by two counter-propagating lightwaves has the DC and AC component. The DC component is proportional to the sum of power of each wave, whereas the AC component is a wave that propagates in positive z direction. This power will interact with the optical medium and cause the change in stricive internal pressure that will, in turn, change the local density of the material. In other words, a phonon wave – an acoustical wave in ultrasonic frequency range is excited and will propagate in the medium.

$$\nabla \vec{f} = -\varepsilon_0 \zeta_e \xi \frac{\partial^2}{\partial z^2} (\tilde{A}_p \tilde{A}_p^* + \tilde{A}_s \tilde{A}_s^* + \tilde{A}_p \tilde{A}_s^* e^{i[qz - \Omega t]} + c. c.). \quad (2.25)$$

For the case in which amplitudes of the pump and Stokes wave change only slowly with distance, such as in optical fibers, the second derivative of the first two terms vanishes and (2.25) becomes:

$$\nabla \vec{f} \cong \varepsilon_0 \zeta_e \xi q^2 [\tilde{A}_p \tilde{A}_s^* e^{i(qz - \Omega t)} + c. c.]. \quad (2.26)$$

The result (2.26) tells us that divergence of force is a wave. This divergence exists only if q is non-zero as in the case of counter propagating waves. In fact, in such cases, the divergence of force is very strong, and it gives rise to the electrostriction effect even at lower levels of laser powers.

We will consider this wave in more detail using an example as follows:

Angular frequency of an acoustical wave is $\Omega = \omega_p - \omega_s$ and its wavenumber is $q = \beta_p + \beta_s$ for counterpropagating EM-waves. For standard telecommunication fibers the former can be taken to be 10.6GHz and the latter can be approximated with $q \cong 2 \beta_p$. Propagation constant β_p can be calculated for 1550nm as:

$$\beta_p = \frac{2\pi}{\lambda_0} n_1 = \frac{2 * 3.14}{1.55 \cdot 10^{-6}} 1.46 = 5.91 \frac{rad}{\mu m}.$$

Using $v\lambda = c$ we can calculate ω_p (v denotes frequency in optical frequency range):

$$\omega_p = 2\pi \frac{c}{\lambda_0} n_1 = 2 * 3,14 * 194.414 THz = 1215 \frac{Trad}{s}.$$

The propagating electromagnetic wave has the form:

$$\cos(\beta_p z - \omega_p t) = \cos(\beta_p v_p - \omega_p) t = \cos(\omega_p - \beta_p v_p) t$$

Inserting the values into the equation we get:

$$\cos\left(1215 \frac{Trad}{s} - \frac{5.91 rad}{\mu m} v_p\right) t.$$

We apply the same principle to the acoustic wave:

$$\cos(qz - \Omega t) = \cos(qv_p - \Omega) t = \cos(\Omega - qv_p) t$$

$$\cos\left(66,06 \frac{Grad}{s} - \frac{11.82 rad}{\mu m} v_p\right) t.$$

For the same z, t variables (and therefore also $v_p = \frac{z}{t}$) the above calculations show that the periodicity of the acoustic wave is by far longer than the one from the electromagnetic wave. In other words, for many periods of the electromagnetic wave, the acoustic wave can be taken as almost constant. This is beneficial and can be used in further analysis when spatial and time derivatives are considered.

2.2 Polarization nonlinearity of 2nd order

Dependence of (macroscopic dipole) polarization density (per-unit-volume) in the electric field consists of linear and nonlinear terms:

$$\vec{P} = \underbrace{\varepsilon_0 \chi^{(1)} \vec{E}}_{\text{Linear summand } \vec{P}_L} + \underbrace{\varepsilon_0 \chi^{(2)} \vec{E}^2 + \varepsilon_0 \chi^{(3)} \vec{E}^3 + \dots}_{\text{Serie of non-linear summands } \vec{P}_{NL}} \quad (2.27)$$

Where χ -s represent susceptibilities of the medium.

It shall be noted that both linear and non-linear terms are extensively used in modern optics in order to produce various effects useful in science and in industry. The electric displacement field \vec{D} is (by definition) dependent on the electric field and dipole polarization:

$$\vec{D} = \varepsilon_0 \vec{E} + \vec{P} = \varepsilon_0 \vec{E} + \varepsilon_0 \chi_0^{(1)} \vec{E} + \vec{P}_{NL} = \underbrace{\varepsilon_0 (1 + \varepsilon_0 \chi_0^{(1)})}_{\tilde{\varepsilon} = \varepsilon_0 \tilde{\varepsilon}_r} \vec{E} + \vec{P}_{NL} \quad (2.28)$$

$$\vec{D} = \tilde{\varepsilon} \vec{E} + \vec{P}_{NL} \quad (2.29)$$

where ε_0 is vacuum permittivity, and $\tilde{\varepsilon}$ permittivity of optical medium.

Taking that \vec{P}_{NL} for small amplitudes of \vec{E} can be approximated as:

$$\vec{P}_{NL} = \varepsilon_0 \Delta \varepsilon_r \vec{E} \quad (2.30)$$

where $\Delta \varepsilon_r$ is relative (to free space) permittivity of the optical medium.

Introducing the substitution $\Delta \varepsilon = \varepsilon_0 \Delta \varepsilon_r$ we get:

$$\vec{D} = \varepsilon_0 \tilde{\varepsilon}_r \vec{E} + \varepsilon_0 \Delta \varepsilon_r \vec{E} = \varepsilon_0 (\tilde{\varepsilon}_r + \Delta \varepsilon_r) \vec{E} \quad (2.31)$$

$$\vec{B} = \mu_0 \mu_r \vec{H}. \quad (2.32)$$

For a dielectric non-magnetic optical medium, as in our case, we take $\mu_r = 1$. Now applying the Maxwell equation to a non-magnetic dielectric optical medium:

$$\nabla \times \vec{E} = -\frac{\partial}{\partial t} \vec{B} \quad (2.33)$$

$$\nabla \times \vec{H} = \frac{\partial}{\partial t} \vec{D} \quad (2.34)$$

$$\nabla \times \vec{B} = \mu_0 \frac{\partial}{\partial t} \vec{D} = \mu_0 \varepsilon_0 \frac{\partial}{\partial t} [(\tilde{\varepsilon}_r + \Delta\varepsilon_r) \vec{E}] \quad (2.35)$$

Using substitution for $\mu_0 \varepsilon_0 = \frac{1}{c_0^2}$:

$$\nabla \times \vec{B} = \frac{1}{c_0^2} \left(\tilde{\varepsilon}_r \frac{\partial}{\partial t} \vec{E} + \frac{\partial}{\partial t} \vec{E} \Delta\varepsilon_r \right) \quad (2.36)$$

And now taking the derivative with respect to time:

$$\nabla \times \frac{\partial}{\partial t} \vec{B} = \frac{\tilde{\varepsilon}_r}{c_0^2} \frac{\partial^2}{\partial t^2} \vec{E} + \frac{\partial^2}{\partial t^2} \vec{E} \Delta\varepsilon_r. \quad (2.37)$$

Taking $\nabla \times \vec{E} = -\frac{\partial}{\partial t} \vec{B}$ and applying the rule $\nabla \times \nabla \times \vec{E} = -\nabla^2 \vec{E}$ we get:

$$\nabla^2 \vec{E} - \frac{\tilde{\varepsilon}_r}{c_0^2} \frac{\partial^2}{\partial t^2} \vec{E} = \frac{\partial^2}{\partial t^2} \vec{E} \Delta\varepsilon_r \quad (2.38)$$

Equation (2.38) describes propagation of the basic electromagnetic wave within a medium in a *weak* nonlinear operation mode.

2.3 Evolution of acoustic wave

So far, we have seen that optical power from two counter-propagating coherent beating electrical fields from lasers has its AC and DC components (2.24). This power will modulate density of the optical medium by the electro-striction mechanism. Further analysis continues using principles of hydrodynamics involving mass density and temperature as variables. Mass density of material due to electric field \vec{E} can be described with:

$$\rho_t(z, t) = \rho_0 + \Delta\rho \quad (2.39)$$

Where:

- ρ_0 is the equilibrium mass density of the medium
- $\Delta\rho$ is a varying part of $\rho_t(z, t)$ and can be described as a wave

$$\begin{aligned}\Delta\rho &= \rho_m \cos(qz - \Omega t + \Phi_\rho) = \\ &= \frac{1}{2} [\rho_m e^{i\Phi_\rho} e^{i(qz - \Omega t)} + \rho_m e^{-i\Phi_\rho} e^{-i(qz - \Omega t)}] = \tilde{\rho} e^{i(qz - \Omega t)} + c. c.\end{aligned}\quad (2.40)$$

Analogously we apply the same principle to pressure $p_t(z, t)$, temperature \tilde{T}_t and velocity \vec{v}_t . Pressure will be a periodic function, but temperature and velocity will not.

$$p_t(z, t) = p_0 + \Delta p \quad (2.41)$$

$$T_t(z, t) = T_0 + \Delta T \quad (2.42)$$

$$\vec{v}_t = \vec{v} \quad (2.43)$$

The rigorous analysis of an optical medium invokes principles and methods in fluid mechanics [1].

1. Equation of continuity

$$\frac{\partial \rho_t}{\partial t} + \nabla \rho_t \vec{v}_t = 0 \quad (2.44)$$

2. Equation of momentum transfer (conservation of momentum, generalization of Navier-Stokes equation)

$$\rho_t \frac{\partial}{\partial t} \vec{v}_t + \rho_t (\vec{v}_t \nabla) \vec{v}_t = \tilde{\mathbf{f}} - \nabla p_t + (2\eta_s + \eta_d) \nabla (\nabla \cdot \vec{v}_t) - \eta_s \nabla \times (\nabla \times \vec{v}_t) \quad (2.45)$$

3. Equation of heat transfer (conservation of energy)

$$\rho_t c_v \frac{\partial}{\partial t} \tilde{T}_t + \rho_t c_v (\vec{v}_t \nabla T_t) + \rho_t c_v \left(\frac{\xi - 1}{\beta_p} \right) (\nabla \cdot \vec{v}_t) = -\nabla \tilde{\mathbf{Q}} + \tilde{\phi}_n + \tilde{\phi}_{ext} \quad (2.46)$$

Where:

- $\tilde{\mathbf{f}}$ internally imposed forces per unit volume
- \vec{v}_t velocity of fluid *unit* volume
- η_s shear viscosity coefficient
- η_d dilatation viscosity coefficient
- c_v specific heat at constant volume

- $\zeta = \frac{c_p}{c_v}$ adiabatic index
- $\beta_p = -\frac{1}{\rho_0} \left(\frac{\partial \rho}{\partial T} \right)_p$ thermal expansion coefficient
- \tilde{Q} heat flux vector that satisfies $\nabla \tilde{Q} = -\kappa \nabla^2 T_t$
- $\tilde{\phi}_n$ viscous energy deposited per unit volume per unit time
- $\tilde{\phi}_{ext}$ viscous energy deposited from external sources per unit volume per unit time

In further analysis we will assume small amplitudes of varying parts compared to equilibrium states, that is:

$$|\rho_m| \ll \rho_0, |p_m| \ll p_0, |\Delta T| \ll T_0, |\vec{v}_t| \ll |v_a|$$

where v_a is the velocity of the acoustic wave (sound velocity).

Taken that p , ρ , and T are independent variables, correlation between them can be expressed as:

$$\Delta p = \left(\frac{\partial p}{\partial \rho} \right)_T \Delta \rho + \left(\frac{\partial p}{\partial T} \right)_\rho \Delta T \quad (2.47)$$

$$p = \frac{v_a^2}{\zeta} (\rho + \beta_p \rho_0 T). \quad (2.48)$$

Combining (2.46), (2.47), taking divergence on (2.48) and using (2.44) and (2.45) we obtain:

$$\frac{\partial^2}{\partial t^2} \rho - \frac{2\eta_s + \eta_d}{\rho_0} \nabla^2 \frac{\partial}{\partial t} \rho - \frac{v_a^2}{\zeta} \nabla^2 \rho - \frac{v_a^2}{\zeta} \beta_p \rho_0 \nabla^2 T = \nabla f. \quad (2.49)$$

Since temperature changes are very slow, the second derivate of temperature is very small and can be neglected. With the introduction of new substitutions, we get:

$$\frac{\partial^2}{\partial t^2} \rho - \Gamma' \nabla^2 \frac{\partial}{\partial t} \rho - v^2 \nabla^2 \rho = \nabla f \quad (2.50)$$

where:

- $\Gamma' = \frac{2\eta_s + \eta_d}{\rho_0}$ damping coefficient of acoustic wave
- $v^2 = \frac{v_a^2}{\zeta}$ effective speed of sound in the medium

Equation (2.50) now governs the mass density wave due to electro-strictive force that is a result of beating optical fields.

Implementing (2.25) and limiting (2.50) to z- axis only:

$$\frac{\partial^2}{\partial t^2} \rho - \Gamma' \frac{\partial^2}{\partial z^2} \frac{\partial}{\partial t} \rho - v^2 \frac{\partial^2}{\partial z^2} \rho = \varepsilon_0 \zeta_e \xi q^2 [\tilde{A}_p \tilde{A}_s^* e^{i(qz-\Omega t)} + c. c.]. \quad (2.51)$$

We have to combine (2.40) with (2.51). We need to work out all spatial and temporal derivatives. For the 1st time, derivative:

$$\frac{\partial}{\partial t} [\tilde{\rho} e^{i(qz-\Omega t)}] = \left(\frac{\partial}{\partial t} \tilde{\rho} - i \tilde{\rho} \Omega \right) e^{i(qz-\Omega t)}$$

and the 2nd time, derivative:

$$\begin{aligned} \frac{\partial^2}{\partial t^2} [\tilde{\rho} e^{i(qz-\Omega t)}] &= \frac{\partial}{\partial t} \left(\frac{\partial}{\partial t} [\tilde{\rho} e^{i(qz-\Omega t)}] \right) = \frac{\partial}{\partial t} \left(\frac{\partial}{\partial t} \tilde{\rho} - i \tilde{\rho} \Omega \right) e^{i(qz-\Omega t)} \\ &= \left[-i \Omega \left(\frac{\partial}{\partial t} \tilde{\rho} - i \tilde{\rho} \Omega \right) + \left(\frac{\partial^2}{\partial t^2} \tilde{\rho} - i \Omega \frac{\partial}{\partial t} \tilde{\rho} \right) \right] e^{i(qz-\Omega t)} \\ &= \left(\frac{\partial^2}{\partial t^2} \tilde{\rho} - 2i \Omega \frac{\partial}{\partial t} \tilde{\rho} - \Omega^2 \tilde{\rho} \right) e^{i(qz-\Omega t)} \end{aligned}$$

the 2nd spatial derivative:

$$\frac{\partial^2}{\partial z^2} [\tilde{\rho} e^{i(qz-\Omega t)}] = \frac{\partial}{\partial z} \left(\frac{\partial}{\partial z} [\tilde{\rho} e^{i(qz-\Omega t)}] \right) = \left(\frac{\partial^2}{\partial z^2} \tilde{\rho} + 2iq \frac{\partial}{\partial z} \tilde{\rho} - q^2 \tilde{\rho} \right) e^{i(qz-\Omega t)}.$$

Equation (2.50) now becomes:

$$\begin{aligned} &\left(\frac{\partial^2}{\partial t^2} \tilde{\rho} - 2i \Omega \frac{\partial}{\partial t} \tilde{\rho} - \Omega^2 \tilde{\rho} \right) e^{i(qz-\Omega t)} + \Gamma \nabla^2 \left[\left(\frac{\partial}{\partial t} \tilde{\rho} - i \tilde{\rho} \Omega \right) e^{i(qz-\Omega t)} \right] + \dots \\ &- v_a^2 \left(\frac{\partial^2}{\partial z^2} \tilde{\rho} + 2iq \frac{\partial}{\partial z} \tilde{\rho} - q^2 \tilde{\rho} \right) e^{i(qz-\Omega t)} = \varepsilon_0 \zeta_e \xi q^2 \tilde{A}_p \tilde{A}_s^* e^{i(qz-\Omega t)}. \end{aligned} \quad (2.52)$$

As we can see the equation (2.52) includes 1st and 2nd temporal and spatial derivatives. The phase elements suggest slow changes relative to fast alternating pumping and stokes fields. The fact is that mass density acts inertially and cannot follow fast changes of electromagnetic fields. Therefore, without losing generality, we can limit our analysis to the special case – slow varying

amplitude approximation (SVEA). This will be introduced in several steps. This means that from this point onward we shall assume that acoustic wave amplitude $\tilde{\rho}$ varies only slowly. We can instantly neglect all terms that involves derivatives of 2nd kind.

Nevertheless, in the first step we can introduce approximation to the term in which only the exponential part varies along z -axis and therefore 2nd derivate is small and it can be neglected:

$$\Gamma \nabla^2 \left[\left(\frac{\partial}{\partial t} \tilde{\rho} - i \tilde{\rho} \Omega \right) e^{i(qz - \Omega t)} \right] = -i \Gamma q^2 \Omega \tilde{\rho} e^{i(qz - \Omega t)}. \quad (2.53)$$

With this approximation (2.52) becomes:

$$\left(\frac{\partial^2}{\partial t^2} \tilde{\rho} - 2i\Omega \frac{\partial}{\partial t} \tilde{\rho} - \Omega^2 \tilde{\rho} \right) - v_a^2 \left(\frac{\partial^2}{\partial z^2} \tilde{\rho} + 2iq \frac{\partial}{\partial z} \tilde{\rho} - q^2 \tilde{\rho} \right) - i \Gamma q^2 \Omega \tilde{\rho} = \varepsilon_0 \zeta_e \xi q^2 \tilde{A}_p \tilde{A}_s^* \quad (2.54)$$

Regrouping the summands, we have:

$$\left(\frac{\partial^2}{\partial t^2} - v_a^2 \frac{\partial^2}{\partial z^2} \right) \tilde{\rho} - 2i\Omega \frac{\partial}{\partial t} \tilde{\rho} - (\Omega^2 - v_a^2 q^2 + i \Gamma q^2 \Omega) \tilde{\rho} - 2iv_a^2 q \frac{\partial}{\partial z} \tilde{\rho} = \varepsilon_0 \zeta_e \xi q^2 \tilde{A}_p \tilde{A}_s^* \quad (2.55)$$

We may now introduce the substitution $\Omega_B = v_a q$ and $\Gamma_B = \Gamma q^2$. Here Γ_B represents material specific Brillouin linewidth and it is corelated with photon lifetime with $\tau_p = \Gamma_B^{-1}$. Now, neglecting 2nd derivatives terms, which are rather very small, we obtain:

$$-2i\Omega \frac{\partial}{\partial t} \tilde{\rho} + (\Omega_B^2 - \Omega^2 - i \Gamma_B \Omega) \tilde{\rho} - 2iv_a^2 q \frac{\partial}{\partial z} \tilde{\rho} = \varepsilon_0 \zeta_e \xi q^2 \tilde{A}_p \tilde{A}_s^* \quad (2.56)$$

Equation (2.56) describes the propagation of the phonon wave. It has an exponential form and its strength is dependent on the product of magnitudes between the pump and the Stokes wave.

The term on the right $\varepsilon_0 \zeta_e q^2 \tilde{A}_p \tilde{A}_s^*$ dominates over $2iv_a^2 q \frac{\partial}{\partial z} \tilde{\rho}$ because phonon magnitude vanishes quickly with distance. If we consider a steady-state condition in which magnitude of density change does not vary with time, thus $\frac{\partial}{\partial t} \tilde{\rho} = 0$ we get the amplitude of the acoustic wave:

$$\tilde{\rho} = \varepsilon_0 \zeta_e q^2 \frac{\xi \tilde{A}_p \tilde{A}_s^*}{(\Omega_B^2 - \Omega^2 - i \Gamma_B \Omega)} \quad (2.57)$$

We see that the acoustic wave has a Lorentzian profile and will reach its maximum for $\Omega = \Omega_B$. It is also dependent on polarization efficiency ξ .

We return now to the analysis of (2.38). Combining equations (2.10) and (2.38) we can write:

$$\nabla^2 \vec{E} - \frac{\tilde{\epsilon}_r}{c_0^2} \frac{\partial^2}{\partial t^2} \vec{E} = \frac{\zeta_e}{\rho_0} \frac{\partial^2}{\partial t^2} (\vec{E} \Delta \rho) \quad (2.58)$$

(5.56) now needs to be evaluated. This can be done using phase matching conditions between the left- and right-hand sides. The overall electric field \vec{E} is the sum of two components \vec{E}_p and \vec{E}_s :

$$\vec{E} \Delta \rho = (\vec{E}_p + \vec{E}_s) \Delta \rho = \vec{E}_p \Delta \rho + \vec{E}_s \Delta \rho. \quad (2.59)$$

For the pump and the Stokes wave respectively, we have:

$$\nabla^2 \vec{E}_p - \frac{\tilde{\epsilon}_r}{c_0^2} \frac{\partial^2}{\partial t^2} \vec{E}_p + \nabla^2 \vec{E}_s - \frac{\tilde{\epsilon}_r}{c_0^2} \frac{\partial^2}{\partial t^2} \vec{E}_s = \frac{\xi_e}{\rho_0} \frac{\partial^2}{\partial t^2} (\vec{E} \Delta \rho) \quad (2.60)$$

Now we evaluate each term and apply phase matching criteria. We start from the right and first evaluate phase matching conditions on $\vec{E}_p \rho$ and $\vec{E}_s \rho$:

$$\vec{E}_p \Delta \rho = (\tilde{A}_p e^{i[\beta_p z - \omega_p t]} + \tilde{A}_p^* e^{-i[\beta_p z - \omega_p t]})(\tilde{\rho} e^{i(qz - \Omega t)} + \tilde{\rho}^* e^{-i(qz - \Omega t)}) \quad (2.61)$$

$$\begin{aligned} \vec{E}_p \Delta \rho &= \underbrace{\tilde{A}_p \tilde{\rho} e^{i[(q + \beta_p)z - (\omega_p + \Omega)t]}}_A + \underbrace{\tilde{A}_p^* \tilde{\rho} e^{i[(q - \beta_p)z - (\omega_p - \Omega)t]}}_B + \\ &+ \underbrace{\tilde{A}_p \tilde{\rho}^* e^{-i[(q - \beta_p)z + (\omega_p - \Omega)t]}}_C + \underbrace{\tilde{A}_p^* \tilde{\rho}^* e^{-i[(q + \beta_p)z - (\omega_p + \Omega)t]}}_D. \end{aligned} \quad (2.62)$$

Now the same for the $\vec{E}_s \Delta \rho$:

$$\vec{E}_s \Delta \rho = (\tilde{A}_s e^{-i[\beta_s z + \omega_s t]} + \tilde{A}_s^* e^{i[\beta_s z + \omega_s t]})(\tilde{\rho} e^{i(qz - \Omega t)} + \tilde{\rho}^* e^{-i(qz - \Omega t)})$$

$$\vec{E}_s \Delta \rho = \underbrace{\tilde{A}_s \tilde{\rho} e^{i[(q - \beta_s)z - (\omega_s + \Omega)t]}}_E + \underbrace{\tilde{A}_s^* \tilde{\rho} e^{i[(q + \beta_s)z + (\omega_s - \Omega)t]}}_F +$$

$$\underbrace{\tilde{A}_s \tilde{\rho}^* e^{i[(q+\beta_s)z+(\omega_s-\Omega)t]}}_G + \underbrace{\tilde{A}_s^* \tilde{\rho} e^{-i[(q-\beta_s)z-(\omega_s+\Omega)t]}}_H. \quad (2.63)$$

We name all the terms with the letters; A , B , C , D , E , F , G , and H . We check each term for phase matching conditions. It means they shall comply to (2.1) and (2.2) that represent basic laws of physics. For the pump wave we have $\beta_p = q - \beta_s$ and $\omega_p = \omega_s + \Omega$ so it is only the term labeled E and its complex conjugate H which meet phase matching conditions, whereas for the Stokes wave $\beta_s = q - \beta_p$ and $\omega_s = \omega_p - \Omega$ only C meets this condition. We may continue now with finding derivatives for both waves, first with spatial derivatives:

$$\begin{aligned} \nabla^2 \vec{E}_p &= \frac{\partial^2}{\partial z^2} (\tilde{A}_p e^{i[\beta_p z - \omega_p t]} + c. c.) = \frac{\partial}{\partial z} \left[\frac{\partial \tilde{A}_p}{\partial z} e^{i[\beta_p z - \omega_p t]} + i\beta_p \tilde{A}_p e^{i[\beta_p z - \omega_p t]} + c. c. \right] \\ &= \frac{\partial^2 \tilde{A}_p}{\partial z^2} e^{i[\beta_p z - \omega_p t]} + i\beta_p \frac{\partial \tilde{A}_p}{\partial z} e^{i[\beta_p z - \omega_p t]} \\ &\quad + i\beta_p \left(\frac{\partial \tilde{A}_p}{\partial z} e^{i[\beta_p z - \omega_p t]} + i\beta_p \tilde{A}_p e^{i[\beta_p z - \omega_p t]} \right) + c. c \\ \nabla^2 \vec{E}_p &= \left(\frac{\partial^2 \tilde{A}_p}{\partial z^2} + 2i\beta_p \frac{\partial \tilde{A}_p}{\partial z} - \beta_p^2 \tilde{A}_p \right) e^{i[\beta_p z - \omega_p t]} + c. c. \end{aligned} \quad (2.64)$$

We continue with temporal derivatives:

$$\begin{aligned} \frac{\partial^2}{\partial t^2} \vec{E}_p &= \left(\frac{\partial^2 \tilde{A}_p}{\partial t^2} - 2i\omega_p \frac{\partial \tilde{A}_p}{\partial t} - \omega_p^2 \tilde{A}_p \right) e^{i[\beta_p z - \omega_p t]} \\ \frac{\partial}{\partial t} \left[\frac{\partial}{\partial t} (\tilde{A}_s \tilde{\rho} e^{i[\beta_p z - \omega_p t]} + c. c.) \right] &= \left(\frac{\partial^2 \tilde{A}_s \tilde{\rho}}{\partial t^2} - 2i\omega_p \frac{\partial \tilde{A}_s \tilde{\rho}}{\partial t} - \omega_p^2 \tilde{A}_s \tilde{\rho} \right) e^{i[\beta_p z - \omega_p t]} + c. c. \end{aligned} \quad (2.65)$$

This brings the following form of the pump wave:

$$\begin{aligned} \left(\frac{\partial^2 \tilde{A}_p}{\partial z^2} + 2i\beta_p \frac{\partial \tilde{A}_p}{\partial z} - \beta_p^2 \tilde{A}_p \right) - \frac{\tilde{\epsilon}_r}{c_0^2} \left(\frac{\partial^2 \tilde{A}_p}{\partial t^2} - 2i\omega_p \frac{\partial \tilde{A}_p}{\partial t} - \omega_p^2 \tilde{A}_p \right) &= \\ = \frac{\tilde{\xi}_e}{\rho_0} \left(\frac{\partial^2 \tilde{A}_s \tilde{\rho}}{\partial t^2} - 2i\omega_p \frac{\partial \tilde{A}_s \tilde{\rho}}{\partial t} - \omega_p^2 \tilde{A}_s \tilde{\rho} \right). \end{aligned} \quad (2.66)$$

We assume again that amplitude varies only slowly in time and space, as follows:

- $\frac{\partial^2 \tilde{A}_p}{\partial z^2}$, $\frac{\partial^2 \tilde{A}_p}{\partial t^2}$ and $\frac{\partial^2 \tilde{A}_s \tilde{\rho}}{\partial t^2}$ are very small and can be neglected

- $2\omega_p \frac{\partial \tilde{A}_s \tilde{\rho}}{\partial t}$ is small compared to $\omega_p^2 \tilde{A}_s \tilde{\rho}$ and can be omitted.
- $\frac{\partial \tilde{A}_p}{\partial z}$ and $\frac{\partial \tilde{A}_p}{\partial t}$ describe change of amplitude with z and t

So (2.66) transforms into a simpler form:

$$\left(2i\beta_p \frac{\partial \tilde{A}_p}{\partial z} - \beta_p^2 \tilde{A}_p\right) + \frac{\tilde{\epsilon}_r}{c_0^2} \left(2i\omega_p \frac{\partial \tilde{A}_p}{\partial t} + \omega_p^2 \tilde{A}_p\right) = -\frac{\zeta_e}{\rho_0} \omega_p^2 \tilde{A}_s \tilde{\rho}. \quad (2.67)$$

Taking $n_c = \sqrt{\tilde{\epsilon}_r}$ and $\beta_p = \frac{\omega_p}{c_0} n$ leading to $\omega_p^2 = \beta_p^2 c_0^2 \frac{1}{n_c^2}$, thus we have:

$$\left(2i\beta_p \frac{\partial \tilde{A}_p}{\partial z} - \beta_p^2 \tilde{A}_p\right) + \frac{n_c^2}{c_0^2} \left(2i\omega_p \frac{\partial \tilde{A}_p}{\partial t} + \beta_p^2 c_0^2 \frac{1}{n_c^2} \tilde{A}_p\right) = -\frac{\zeta_e}{\rho_0} \omega_p^2 \tilde{A}_s \tilde{\rho}. \quad (2.68)$$

After manipulation of the summands we finally obtain the form describing the pump wave:

$$\frac{\partial \tilde{A}_p}{\partial z} + \frac{n_c}{c_0} \frac{\partial \tilde{A}_p}{\partial t} = i \frac{\zeta_e \omega_p}{n_c \rho_0} \tilde{\rho} \tilde{A}_s. \quad (2.69)$$

We use the same procedure for the Stokes wave:

$$-\frac{\partial \tilde{A}_s}{\partial z} + \frac{n_c}{c_0} \frac{\partial \tilde{A}_s}{\partial t} = i \frac{\zeta_e \omega_p}{n_c \rho_0} \tilde{\rho}^* \tilde{A}_p. \quad (2.70)$$

From both equations we can see the exponential dependence of amplitude with length. The exponential growth of the pump wave is dependent on the product of density change and Stokes wave magnitudes, whereas the Stokes wave is dependent on the product of density change and pump wave magnitudes. In other words, the equations are coupled as magnitudes of both optical waves which are mutually dependent.

Stimulated Brillouin effect within a lossless medium is fully described with (2.56), (2.69) and (2.70). Using (2.57) equations (2.69) and (2.70) can be written in a simpler form. If we defined intensities as $I_i = 2n\epsilon_0 \tilde{A}_i \tilde{A}_i^*$, multiply (2.69) and (2.70) with \tilde{A}_p^* and \tilde{A}_s^* respectively, and then applied identities:

$$\frac{\partial(\tilde{A}_p \tilde{A}_p^*)}{\partial u} = \tilde{A}_p^* \frac{\partial \tilde{A}_p}{\partial u} + \tilde{A}_p \frac{\partial \tilde{A}_p^*}{\partial u}$$

$$\frac{\partial(\tilde{A}_s \tilde{A}_s^*)}{\partial u} = \tilde{A}_s^* \frac{\partial \tilde{A}_s}{\partial u} + \tilde{A}_s \frac{\partial \tilde{A}_s^*}{\partial u}$$

where $u = z, t$. Then (2.69) and (2.70) would take the simpler form:

$$\left[\frac{n_c}{c_0} \frac{\partial}{\partial t} + \frac{\partial}{\partial z} \right] I_P = -g_B I_P I_S \quad (2.71)$$

$$\left[\frac{n_c}{c_0} \frac{\partial}{\partial t} - \frac{\partial}{\partial z} \right] I_S = -g_B I_P I_S \quad (2.72)$$

Where g_B is Brillouin gain with frequency difference $f_D = f_s - f_B$ between Stokes frequency and central frequency f_B (frequency of the peak):

$$g_B = \xi \cdot g_{Bmax} \frac{1}{1 + 4 \left(\frac{f_D - f_B}{\Delta f_B} \right)^2} \quad (2.73)$$

$$g_{Bmax} = \frac{2\pi^2 n^7 p_{12}^2}{c \lambda^2 \rho_0 \xi_S c_S} \quad (2.74)$$

Where:

- n - refractive index of core
- c - speed of light
- λ - wavelength in vacuum
- p_{12} - electrostriction coefficient
- ρ_0 – average mass density
- ξ_S - acoustic attenuation coefficient
- g_{Bmax} – maximum gain coefficient at zero detuning
- $f_D = f_p - f_s$ - frequency difference/distance between pump and Stokes light
- f_B - peak frequency of Brillouin profile

- Δf_B - bandwidth (full width at half maximum - FWHM) of Brillouin gain profile
- c_S - speed of acoustic wave

2. FIBER OPTIC PRESSURE SENSING CABLE

This chapter introduces a sensor cable that is, for the time being, commercially available for distributed strain and acoustic measurements. It also introduces and discusses technical possibilities for fully distributed pressure (DPS) measurements. Without any doubts, DPS measurement, the truly fully distributed version of it, represents a major technical challenge, not only for sensor cable construction but also for interrogation methods. Therefore, the intentions and objectives in this chapter are the following:

- propose and discuss DPS cable candidates with intrinsic birefringence change capability
- propose DPS interrogation methods based on stimulated Brillouin scattering technique.

The industrial potential for fully distributed pressure sensing systems using birefringence change techniques [26], [30], [31], [56] is generally believed to be enormous. Since strain and temperature measurements are available in industry, it represents the missing piece in the world of fully distributed measurements. For the purpose of distributed pressure measurements, both approaches - the Brillouin and Rayleigh backscattering measurement methods qualify for the call. Because of availability of the DTSS unit (Omnisens Ditest) [18] and experience gained in previous years in working with both systems, only stimulated Brillouin techniques are the focus of discussion here.

2.1. Sensing cable construction and verification methods

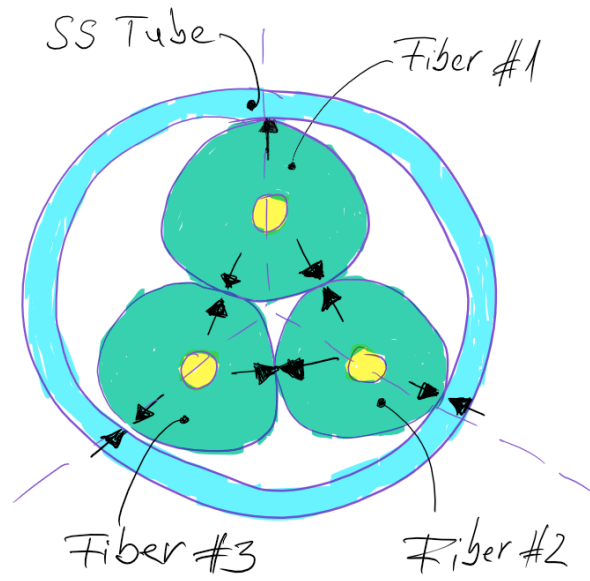
Stainless steel tubing (SST) in its various forms is traditionally used for production of optical power ground wire where it was used for telecommunication exchange in power transmission systems, i.e. in overhead power lines. The other application in industry is subsea telecommunication lines. These are traditional industries for which laser welded tubes with optical fibers are produced. This sort of tubing is proven to provide quality protection for numerous applications, rather than the fragile and sensitive optical tubing. Such an application is measurement and sensing in harsh environments such as geophysical downhole applications. Because of its metallic nature, SST exhibits intrinsically large thermal conductivity providing easy and fast thermal energy transmission through the walls of the SST. Another advantage is that optical fibers enclosed in SST – referred to as Fiber in Metal Tube (FIMT) - can survive harsh environmental conditions, such as in aggressive chemical and mechanically demanding

conditions. This counts especially for down-hole applications where pressure and temperature ranges exceed 900 bar and 350°C, respectively.

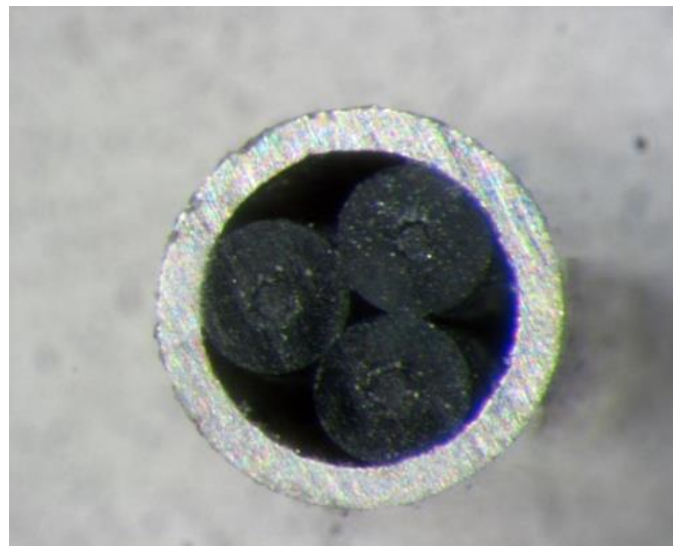
The proposed sensor cable consists of three optical fibers (Fig.-3.1), positioned at 120° in a cross-section azimuthal plane and tightly encapsulated in a metal tubing by means of FIMT (Fiber in Metal tube) production machinery using the laser welding technique. An industrial version is shown in Fig.-3.2. Tight encapsulation here means that all fibers are in physical contact with the metal tubing on top. The amount of physical contact in terms of pressure between optical fibers and the inner wall of the metallic tubing can be regulated during the production process. The basic idea for this design is to arrange tight-buffer construction producible with three fibers in long lengths. All three fibers must be in optimum contact with the steel encapsulation on top of it. Information on the quality of contact and all parameters can be obtained from various measurements. Two techniques are particularly useful; Rayleigh backscattering using Optical Time Domain Reflectometry (OTDR) [62] and acoustics measurement techniques such as Brillouin Optical Time Domain Analysis (BOTDA) [47], [48]. Our interests are the spatial Brillouin-Lorentzian profile and its parameters. From the pressure measurement point of view, both the mechanical and optical properties are equally important and need to be addressed in this technical challenge. Inside the construction optical fiber is clamped in the position and touching the inner wall of the tube. It is surrounded by two voids and two other adjacent fibers. Hence, it is subjected to three forces on its circumference; one from encapsulation tubing and the other two - one from each adjacent fiber.

2.2. Three optical fibers working together

The cable consists of three optical fibers (Fig.-3.1) positioned at 120° in a cross-section azimuthal plane and tightly encapsulated in metal tubing by means of FIMT production machinery using the laser welding technique. The amount of physical contact in terms of pressure between optical fibers and the inner wall of the metallic tube can be regulated during the production process. The basic idea for this design is to arrange tight-buffer construction with three fibers with such stability in the production process that it can be produced in long lengths. Therefore, all three fibers must be in optimum contact with the steel encapsulation on top of it, not too much - as it introduces additional losses, and not too little as it stops transferring exterior measurands to inner optical fibers.



(a)



(b)

Figure-3.1: Cable prototype with overall diameter 1.25mm; the initial sketch (a) and the prototype (b)

The information on the quality of contact, together with all other pressure parameters, can be obtained from measurements that can vary.

Pressure measurement, the one with good accuracy, brings mechanical and optical properties of the cable to our focus. They are equally important for a successful outcome. In order to assure the change of birefringence, the configuration must provide asymmetrical loading to each fiber. The concept is depicted in Fig.-3.2. Hydrostatic pressure exerts the loads to the round tube, all

that homogenously along the circumference. The tube, in turn, exerts asymmetrical load to round optical fibers inside the tube.

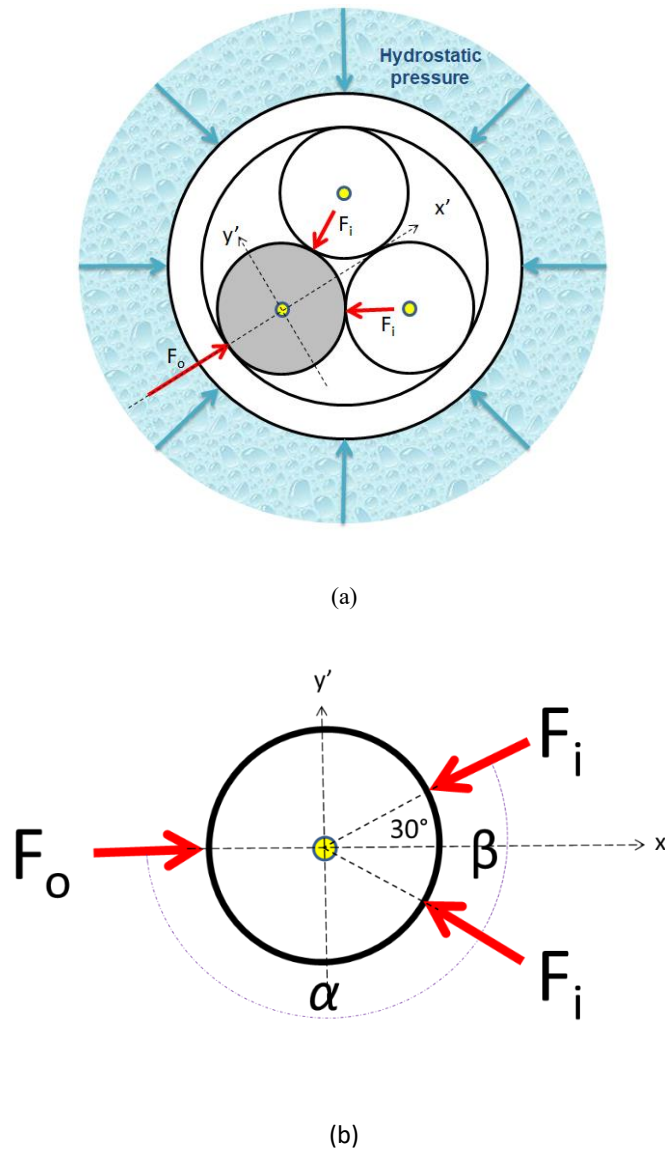


Figure-3.2: Concept of a sensor cable based on three optical fibers encapsulated in a metal or plastic jacket; (a) cable design, (b) configuration of forces exerted on optical fiber.

The fiber under consideration is fixed and ‘sandwiched’ into the position by surrounding encapsulation tubing and two others adjacent fibers. Thus, it shall see three forces exerted on its circumference; one from encapsulation tubing and one from each adjacent fiber. Consequently, in static equilibrium we will have:

$$\sum_i F_{xi} = 0; \sum_i F_{yi} = 0 \quad (3.1)$$

For the x'-axis we have:

$$F_o - 2F_i \cos(30^\circ) = 0 \quad (3.2)$$

$$F_o = \sqrt{3}F_i \quad (3.3)$$

The same analysis approach for y'-axis gives:

$$0 + F_i \sin(30^\circ) - F_i \sin(30^\circ) = 0 \quad (3.4)$$

In other words, y' components are cancelled.

Because $F_o = \sqrt{3}F_i$ in x'-axis and 0 in y'-axis we can now say that the fiber is asymmetrically loaded. This gives rise to birefringence in the core of the optical fiber as pressure increases. In this way birefringence as an asymmetrical phenomenon is generated by means of symmetrical elements that are easily available in industry.

2.3. Optical loss consideration for cable design

From the optical performance point of view, the first and most important technical requirement is that the design can be manufactured in a very long length without introducing additional losses but with good repetition. Fig.-3.3 shows fiber attenuation (i.e. losses) results from the optical time domain measurement (OTDR Exfo FTB-500). The measurements show average attenuation of 0.347 dB/km at 1310nm and 0.20 dB/km at 1550nm and 0.211dB/km at 1625nm from all three fibers, respectively. It proves that the design does not introduce significant additional losses and they are within an acceptable range and comparable with uncabled optical fiber.

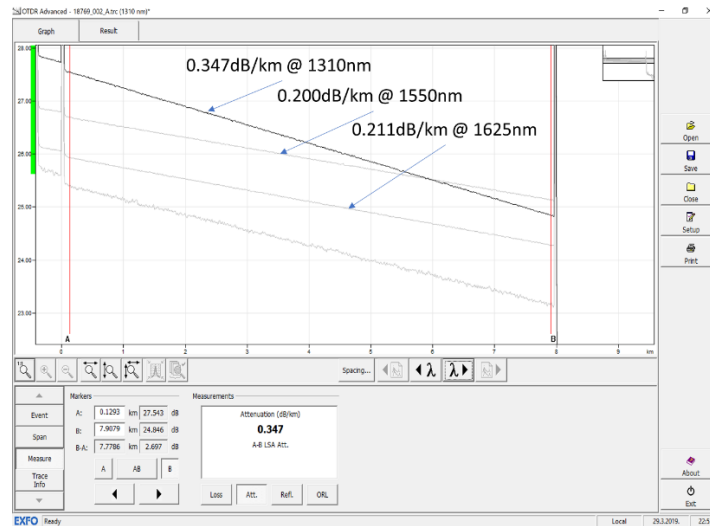


Figure-3.3: Characteristic losses obtained from all three fibers of the prototype, each at different wavelength; (a) fiber-1 @ 1310nm, (b) fiber-2 @ 1550nm and (c) fiber-3 @ 1625nm.

2.4. Validation of impact on birefringence and pressure sensitivity using FEM

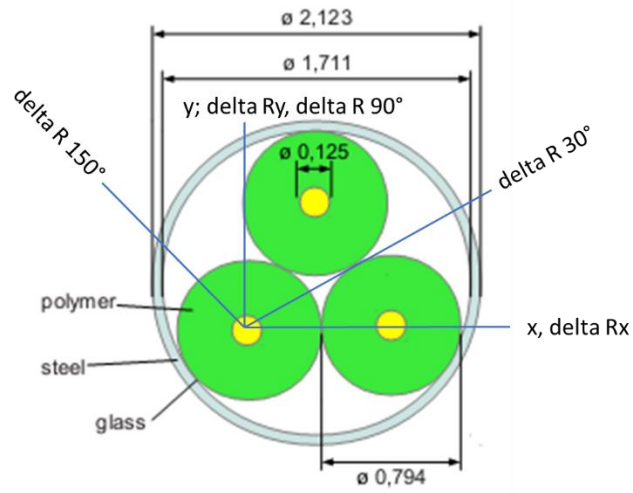
From the mechanical perspective, the concept can be validated using FEM - Finite Element Method. For this purpose, Abacus simulation software has been used. The analysis has been made on a relatively large design (Fig.-3.4) with an outer diameter (OD) of 2.213mm and wall thickness (WT) of approximately 0.25mm. Young modulus (E) and Poisson ratio (ν) along with other parameters and information of interest are:

Parameters used for FEM:

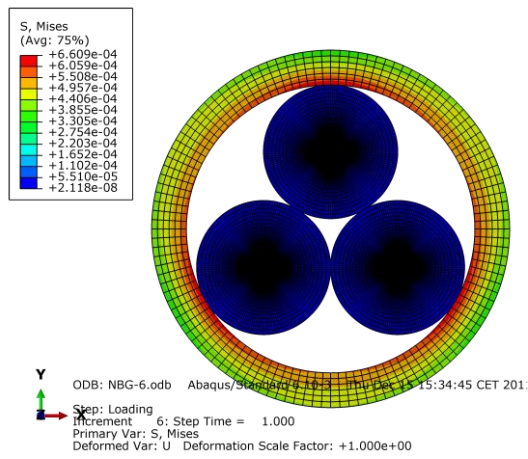
- Steel: $E = 210$ GPa, $\nu = 0.30$
- Polymer: $E = 2.7$ GPa, $\nu = 0.34$
- Loads: static pressure, magnitude up to 1200 bars
- Finite element type: plane strain, quadratic, reduced integration (CPE8R)

Evaluated parameters:

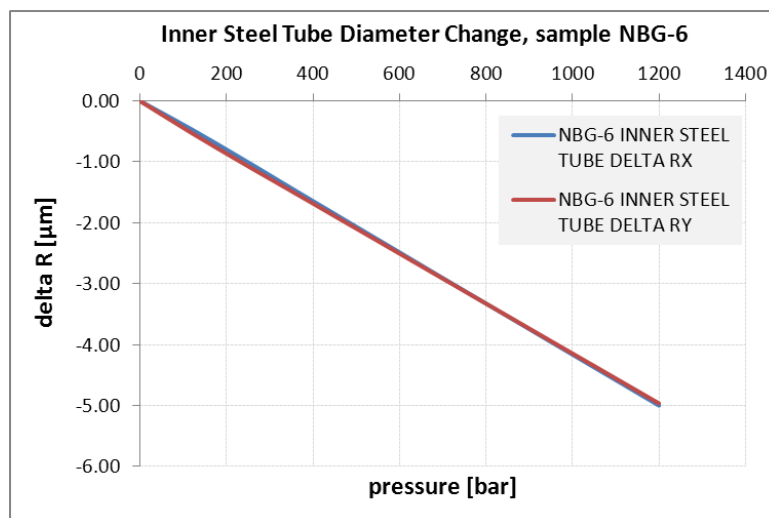
- Inner diameter changes of steel tube (ΔR_x , ΔR_y)
- Outer diameter changes of optical fiber (ΔR_x , ΔR_y , $\Delta R_{30^\circ/90^\circ/150^\circ}$)



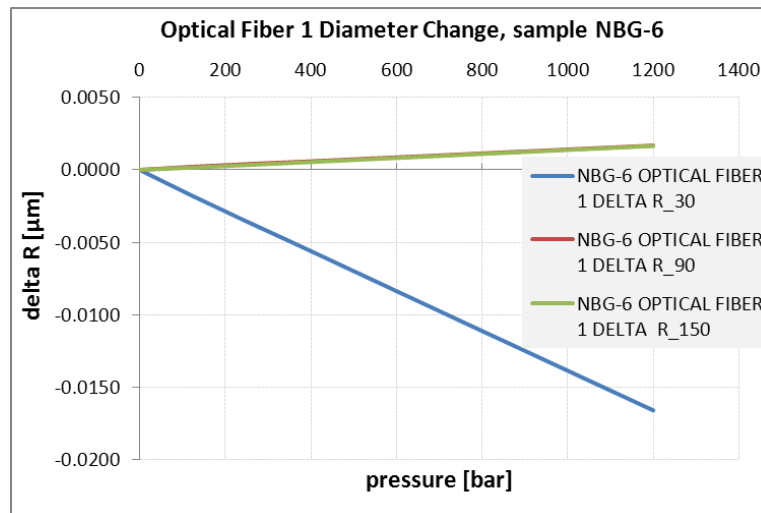
(a)



(b)



(c)



(d)

Figure-3.4: Validation using Finite Element Method (FEM) applied to cable; (a) geometry with dimensions and observation angles, (b) FEM mesh configuration with legend showing pressure magnitudes in TPa, (c) change in inner diameter, and (d) radial deformation of fiber-1 due to asymmetrical loading obtained at observed angles.

Note that lines for angles 90° and 150° almost overlap.

The results for fiber-1 are shown in Fig.-3.4a. As it can be seen from it, FEM analysis confirms the assumption of asymmetrical loading. The results provide also insight in magnitudes of tube compression for pressure up to 1200 bar. The analysis is taken at different angles on the fiber circumference. They give magnitude of fiber radial compression at an angle of 30° and radial extension at angles 90° and 150°. Note that the considered angles 90° and 150° are between the angles for which fiber-1 is in contact with the metal tube and the other fibers inside the tube (0° and 60°, respectively).

2.5. Validation using polarization measurements and Stokes parameters

The first optical validation can be conducted using the straight-through polarimetric technique [5,6]. In our case, the birefringent element is the length of cables that is pressurized on its circumference. This method offers also a neat method to observe and trace the changes by means of the Poincare sphere approach that fully describes polarization states of light and as the output of the sample. The projections of the electric field vector $\vec{E}(z, t)$ on fast and slow axis of the birefringent fiber are:

$$e_x(z, t) = E_{0x} \cos(\omega t - kz + \delta_x) \quad (3.5a)$$

$$e_y(z, t) = E_{0y} \cos(\omega t - kz + \delta_y) \quad (3.5b)$$

$$\delta = \delta_x - \delta_y \quad (3.6a)$$

$$\delta_x = \Delta k_x z + \phi_x \quad (3.6b)$$

$$\delta_y = \Delta k_y z + \phi_y. \quad (3.6c)$$

Here we have put all asymmetric effects into δ_x and δ_y (difference in propagation constants, phases at the input). Hence, k represents the average propagation constant. We introduce substitution with $\tau = \omega t - kz$ - the propagator:

$$e_x(z, t) = E_{0x} \cos(\tau + \delta_x) \quad (3.7a)$$

$$e_y(z, t) = E_{0y} \cos(\tau + \delta_y) \quad (3.7b)$$

$$\frac{e_x}{E_{0x}} = \cos(\tau)\cos(\delta_x) - \sin(\tau)\sin(\delta_x) \quad (3.8a)$$

$$\frac{e_y}{E_{0y}} = \cos(\tau)\cos(\delta_y) - \sin(\tau)\sin(\delta_y) \quad (3.8b)$$

$$\frac{e_x}{E_{0x}} \sin(\delta_y) - \frac{e_y}{E_{0y}} \sin(\delta_x) = \cos(\tau)\sin(\delta_x - \delta_y) \quad (3.9a)$$

$$\frac{e_x}{E_{0x}} \cos(\delta_y) - \frac{e_y}{E_{0y}} \cos(\delta_x) = \cos(\tau)\sin(\delta_x - \delta_y) \quad (3.9b)$$

Squaring equations and adding them together gives:

$$\frac{e_x^2}{E_{0x}^2} + \frac{e_y^2}{E_{0y}^2} - 2 \frac{e_x}{E_{0x}} \frac{e_y}{E_{0y}} \cos(\delta) = \sin^2(\delta) \quad (3.10)$$

We can notice that the propagator has been excluded in the last manipulation. The equation describes the relation between quantities of the electromagnetic wave independent of the propagator. The only variables dependent on time and position along z-axis are e_x and e_y . The beauty of this equation is that the squared forms and multiplication products of these variables

are observables of the optic field and they can be measured easily because they represent optical power (more precisely power density). Therefore, it is necessary to find a way of expressing equation (3.7) in terms of the observables. Using multiplication products means taking the average over the time of observation. Since e_x and e_y are time dependent and the averaging can be done over a long period of time

$$\langle e_i(t)e_j(t) \rangle = \lim_{T \rightarrow \infty} \frac{1}{T} \int_0^T e_i(t) e_j(t) dt \quad i, j = x, y$$

Because e_x and e_y are periodic, it would be enough to take just one period for averaging. Thus, taking the average of (3.7) we get:

$$\langle e_x^2(t) \rangle = \frac{1}{2} E_{0x}^2 \quad (3.11a)$$

$$\langle e_y^2(t) \rangle = \frac{1}{2} E_{0y}^2 \quad (3.11b)$$

$$\langle e_x(t)e_y(t) \rangle = \frac{1}{2} E_{0x}E_{0y}\cos\delta \quad (3.12)$$

Multiplying (3.10) with $4E_{0x}E_{0y}$ we obtain:

$$4E_{0y}^2\langle e_x^2(t) \rangle + 4E_{0x}^2\langle e_y^2(t) \rangle - 8E_{0x}E_{0y}\langle e_x(t)e_y(t) \rangle \cos\delta = (2E_{0x}E_{0y}\cos\delta)^2 \quad (3.13)$$

Substituting (3.11) and (3.12) into (3.13) yields:

$$(E_{0x}^2 + E_{0y}^2)^2 - (E_{0x}^2 - E_{0y}^2)^2 - (2E_{0x}E_{0y}\cos\delta)^2 = (2E_{0x}E_{0y}\sin\delta)^2 \quad (3.14)$$

Now, we can introduce new substitutions related to the so-called Stokes parameters [36]-[38]

$$S_0 = E_{0x}^2 + E_{0y}^2 \quad (3.15a)$$

$$S_1 = E_{0x}^2 - E_{0y}^2 \quad (3.15b)$$

$$S_2 = 2E_{0x}E_{0y}\cos\delta \quad (3.15c)$$

$$S_3 = 2E_{0x}E_{0y}\sin\delta \quad (3.15d)$$

Thus, (3.14) can be now rewritten as:

$$S_0^2 = S_1^2 + S_2^2 + S_3^2 \quad (3.16)$$

These Stokes parameters (named after Sir George Gabriel Stokes) describe distribution of light energy into different polarization states by means of optical field observable – the power of light. S_0 is the sum of power in both orthogonal axis and represents the total power of light, S_1 is the difference of power in both axes. Both S_0 and S_1 bear information on linear polarizations only, and S_2 and S_3 are powers that include phase difference – phase retardation - between the axes giving rise to elliptical and circular polarizations. Now, they can be rewritten in a slightly different form, i.e. the complex form:

$$S_0 = E_x E_x^* + E_y E_y^* \quad (3.17a)$$

$$S_1 = E_x E_x^* - E_y E_y^* \quad (3.17b)$$

$$S_2 = E_x E_y^* + E_y E_x^* \quad (3.17c)$$

$$S_3 = i(E_x E_y^* - E_y E_x^*) \quad (3.17d)$$

Here $E_x = E_{0x} e^{j\delta_x}$ and $E_y = E_{0y} e^{j\delta_y}$ represent complex amplitudes of e_x and e_y or phasors, respectively. Stokes parameters form the so called Stokes vector $S = [S_0 \ S_1 \ S_2 \ S_3]^T$. Stokes parameters can be further normalized with S_0 . In such case they are called normalized Stokes parameters and each polarization state can be described with a vector $S_n = [S_1 \ S_2 \ S_3]^T$. The normalized Stokes parameters span spherical vector space, the so called Poincare sphere, with radius 1. The Poincare sphere shows polarization states of light. The rotation and trace of the sphere shows all the change of actual State-Of-Polarization (SOP) due to perturbation exerted to the optical medium or sample. These perturbations can be of different types, such as:

- mechanical – influence of twist, strain and pressure
- thermal – change of temperature of fiber and thus its polarization parameters
- optical – refractive index, phase and wavelength change

For the principle validation purpose of the pressure impact on birefringence, measurement polarimetric set-up was arranged (Fig.-3.5) in which polarimetric properties of fiber and cables

samples are measured and characterized. The sample of a sensor cable is brought through a 24m long chamber and then sealed on both ends and pressurized using silicon oil. As a light source, the coherent laser source (Yenista Tunics 100R) is used and input polarization state was set to linear vertical polarization. On the receiver side, polarimeter (Thorlabs PAX 1000) measures polarization states and shows them in the form of a Stokes parameters curve. The rotation of SOP at Poincare sphere combines integrating features of more devices into one: the passive polarization analyzer, optoelectrical converter and power measurement and visualization in one single unit. After installation and sealing, the sample is subjected to pressure increase from 0 to 800bar in steps of 100bar. The total length of the sample is around 24m.

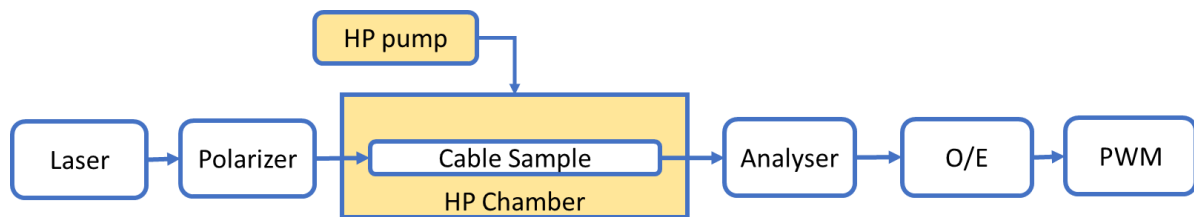


Figure-3.5: Polarimetric measurement set-up integrating pressure chamber in which cable samples were set and sealed

Table-3.1 lists the Stokes parameters acquired and Fig.-3.6 depicts the changes of SOP by means of rotation of the Poincare sphere.

TABLE-3.1: THE CHANGE OF STOKES PARAMETERS WITH PRESSURE RATE

Pressure rate [bar]	0.00	25.00	50.00	75.00	100.00
S1	-0.78	-0.82	-0.90	-0.90	-0.85
S2	-0.12	-0.04	0.10	0.33	0.52
S3	-0.61	-0.57	-0.42	-0.29	-0.10
Pressure rate [bar]		125.00	150.00	175.00	200.00
S1		-0.70	-0.47	-0.42	-0.55
S2		0.70	0.84	0.83	0.74
S3		0.09	0.27	0.36	0.40
Pressure rate [bar]		225.00	250.00	275.00	300.00
S1		0.19	0.62	0.76	0.40
S2		0.82	0.74	0.58	0.25
S3		0.53	0.25	-0.28	-0.88
Pressure rate [bar]		325.00	350.00	375.00	400.00

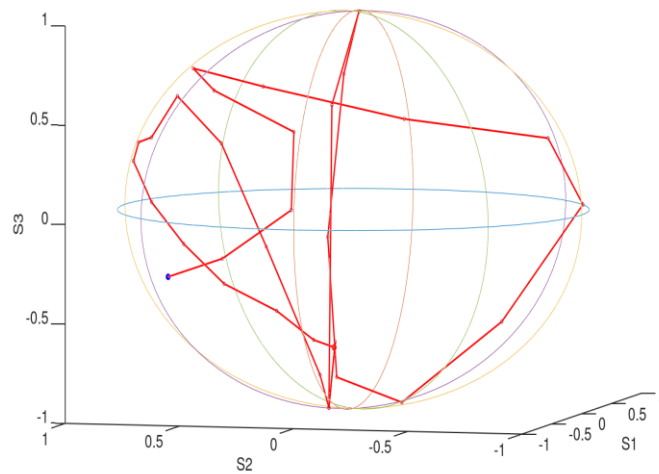
S1	-0.18	-0.80	-0.18	-0.78
S2	0.06	-0.13	0.06	-0.11
S3	-0.98	-0.58	-0.98	0.61

Pressure rate [bar]		425.00	450.00	475.00	500.00
S1		-0.02	0.76	0.91	0.41
S2		-0.03	0.24	0.35	0.18
S3		1.00	0.60	-0.24	-0.89

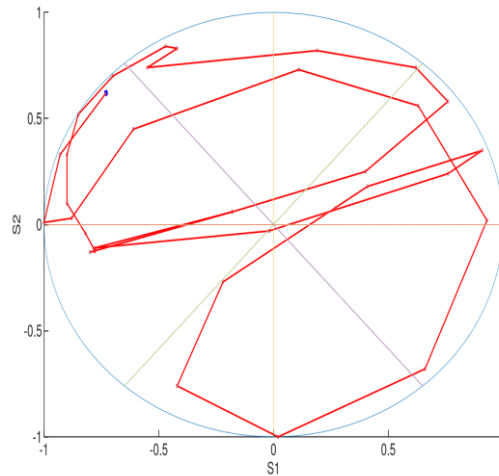
Pressure rate [bar]		525.00	550.00	575.00	600.00
S1		-0.22	-0.42	0.02	0.66
S2		-0.27	-0.76	-1.00	-0.68
S3		-0.94	-0.50	0.05	0.31

Pressure rate [bar]		625.00	650.00	675.00	700.00
S1		0.93	0.63	0.11	-0.61
S2		0.02	0.56	0.73	0.45
S3		0.36	0.54	0.68	0.65

Pressure rate [bar]		725.00	750.00	775.00	800.00
S1		-0.88	-1.00	-0.93	-0.73
S2		0.03	0.01	0.33	0.62
S3		0.48	0.10	-0.16	-0.28



(a)



(b)

Figure-3.6: Polarization changes due to pressurization of the sample; (a) test set up, (b) Poincaré sphere rotation and (c) rotation projection on S1-S2 plane

Although the Poincaré sphere exhibits irregular rotation, it proves strong birefringence dependence on external pressure. It shall be kept in mind that these are straight-through kinds of measurements and the irregularity is believed to be a result of inhomogeneous sensitivity along the length (24m) of the cable sample. After this validation, we can expect that fully distributed measurements shall provide further insight, now broken into resolution segments of the cable.

2.6. *Compression of the stainless-steel tube in high-pressure condition*

It was of interest to evaluate the behavior of the SST when subjected to high hydrostatic pressure. With this objective in mind, it was necessary to build high pressure and a high temperature chamber for optical and mechanical measurements and characterization of optical fibers and FIMTs. The chamber is specially designed for distributed optical pressure and temperature measurements, see Fig.-3.7 showing construction details of the pressure chamber. The pressure consists of low pressure and high-pressure segments. Low pneumatic pressure is used to build hydraulic high-pressure. Silicon oils are used as pressurization liquids. Since its length exceeds 24 m, all relevant resolution lengths in distributed optical sensing are supported with the design. For example, pressure and temperatures can be used to check impact on both; attenuation and birefringence for most of FIMT tight buffer and specialty-optical fiber constructions. Furthermore, the pressure chamber is particularly useful for simulation of borehole conditions. For example, using this test chamber, the collapse pressure of the samples

can be determined as a measure of precision in the manufacturing process. From theoretical background we know that collapse pressure is inversely proportional to the ellipticity of the sample under the test and the ratio between the outer diameter and wall thickness.

Let us demonstrate the possibilities of the developed chamber as an example of measurements. The special benefit of the chamber are the tests for determination of compression magnitude, as well as its measurement repeatability in the pressure cycling. In this test the SST sample with no optical fibers is filled with water and brought through the pressure chamber and sealed on both ends (Fig.-3.8).

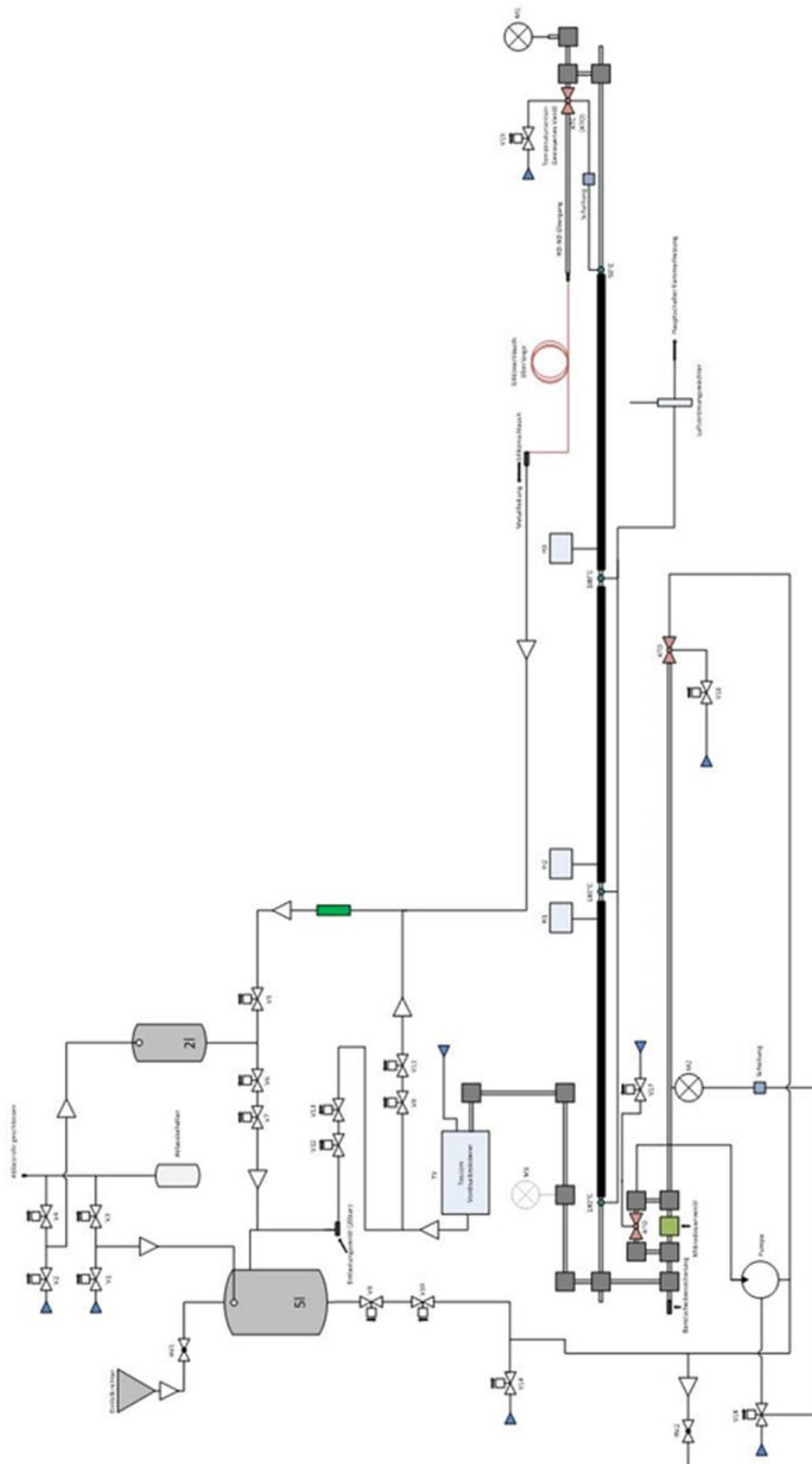
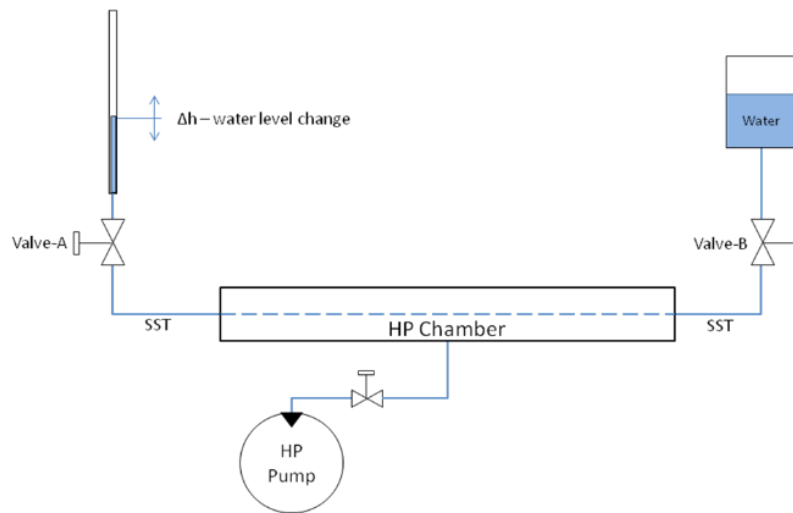
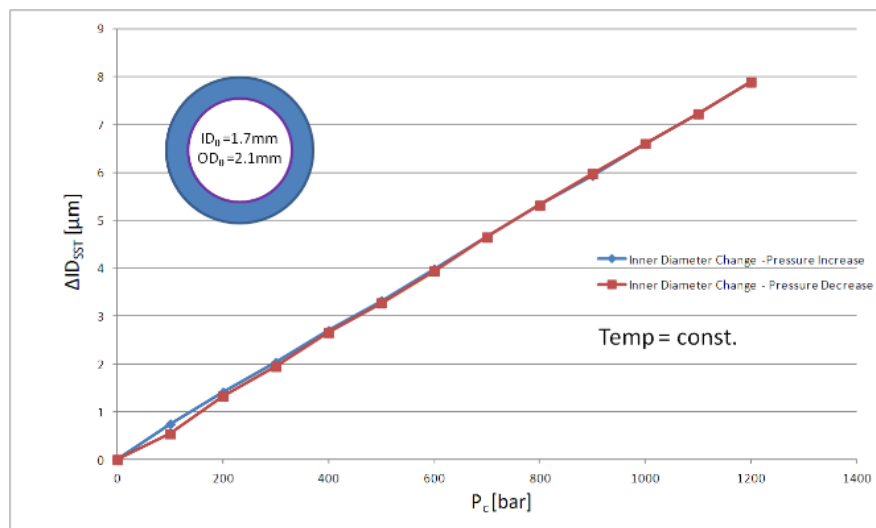


Figure-3.7: Simplified block scheme of the high-pressure chamber



(a)



(b)

Figure-3.8: Measurement of the change in tube outer and inner diameter under high pressure (a) evaluation set-up; (b) measurement results

The water tank is installed on the right end of the sample, whereas the water level indicator is placed to its left terminal. Both ends of the sample are led outside the pressure chamber and are thus freed from the pressure impact. The water is then led through the sample, all the way to the water indicator on the other side of the set-up. The tank valve is then closed, and the water reference level is indicated. Hence, during pressurization the water can only escape on the indicator side and the water level is increased following the change in cable diameter. The reduction in inner and outer diameter of the sample due to compression has been observed and

measured. Knowing the geometry of the sample SST, the effective length of the pressure chamber, and indicator dimensions, and observing the volume that is pushed out towards the indicator, we can now set the equation:

$$\left(\frac{ID_{IND}}{2}\right)^2 \pi \Delta h = \left(\frac{ID_{SST}}{2}\right)^2 \pi L_{CH} - \left(\frac{ID_{SST} - \Delta ID_{SST}}{2}\right)^2 \pi L_{CH} \quad (3.18)$$

The change in water level due to pressure increase shall be:

$$\Delta h = \frac{\Delta ID_{SST} (2ID_{SST} - \Delta ID_{SST})}{ID_{IND}^2} L_{CH} \quad (3.19)$$

From this equation ΔID_{SST} can be extracted:

$$\Delta ID_{SST} = ID_{SST} \left(1 - \sqrt{1 - \frac{\Delta h}{L_{CH}} \left(\frac{ID_{IND}}{ID_{SST}}\right)^2} \right) \quad (3.20)$$

Where;

- Δh is the water level change due to pressure change in the indicator
- ΔID_{SST} is the change in the inner diameter of the steel tube
- ID_{SST} is the initial inner diameter of the steel tube
- ID_{IND} is the inner diameter of the water level indicator
- L_{ch} is the effective pressure chamber length

The obtained results (Fig.-3.8b) are obtained for the 316L SST and they show linear characteristics in both cycles; pressurization (blue line) and depressurization (red line). Hence, it qualifies stainless steel tubes for the purpose of distributed pressure measurements within the pressure range from 0 to 1200 bar. In other measurements it was observed that different steels provide different characteristics and more cycling brings more linearity. SST qualifies for the purpose of pressure transducer, scaling the pressure to the range that assures long term integrity and lifetime of the optical fiber – which is of strategic importance in the applications. All this yields to a range of possibilities for further optimization techniques that shall be discussed later on.

3. FULLY DISTRIBUTED PRESSURE INTERROGATION METHODS USING STIMULATED BRILLOUIN SCATTERING

So far it has been demonstrated that all three fibers are asymmetrically loaded and therefore intrinsically birefringent due to the encapsulation process during the manufacturing of the cable. Optical fibers inside the encapsulation tube must be compressed to some extent. Therefore, they are intrinsically birefringent. The increase of pressure on the circumference in the pressurization cycle causes increase of fiber birefringence, too. With stimulated Brillouin scattering techniques (SBS) we need two lightwaves to cause their interaction in the optical medium. Therefore, birefringence increase will have impact on both waves, and we need appropriate mathematical models describing birefringence increase and polarization effects in the fiber for both waves. A model, particularly suitable for this task, was found and described in [10].

For the pump wave we can introduce the following model:

$$e_p = E_{p0}(t, z) \begin{cases} \cos(\alpha_p) \cos[\omega_p t + \varphi_p(t, z) - k_{p,x}z + \delta_p] \\ \sin(\alpha_p) \cos[\omega_p t + \varphi_p(t, z) - k_{p,y}z - \delta_p] \end{cases} \quad (4.1)$$

$$e_p = \tilde{E}_p(t, z) \begin{cases} \cos(\alpha_p) e^{-jk_{p,x}z + j\delta_p} \\ \sin(\alpha_p) e^{-jk_{p,y}z - j\delta_p} \end{cases} \quad (4.2)$$

The same for the Stokes waves:

$$e_s = E_{s0}(t, z) \begin{cases} \cos(\alpha_s) \cos[\omega_s t + \varphi_s(t, z) - k_{s,x}(L - z) + \delta_s] \\ \sin(\alpha_s) \cos[\omega_s t + \varphi_s(t, z) - k_{s,y}(L - z) - \delta_s] \end{cases} \quad (4.3)$$

$$e_s = \tilde{E}_s(t, z) \begin{cases} \cos(\alpha_s) e^{jk_{s,x}(z-L) + j\delta_s} \\ \sin(\alpha_s) e^{jk_{s,y}(z-L) - j\delta_s} \end{cases} \quad (4.4)$$

Where:

- $\tilde{E}_p(t, z) = E_{p0}(t, z)e^{j\varphi_p(t, z)}$ and $\tilde{E}_s(t, z) = E_{s0}(t, z)e^{j\varphi_s(t, z)}$ are phasors for the pump and Stokes waves, respectively.
- α_s and α_p – initial polarization angles of the Stokes and pump field strength vectors with respect to slow and fast axis of propagation in xy -plane

- δ_S and δ_P – initial phase difference (retardation) of Stokes and pump waves launched at both ends of the fiber closed in the loop.
- φ_S and φ_P represent phase shifts due to the source and perturbations in the optical medium. It can be neglected in these considerations.

Now, the birefringence $\Delta n = n_x - n_y$ induced will cause difference in propagation constants in x - and y - axis for both waves. This difference is:

$$\Delta k_p = k_{p,x} - k_{p,y} = \frac{2\pi f_p}{c} (n_x - n_y) \quad (4.5a)$$

$$\Delta k_s = k_{s,x} - k_{s,y} = \frac{2\pi f_s}{c} (n_x - n_y) \quad (4.5b)$$

Since one axis will be compressed while the other decompressed, we can now introduce average and initial equilibrium propagation constants $k_{p,0}$ and $k_{s,0}$ as:

$$k_{p,x} = k_{p,0} + \frac{1}{2} \Delta k_p \quad (4.6a)$$

$$k_{p,y} = k_{p,0} - \frac{1}{2} \Delta k_p \quad (4.6b)$$

$$k_{s,x} = k_{s,0} + \frac{1}{2} \Delta k_s \quad (4.6c)$$

$$k_{s,y} = k_{s,0} - \frac{1}{2} \Delta k_s \quad (4.6d)$$

We substitute (4.6) in (4.2) and (4.4) and get:

$$e_p = \tilde{E}_p(t, z) e^{-jk_{p,0}z} \begin{cases} \cos(\alpha_p) e^{-j0.5\Delta k_p z + j\delta_p} \\ \sin(\alpha_p) e^{+j0.5\Delta k_p z - j\delta_p} \end{cases} \quad (4.7a)$$

$$e_s = \tilde{E}_s(t, z) e^{jk_{s,0}(z-L)} \begin{cases} \cos(\alpha_s) e^{j0.5\Delta k_s z(z-L) + j\delta_s} \\ \sin(\alpha_s) e^{-j0.5\Delta k_s z(z-L) - j\delta_s} \end{cases} \quad (4.7b)$$

In this form both waves are suitable for polarization and phase considerations related to birefringence and pressure sensitivity. The following considerations matter now:

- $k_{s,0}$ and $k_{p,0}$ are the propagation constants of Stokes and pump waves at the entrance of the pressure sensitive cable segment. Their dependence of the wavelength on the small bandwidth is minor and can be neglected. Hence, from this point further we can take $k_{s,0} = k_{p,0} = k$ and $\Delta k_s = \Delta k_p = \Delta k$
- α_s and α_p are input angles of Stokes and pump waves in xy -plane that is geometrically perpendicular to the propagation direction in z -axis. They are both dependent on wavelength (but can be set confined to a particular polarization state by means of a passive polarizer).
- Δk_s and Δk_p are propagations constant differences (between linearly polarized waves with E-fields confined with the fast and slow axes) reflecting the magnitude of birefringence and therefore directly pressure dependent. The increase in Δk due to pressure increase will increase frequency and lower the beat-length of both waves within the fiber. The beat-length is the distance required for polarization states to repeat. In that respect, pressure can be measured simply by means of spatial beat-length measurements.
- δ_s and δ_p are the phase difference between the axes (Fig.-4.1) determining whether the input state of polarization will be linear, circular or elliptical [8]. If input retardance is 0, the wave is linearly polarized and if $\pi/4$ the wave is circularly polarized. All other values will cause elliptical polarization of the wave at input.

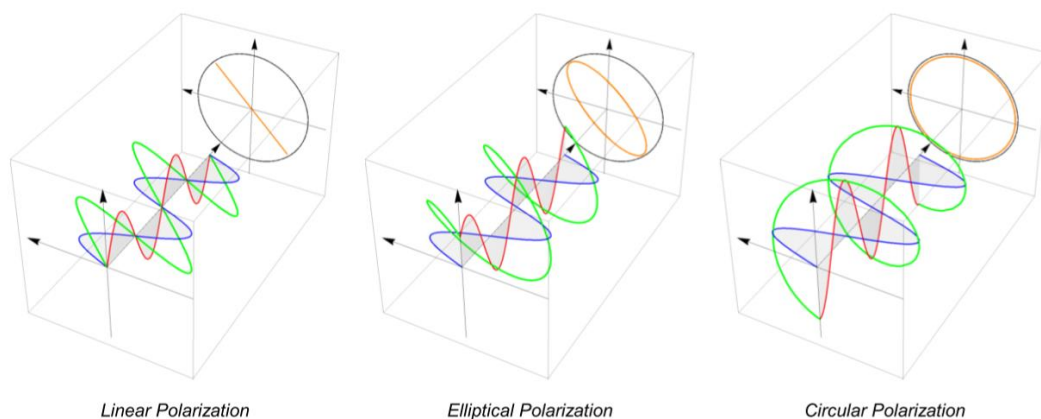


Figure 4.1: Polarization states in optical fibers [8]; linear polarization (a) with no retardance $\delta_x - \delta_y = 0$ between the x- and y- axis, any retardance $\delta = \delta_x - \delta_y$ will cause elliptical polarization, and the case $\delta =$

$$\delta_x - \delta_y = \frac{\pi}{2} \text{ giving circular polarization}$$

Further, we should also consider the refractive index difference in x - and y - axis giving rise to birefringence, hence constituting the basic mechanism for pressure change detection and measurement using the proposed cable concept. In weakly guiding fibers such as standard telecom fibers we have:

$$\Delta = \frac{n_c - n}{n} \leq 0.01 \quad (4.8)$$

For example, if we take $n = 1.48$ and apply it to (4.8) we get $\Delta n = 0.0148$ that is slightly different and used to design weakly guiding optical fibers. Now we will make an extraction of Δn that can be measured by modern optical measurement equipment. For Δk_s and Δk_p in (4.5) we have:

$$\Delta k_i = \frac{2\pi \times 193.54 \times 1E(+12)}{3 \times 1E(+8)} \times \Delta n \quad (4.9)$$

$$\Delta k_i = 4.053E(+6) \times \Delta n \quad (4.10)$$

where $i = S, P$; S for Stokes and P for pump wave. $\frac{\Delta k_i}{k}$ can be expressed using frequency spectra:

$$\frac{\Delta k_i}{k} = \frac{\Delta f_i}{f} = 4.0531E(+6) \times \frac{\Delta n}{n}. \quad (4.11)$$

So, if we take frequency $f = 193.54 \text{ THz}$ and the frequency resolution $\Delta f_i = 0.1 \text{ MHz}$ of a typical unit or measurement set-up, such as the one based on a stable heterodyne interferometer with two phase locked lasers or the Brillouin Optical Time Domain Analyzer (BOTDA), we can calculate Δn :

$$\Delta n = \frac{1}{4.0531E(+6)} \times \frac{\Delta f_i}{f} \times n \quad (4.12)$$

$$\Delta n = \frac{1}{4.053E(+6)} \times \frac{1E(+6)}{193.54E(+12)} \times 1.48 \quad (4.13)$$

$$\Delta n = 1.8866E(-15) \quad (4.14)$$

If we choose $\Delta f_i = 0.001 \text{ MHz}$ - that is easily provided with modern interferometer set-up - then we get $\Delta n = 1.8866E(-18)$. We see that an extremely small differences in refractive indices can be detected and measured with measurement devices presently available at the market. In terms of wavelength, we can perform similar calculations:

$$\Delta k_i = \frac{dk_i(\lambda_i)}{d\lambda} \Delta\lambda_i \quad (4.15)$$

$$k_i(\lambda_i) = \frac{2\pi}{\lambda_i}. \quad (4.16)$$

From (4.15) and (4.16) follows:

$$\Delta k_i = -2\pi \frac{1}{\lambda_i^2} \Delta\lambda_i \quad (4.17)$$

$$\Delta\lambda_i = -\frac{\lambda_i^2}{2\pi} \Delta k_i \quad (4.18)$$

The conversion from wavelength to frequency range will be important in considering frequency scanning of the Stokes signal. Table-4.2 quantitatively provides the conversion of wavelength change to frequency and propagation change. Note that Brillouin interaction at 1550nm and Brillouin-Lorentzian profiles do not exceed 100MHz of frequency ranges which correspondents to $\sim 0.8 \text{ pm}$ and $\sim 2.1 \text{ rad/m}$ of wavelength and propagation constant change, respectively. In the same way, the finest scanning resolution available from BOTDA unit used is 0.1 MHz corresponding to $\sim 0.8 \text{ fm}$ and $\sim 2.1 \text{ mrad/m}$ of wavelength and propagation constant change, respectively. The blue numbers denote common FWHM parameters of the Brillouin-Lorentzian profile measured on standard telecommunication fibers.

TABLE-4.2: CONVERSION OF WAVELENGTH CHANGE TO FREQUENCY
AND PROPAGATION CONSTANT RANGE

Speed of light $c[m/s]$: $3.000000E+08$
Wavelength range $\lambda_0[m]$: $1.550000E-06$
Refractive Index $n[-]$: 1.000000 (free space)

$\Delta\lambda$ -wavelength width [pm]	$\Delta\nu$ - frequency width [GHz]	Δk - propagation constant [rad/m]
1000.0000	124.869927	-2.6139E+03
100.0000	12.486993	-2.6139E+02
10.0000	1.248699	-2.6139E+01
1.0000	0.124870	-2.6139E+00
0.1000	0.012487	-2.6139E-01
0.6400	0.079917	-1.6729E+00
0.4000	0.049948	-1.0456E+00
0.0100	0.001249	-2.6139E-02
0.0010	0.000125	-2.6139E-03
0.0001	0.000012	-2.6139E-04

Substituting (4.10) into (4.18) we have:

$$\Delta\lambda_i = -4.0531E(+6) \times \frac{\lambda^2}{2\pi} \times \Delta n \quad (4.19)$$

If we take measurement set-up based on spectrum analysis using the standard optical spectrum analyzer (OSA) having wavelength resolution of $\Delta\lambda_i = 0.3nm$ (commonly found on the market) we can calculate Δn :

$$\Delta n = -\frac{2\pi}{4.0531E(+6)} \frac{\Delta\lambda_i}{\lambda^2} \quad (4.20)$$

$$\Delta n = 193.58E(-6) \quad (4.21)$$

If, for spectral resolution, we take $\Delta\lambda_i = 1 pm$, commonly available from modern tunable lasers, we obtain $\Delta n = 64.52E(-6)$. Therefore, when comparing (4.21) and (4.14) we can notice a large difference from which we can draw a few conclusions:

- Interferometric techniques e.g. phase-OTDRs, and Brillouin frequency scanning techniques, e.g. BOTDA are suitable candidates for pressure measurement systems. They offer more sensitivity with respect to Δn for both Stokes and the pump wave. This counts especially for the cases where robust cables are required providing more protection to optical fibers. In such case, the dynamic range Δn is smaller and it is sacrificed on account of the robustness of the cable
- SBS techniques can be considered as a special case of heterodyne interferometer with two counter-propagating lightwaves. In such form, a change pressure detection and measurement is suitable. Brillouin interaction can be regarded as an amplified interference of two lightwaves in the optical medium, and the peak of the spectral Brillouin-Lorentzian profile represents a maximum of this interference. Fiber loop represents one or a series of passive interferometers.
- Brillouin-Lorentzian profile of SBS interference shall be considered as a range of fine optical spectrum analysis (OSA) suitable for wavelength scanning by means of Stokes wave.
- Both distributed interferometric and Brillouin techniques can intrinsically profile Δk , Δn and the environmental pressure p in which the cable is immersed.
- Since distributed interferometric and distributed Brillouin techniques qualify for distributed pressure profiling, additional work is needed in the analysis of their performance and characteristics, and the comparison between the two.

Because of strong interaction, the considerations above lead to the conclusion that the fiber optic cable aimed for pressure measurements can be interrogated with the stimulated Brillouin scattering measurement technique [10] with best available precision to our knowledge.

Maximal SBS interaction and interrogation of optical fibers involves two counter-propagating lightwaves. This is arranged with optical fiber in the loop configuration as described in Fig.-4.2. There are two ports from which the lights are launched: pump and Stokes port. The cable sample is inserted within the first half closer to the pump port. It is also efficient since the pump in that segment is non-depleted and thus more pump power is invested into the inelastic Brillouin interaction and generation of acoustic wave causing a backscattered signal at Stokes wavelength.

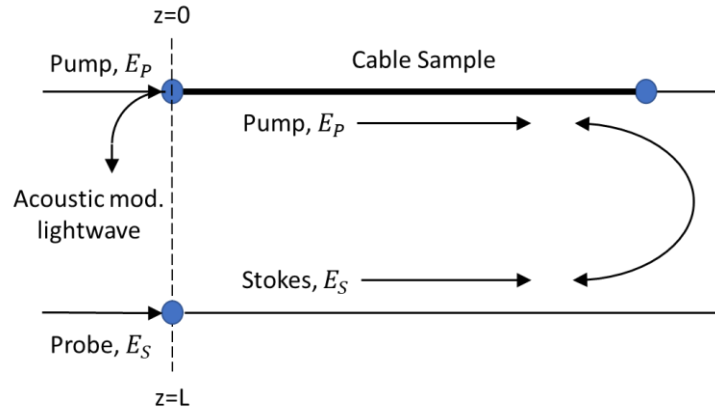


Figure-4.2: Stimulated Brillouin measurement set-up requires interaction of two waves counter-propagating within the fibers; the pump delivers energy and spatial profiling and the Stokes wave – also referred to as ‘the probe’ - scans the frequency ranges where Brillouin interaction takes place.

As shown in Chapter-2, the intensity of pumped and Stokes optical signals (I_P and I_S) can be described with the following differential equations:

$$\left[\frac{n}{c} \frac{\partial}{\partial t} - \frac{\partial}{\partial z} + \alpha \right] I_P = -g_B I_S I_P \quad (4.22a)$$

$$\left[\frac{n}{c} \frac{\partial}{\partial t} - \frac{\partial}{\partial z} + \alpha \right] I_S = -g_B I_S I_P \quad (4.22b)$$

Where:

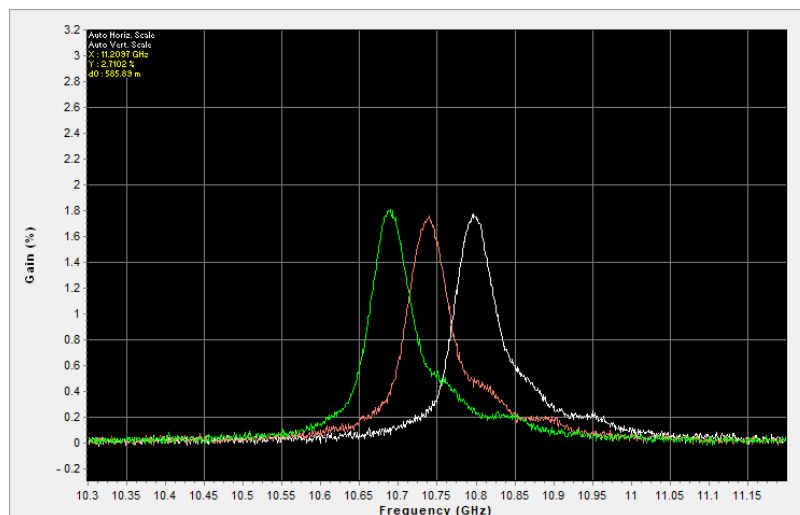
- $I_p = \frac{n\varepsilon_0 c}{2} |\tilde{E}_p|^2$ - pump intensity
- $I_s = \frac{n\varepsilon_0 c}{2} |\tilde{E}_s|^2$ - Stokes (scanning) light intensity
- ξ - polarization efficiency
- g_B - gain of Brillouin signal
- α - characteristic attenuation

The polarization-dependent amplification factor ξ reflects polarization and birefringence effects. The propagation constant difference Δk bears the information on birefringence between the axes:

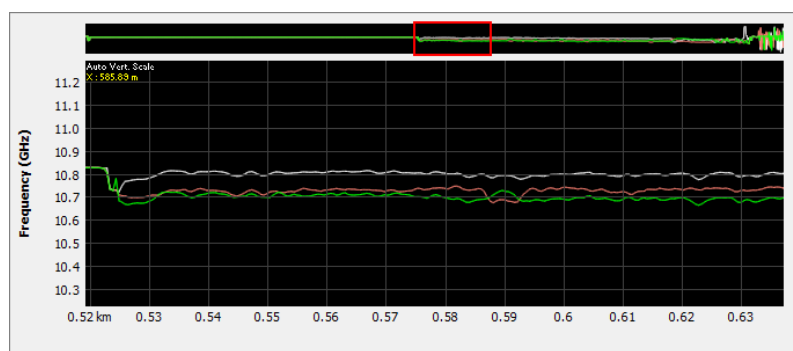
$$\xi = \frac{1}{2} [\cos^2(\alpha_S - \alpha_P) - \cos^2(\alpha_S + \alpha_P)] [1 + \cos[2\Delta kz - \Delta kL + 2(\delta_S - \delta_P)]] + \cos^2(\alpha_S + \alpha_P) \quad (4.23)$$

The Brillouin gain is described with (2.73) and (2.74),

A typical analysis of the SBS backscatter involves profiling of a Brillouin-Lorentzian shape, known as “the bell”. It is obtained from each sampled segment along the length of the cable. From the profile, we can determine two important parameters - the frequency position of the peak and its shifts across the length of the cable and full-width-at-half-maximum (FWHM), the results of which are shown in Fig.-4.3a and Fig.-4.3b, respectively. DiTest BOTDA unit from Omnisens is used for these measurements. The Brillouin-Lorentzian profile is an appropriate tool that reveals information on the quality of the cable and its production process.



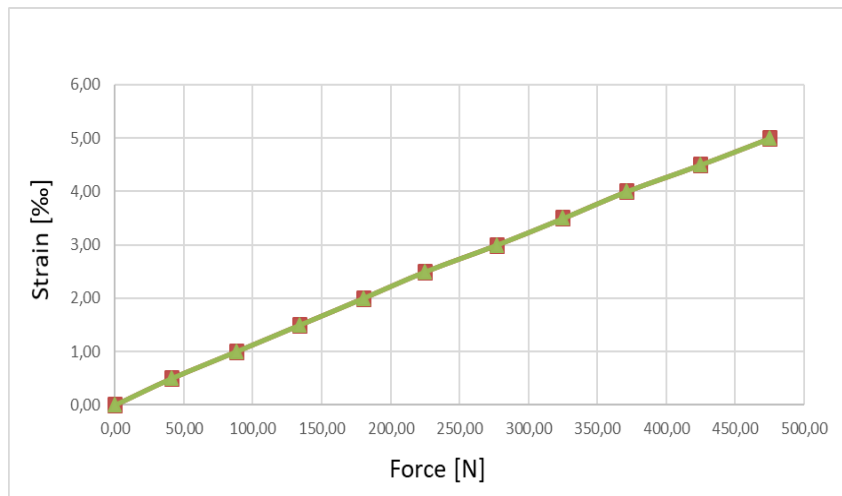
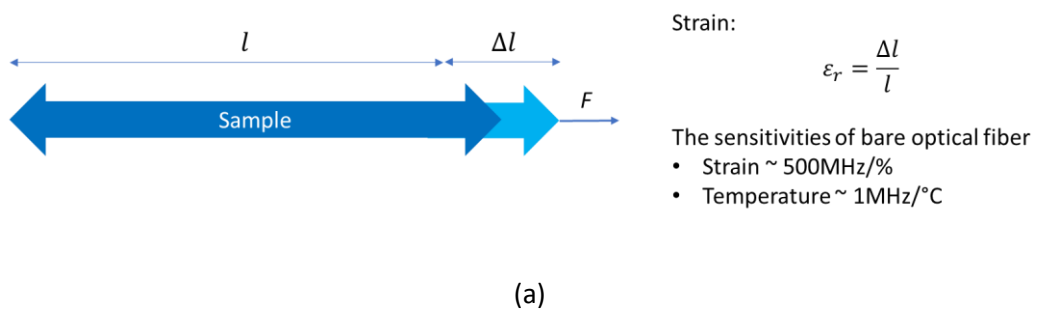
(a)



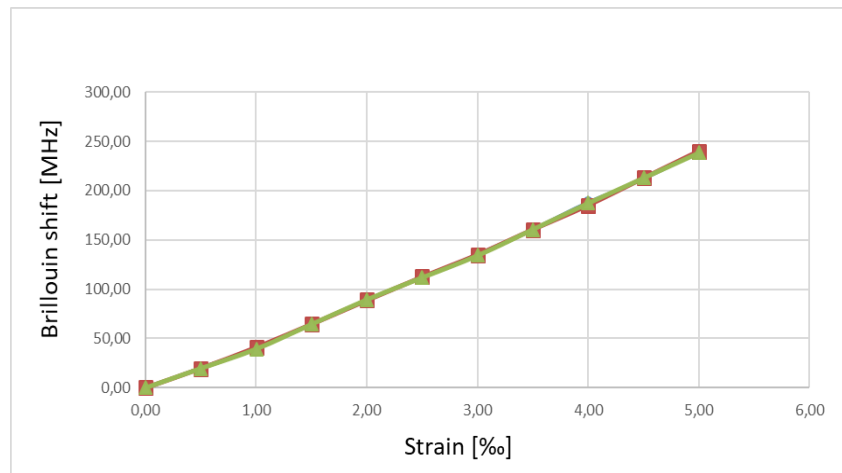
(b)

Figure-4.3: Measurement results obtained from all three fibers from the prototype; (a) spatial Brillouin profile of the monitored cable segment, (b) frequency (Lorentzian) profile of Brillouin backscattered signal

Since optical fibers are in tight contact with the steel tube, all the strain exerted on the steel encapsulation will, in an ideal case, be transferred to optical fibers with the same magnitude. This can be measured using both BOTDR and BOTDA techniques in which the central peak of the Brillouin-Lorentzian profile is proportional to the strain applied to the fiber. The measurement results (Fig.-4.4) confirm strong coupling and full strain transfer to the optical fibers of the strain exerted on the tube. All three fibers react in the same way and the characteristics obtained are linear.



(b)



(c)

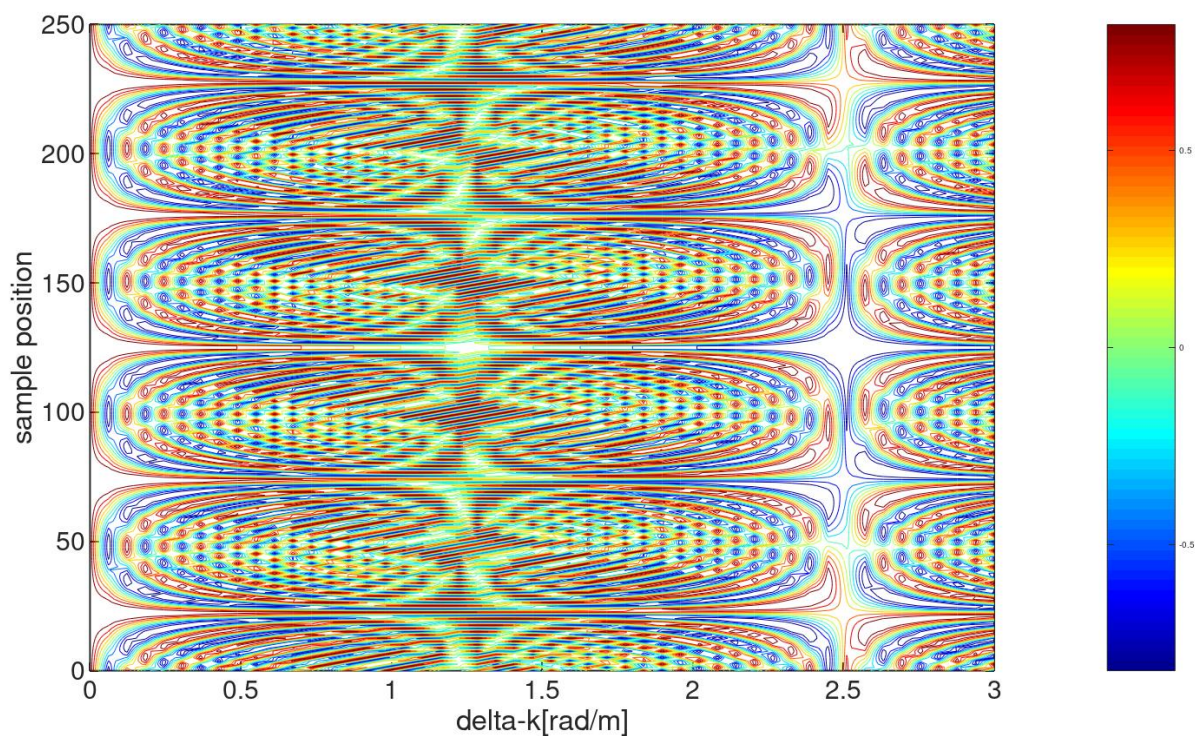
Figure-4.4: One-way stress-strain (SS) measurements of cable prototype characteristics; (a) measurement set-up, (b) strain characteristics for all three fibers (one on top of the other two) exhibiting highly linear behavior, and (c) Brillouin strain characteristics

As a function of the both; the strain ε and temperature T of the Brillouin-Lorentzian profile will move left or right in the spectral or Δkz -plane. The strain and temperature of optical fiber does not impact the shape of the Brillouin-Lorentzian profile, and it will remain unchanged only shifted. On the other hand, the change of temperature will introduce phase shifts in polarization efficiency ξ . Presuming that the temperature change impact both waves and both axes of the fiber equally, it means that the form of the blueprint in Δkz -plane will not change since the blueprint is dependent on product Δkz and the phase difference of both waves (4.23) only. On one hand, due to the cable design, pressure change will change Δk dramatically and that will, in turn, change the blueprint of ξ in Δkz -plane. The change of ξ depicted in Δkz -plane will also cause change in the Brillouin-Lorentzian profile (2.73).

3.1. The Brillouin-Lorentzian profile and the investigation of polarization efficiency ξ application in distributed pressure measurements

Polarization efficiency ξ represents a factor that multiplies the Brillouin-Lorentzian profile (2.73) and defines the strength of the interaction of the two counter-propagating waves. On one hand it impacts the altitude of the Brillouin-Lorentzian peak in the profile, and on the other it

connects the spatial (z) to the spectral domain (Δk) that is related to the wavelength range $\Delta\lambda$ with (4.15) and (4.18). When no birefringence is involved between the axes then $\Delta k = 0$ and polarization efficiency ξ is a smooth function that does not change with the length - given that polarization parameters of the wave are constant. In case $\Delta k \neq 0$, the periodic function $\cos[2\Delta kz - \Delta kL + 2(\delta_S - \delta_P)]$ from (4.23) will be nonzero and it will give rise to ripples in ξ . In other words, the blueprint of ξ in Δkz -plane changes. These ripples are a function of birefringence, the position z , and phase difference $\delta_S - \delta_P$. As an example, we provide several illustrations (Fig.-4.5) of the function $y = \cos[\Delta k(2z - L) + 2(\delta_S - \delta_P)]$ in Δkz -plane for $\Delta k = 0 \div 3$ and 250 sample position points presuming $\delta_S - \delta_P = 0$.



(a)

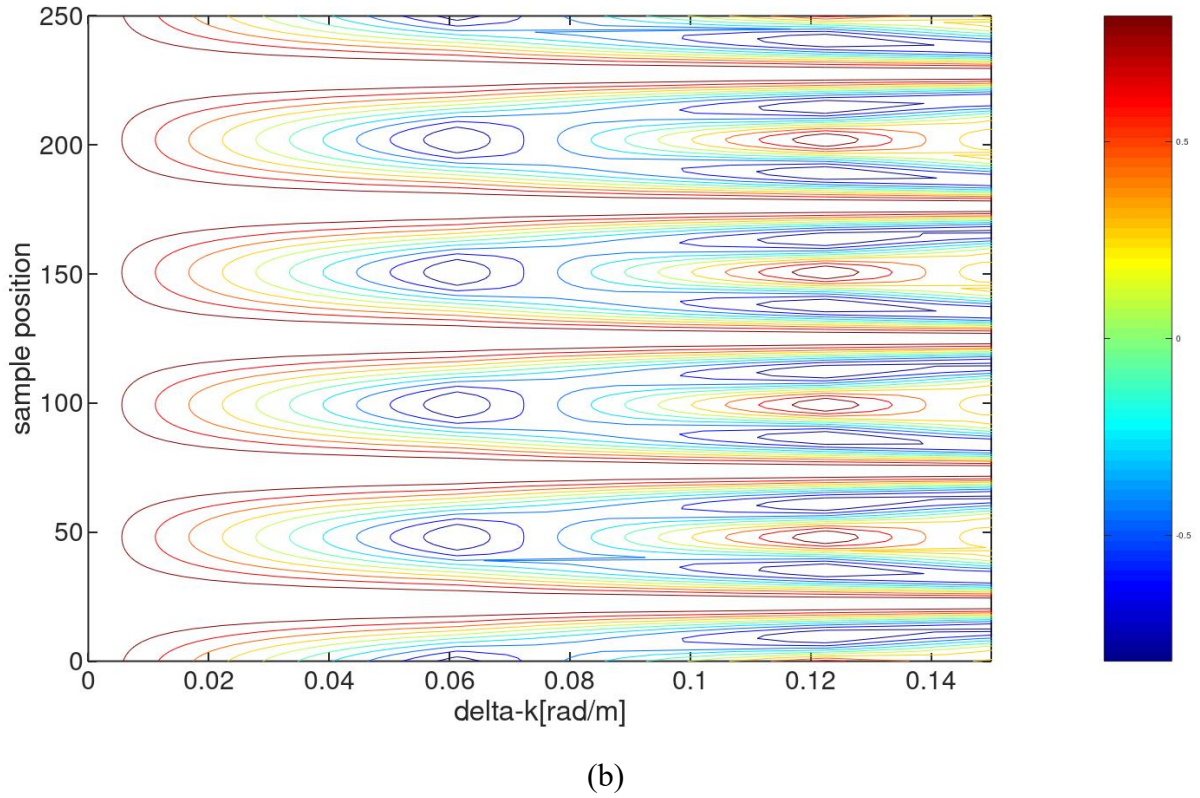


Figure-4.5: Contour blueprint of $\cos[\Delta k(2z - L) + 2(\delta_S - \delta_P)]$ in Δkz -plane for $z = 0 \div 250$ samples and $\delta_S - \delta_P = 0$; (a) periodicity in Δkz -plane in both axes, and (b) the zoomed version showing no periodicity for $\Delta k = 0$ and evolution of first extremes as Δk increases.

Hence, the product Δkz defines the blueprint of ξ in Δkz -plane. The phase difference $\delta_S - \delta_P$ will only shift the same configuration across Δkz -plane. We know from earlier that Δk is directly dependent on birefringence Δn , and, due to the construction of the cable, also on hydrostatic pressure. It means that pressure measurements can be deduced from the measurement of Δk . The difference in propagation constant Δk is the subject of our optical measurements, e.g. with BOTDA. The measurement techniques that lead to Δk read-out need to be developed first. There are several possible approaches to that. Since Δk can be measured in both domains, there can be at least 2 known measurements - one in the spectral domain and one in the spatial domain. A convenient way to that objective would be without requiring intervention into interrogation equipment, i.e. to avoid additional cost and investments. We need to investigate whether this can be realized simply with manipulation of both lightwaves at their launch sides, as depicted in Fig-4.6. At both terminals of the fiber loop, sets of polarization

controllers and variable retarders are inserted which enables passive manipulation of light. This new set-up will help us investigate the properties of lights and their interaction defined in (4.23)

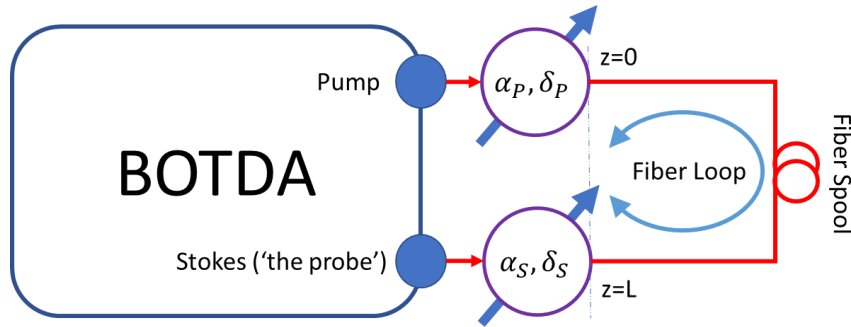


Figure-4.6: Interrogation method suggested for distributed Δk measurements. The lightwaves are manipulated in polarization and phase at both ends before launched in the fiber

Our interest is to investigate the impact of Δk on polarization efficiency ξ , and in which way we can use ξ to conclude and calculate the difference in the propagation constant Δk . Since Δk is a function of pressure p change, $\Delta k = \Delta k(p)$, and because our BOTDA equipment characterizes the optical fiber in a fully distributed way, we shall be able to profile the pressure change fully as well as distributively. In other words, we need to investigate properties and characteristics of ξ in more details and in particular for the following conditions:

- ξ vanishes ($\xi = 0$);
- ξ has extremes in spectral domain Δk
- ξ has extremes in spatial domain z

Case ξ vanishes ($\xi = 0$)

From (4.23) we see that ξ will vanish under the following condition:

a)
$$\Delta k(2z - L) + 2(\delta_s - \delta_p) = 0 \tag{4.24}$$

b)
$$\alpha_s - \alpha_p = \frac{\pi}{2} \tag{4.25}$$

Applying condition (4.26a) to ξ we get:

Now adding condition (4.26b) we get $\xi = 0$. Hence, for stimulated Brillouin interaction to vanish it takes:

1. Orthogonality of field strength vectors with respect to *fast* and *slow* axes, and
2. One of the two
 - Both $\Delta k = 0$ and $\delta_S - \delta_P = 0$ or
 - $\Delta k = -2 \frac{\delta_S - \delta_P}{2z - L}$

This condition (4.25a) reflects the fact that the stimulated Brillouin effect is built only with those components of the waves that are parallel, and not by those that are perpendicular (Fig.-4.7). It sets in the relation Δk , position on the fiber z , and launching retardancies δ_S and δ_P required for $\xi = 0$. If Δk is constant (vertical line in Δkz -plane) and distance z grows, then positions having $\xi = 0$ detected in the measurements can reveal phase differences $\delta_S - \delta_P$.

In a different case in which we will have $\alpha_S - \alpha_P = 0$ (but not $\alpha_S = \alpha_P = 0!$), the polarization efficiency ξ will be nonzero, all that regardless of the position z , propagation constant difference Δk or the input retardance difference $\delta_S - \delta_P$.

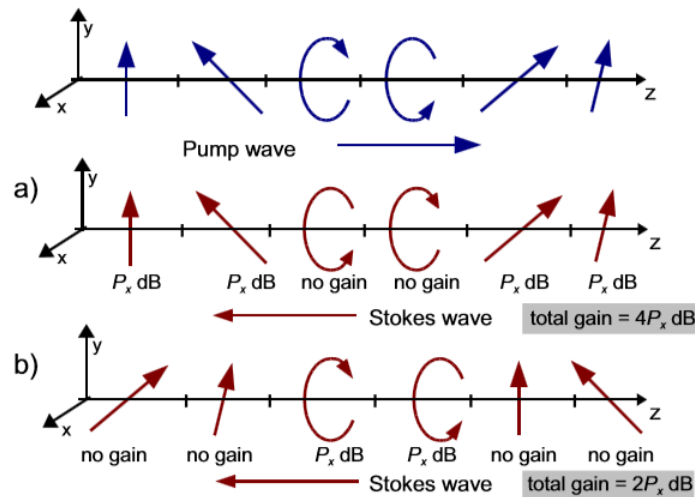


Figure-4.7: Polarization efficiency as a function of Pump and Stokes wave polarization [15]

With Δk nonzero, there is a number of spots in which interaction of the Stokes and pump wave has an extreme. They shall be observed in Brillouin gain measurements and recognized as ripples with valleys and peaks in the signal, all in accordance with (4.23).

3.2. Extraction method 1: finding extremes of ξ in the spectral domain

The Stimulated Brillouin Scattering technique uses two lightwaves; the pump delivering energy for the interaction process, and Stokes bringing frequency/wavelength scanning into the system. The scanning features of the system can be regarded as a specialty non-linear optical spectrum analysis (OSA) system based on tunable laser technique. As such, it brings one additional benefit. The polarization efficiency ξ is dependent only on polarization parameters and at input on Δkz product and on retardance $\delta_S - \delta_P$. Nonzero Δk causes ripples in the whole Δkz -plane, for all Δk and z positions. But in the measurements not all the ripples in the Δkz -plane will be observed - only the segment of a few 10ths of MHz in Δkz -plane where stimulated Brillouin interaction takes place will be observed with BOTDA. We have mentioned earlier that the position of the Brillouin-Lorentzian profile in the spectral domain depends on strain and temperature. This is not the case for polarization efficiency ξ – its blueprint in the Δkz -plane remains unaffected by the changes in strain and temperature – the changes that the fiber is subjected to. It means that the ripples in Δkz -plane are dependent on pressure change and not on temperature and strain change, and they can be used for measurements of Δk and hence the pressure change p .

Therefore, the measurement of birefringence is reduced to the measurements of ripples in the spectral domain. In that sense we need to investigate extremes in the spectral domain. The spectral domain is interrogated with the Stokes wave only - the pump can be left unchanged and shall be beneficial as such (Fig.-4.8). For this purpose, we need a slight adaptation of (4.23). It shall now reflect the fact that all polarization parameters of the Stokes wave are wavelength dependent.

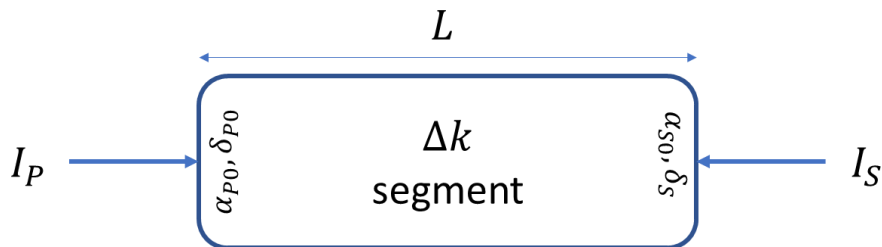


Figure-4.8: The segment to be interrogated for determination of Δk . Polarization properties of light in the segments along the fiber are random and cannot be predicted.

Using trigonometric identities $2\cos^2\theta = 1 + \cos 2\theta$ the equation (4.23) can be rewritten in a form more suitable for manipulation:

$$\xi(\Delta k) = \frac{1}{2} [\cos 2(\alpha_{S0} - \alpha_{P0}) - \cos 2(\alpha_{S0} + \alpha_{P0})] \cos^2 \Theta + \cos^2(\alpha_{S0} + \alpha_{P0}) \quad (4.26)$$

where:

$$\Theta = \Delta k \left(z - \frac{L}{2} \right) + (\delta_S - \delta_{P0}). \quad (4.27)$$

We shall now investigate extremes of the function $\xi(\Delta k)$:

$$\frac{d}{d(\Delta k)} \xi(\Delta k) = 0 \quad (4.28)$$

$$\xi' = -[\cos 2(\alpha_{S0} - \alpha_{P0}) - \cos 2(\alpha_{S0} + \alpha_{P0})] \cos \Theta \sin \Theta \cdot \Theta' \quad (4.29)$$

Using identity $\sin(2\theta) = 2\sin\theta\cos\theta$:

$$\xi' = -\frac{1}{2} [\cos 2(\alpha_{S0} - \alpha_{P0}) - \cos 2(\alpha_{S0} + \alpha_{P0})] \sin 2\Theta \cdot \Theta' \quad (4.30)$$

From (4.27) we also have:

$$\Theta' = \left(z_0 - \frac{L}{2} \right) \quad (4.31)$$

Substituting (4.27) and (4.31) in (4.30) we get:

$$\xi' = -\frac{1}{2} \left(z_0 - \frac{L}{2} \right) [\cos 2(\alpha_{S0} - \alpha_{P0}) - \cos 2(\alpha_{S0} + \alpha_{P0})] \sin[\Delta k(2z_0 - L) + 2(\delta_S - \delta_{P0})] \quad (4.32)$$

$\xi(\Delta k)$ has extremes when the following condition is fulfilled:

$$\Delta k(2z_0 - L) + 2(\delta_{S0} - \delta_{P0}) = m\pi \quad (4.33)$$

Δk that fulfills the condition (4.33) can be calculated as:

$$\Delta k = \frac{m\pi - 2(\delta_S - \delta_{P0})}{(2z_0 - L)}. \quad (4.34)$$

From the equation (4.34) we can see that the position of extremes depends on the phase of the Stokes wave δ_S and we can make use of it. For example, we can take the measurement by means of a common BOTDA unit and external passive manipulation of δ_S , e.g. using a variable retarder at Stokes wave input (Fig.-4.9). By varying δ_S , shifts in Δkz -plane will be introduced.

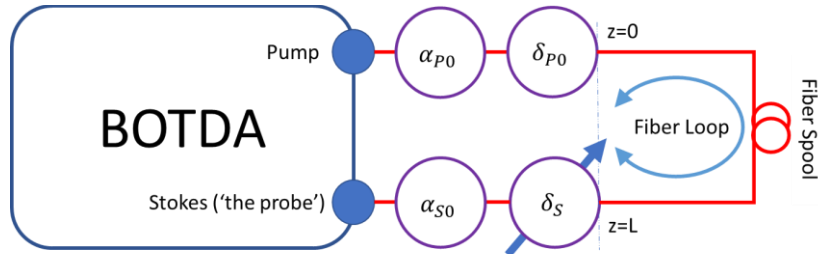
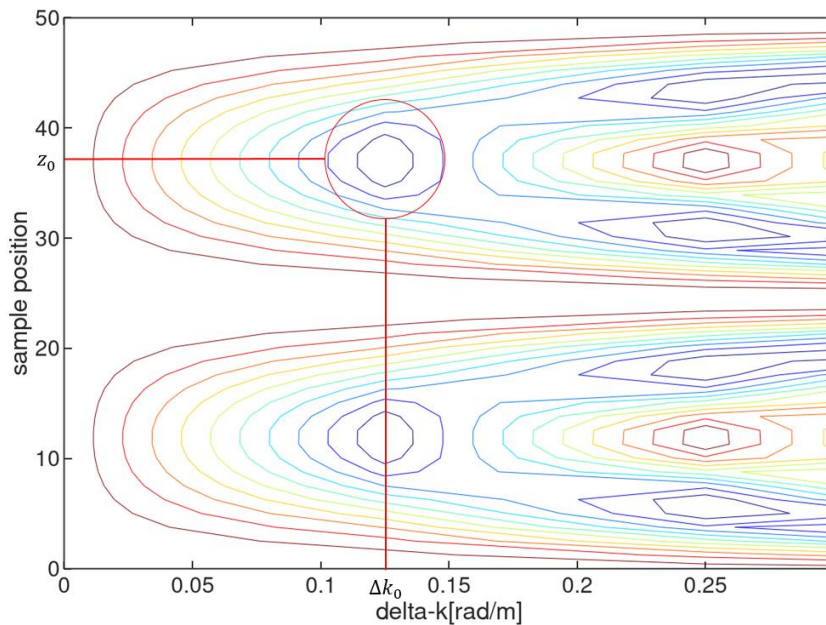
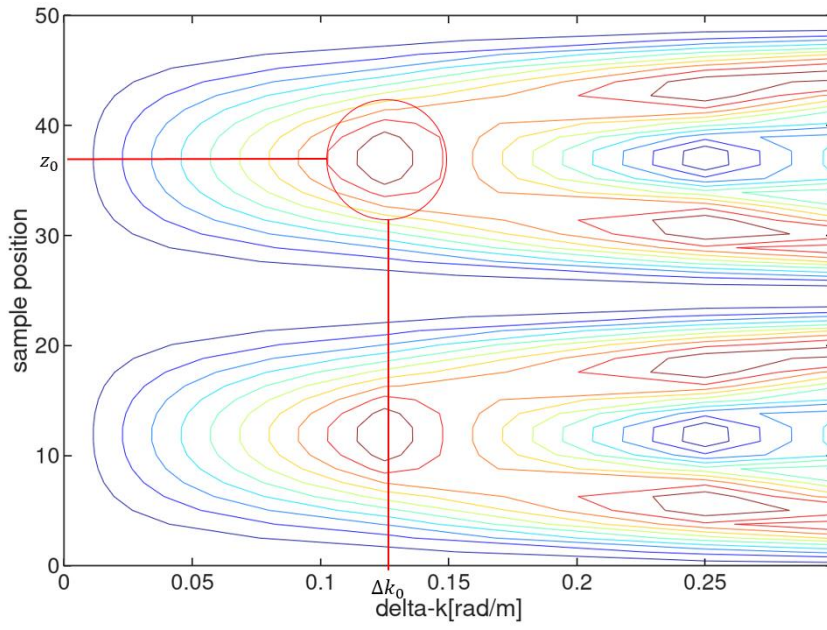


Figure-4.9: Measurement set up for Δk profiling in spectral domain

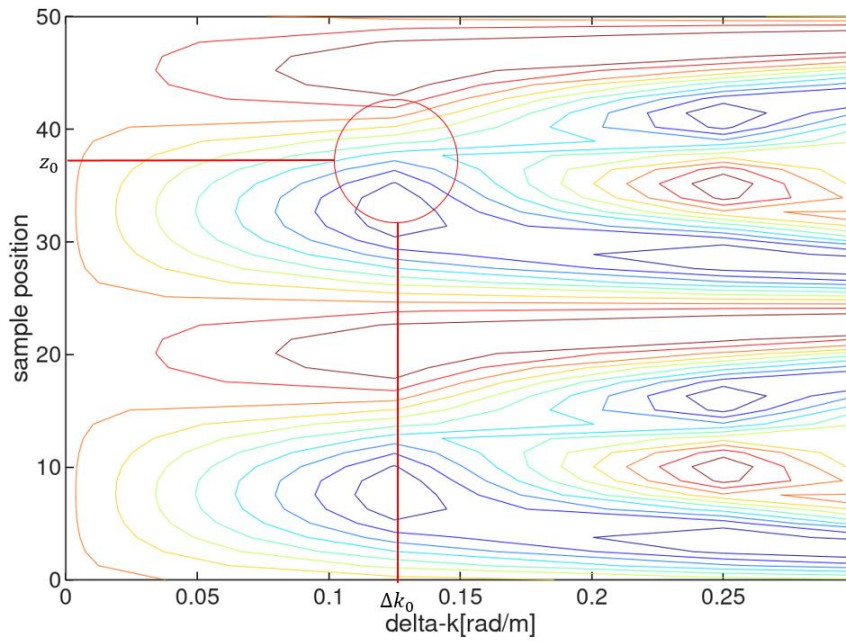
Fig.-4.10 shows shifts in Δkz -plane induced for $\delta_S - \delta_P = 0, \pi/3, 2\pi/3, \pi$. The procedure is the following – we set fixed input linear polarization parameters and continue scanning our Brillouin-Lorentzian profile within the available spectral range of the unit as usual. Now we additionally introduce and measure phase change that moves over the working point $\Delta k_0 z_0$ (where Δk_0 can be zero) in the Δkz -plane that we had set. The phase manipulation δ_S changes the magnitude of the Brillouin-Lorentzian gain that we measure with the BOTDA unit.



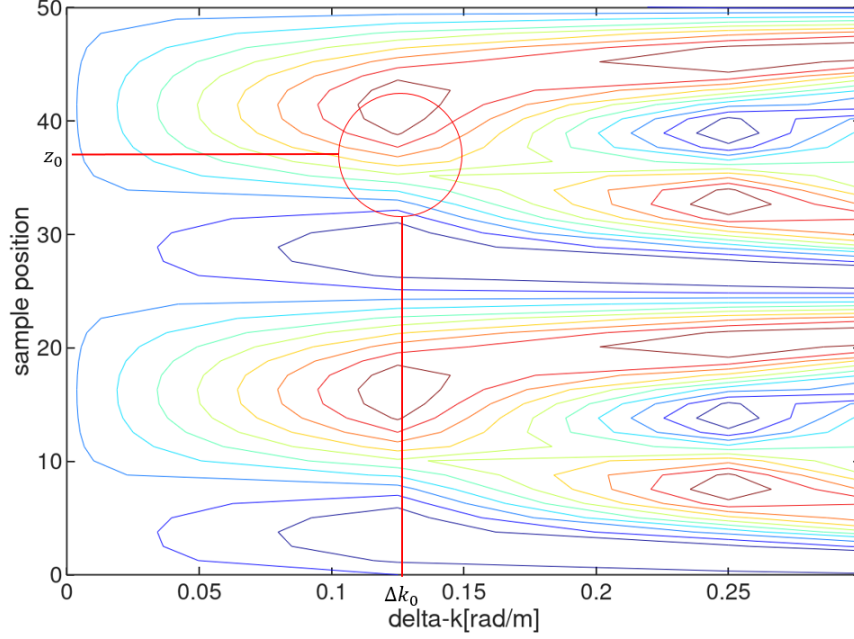
(a)



(b)



(c)



(d)

Figure-4.10: Contour representation of ξ in $\Delta k z$ -plane and impact of phase shift in Stokes wave δ_S for different values $\mathbf{0}$ (a), $\frac{\pi}{3}$ rad (b), $\frac{2\pi}{3}$ (c) and π (c). The phase δ_S shifts ξ in vertical direction

During the process we observe and note the strength of Brillouin gain at every phase position that we use for recovering the initial periodic function with phase change as its argument. Since manipulating the Stoke wave phase δ_S shifts ξ in the $\Delta k z$ -plane only vertically, we stay always for all shifts at the same Δk . The change of Δk , e.g. due to pressure change, moves us to the other position on Δk -axis where other phase dynamics exist. Therefore, manipulating only with retardance δ_S at the Stokes wave entrance, and monitoring ξ and its extremes, we can calculate Δk for the position z_0 . The distance between two adjacent minimums, say m and $m + 2$ with retardances δ_{S1} and δ_{S2} , can be calculated using (4.34):

$$(\Delta k_2 - \Delta k_1)(2z - L) = (m + 2)\pi - 2(\delta_{S2} - \delta_P) - m\pi - 2(\delta_{S1} - \delta_P)$$

$$(\Delta k_2 - \Delta k_1)(2z - L) = 2\pi - 2(\delta_{S2} - \delta_{S1})$$

$$(\Delta k_2 - \Delta k_1) = 2 \frac{\pi - \Delta\delta_{S2-S1}}{(2z_0 - L)} \quad (4.35)$$

$$\underbrace{\Delta k_2(p)}_{\text{calculated}} = 2 \frac{\pi - \overbrace{\Delta \delta_{S2-S1}}^{\substack{\text{the reading} \\ \text{from VR}}}}{(2z_0 - L)} + \underbrace{\Delta k_1(p=0)}_{\substack{\text{reference value} \\ \text{(calibration)}}} \quad (4.36)$$

The value of $\Delta \delta_{S1-S2}$ - required for the transition from one to the next minimum position of ξ , can be read from the variable retarder (VR). δ_{S1} is a reference value and can be set to $\delta_{S2} = 0$. In such case $\Delta \delta_{S2-S1} = \delta_{S2}$.

3.3. Extraction method 2: finding extremes of ξ in the spatial domain

Analogously, another method for determining Δk can be developed in the spatial domain. In an earlier case, we conducted derivatives on the Δk , whereas in this case we will do it with respect to the length. In the fiber observed we cannot have information on its polarization states and will rely on the spatial profile of ξ which we measure from the BOTDA unit. The condition for finding extremes that $\xi(z)$ undergoes along the length z is:

$$\frac{d}{dz} \xi(z) = 0 \quad (4.37)$$

$$\frac{d}{dz} \xi = \left\{ \frac{1}{2} [\cos 2(\alpha_{S0} - \alpha_{P0}) - \cos 2(\alpha_{S0} + \alpha_{P0})] \cos^2 \theta + \cos^2(\alpha_{S0} + \alpha_{P0}) \right\}' \quad (4.38)$$

Using identity $2 \sin \theta \sin \varphi = \cos(\theta - \varphi) + \cos((\theta + \varphi))$:

$$\xi' = -2 \sin(2\alpha_{S0}) \sin(2\alpha_{P0}) \sin(2\theta) \theta'.$$

Since $\theta = \Delta k(z - \frac{L}{2}) + [\delta_{S0} - \delta_{P0}]$ the derivative of θ is $\theta' = \Delta k$, and it follows:

$$\xi' = -2\Delta k \cdot \sin(2\alpha_{S0}) \sin(2\alpha_{P0}) \sin(2\theta)$$

$$\xi' = -2\Delta k \cdot \sin(2\alpha_{S0}) \sin(2\alpha_{P0}) \sin[\Delta k(2z - L) + 2(\delta_{S0} - \delta_{P0})] \quad (4.39)$$

we set $\xi' = 0$ to investigate for extremes. This requires following conditions to be met:

- Condition-1:

$$\Delta k = 0 \quad (4.40)$$

which means there is no change in ξ , hence there is no birefringence present in the fiber

- Condition-2:

$$\sin(2\alpha_{S0})\sin(2\alpha_{P0}) = 0 \quad (4.41)$$

This condition can be fulfilled if we have:

$$\alpha_{S0}(z) = m \frac{\pi}{2} \quad (4.42a)$$

or:

$$\alpha_{P0}(z) = m \frac{\pi}{2} \quad (4.42b)$$

For $m = 0, 1, 2 \dots$ In that case $\xi = 1$ and we have maximum gain. Physically the condition (4.47) means that the polarization of both waves is linear along the principal polarization axes.

- Condition-3:

$$\sin[\Delta k(2z - L) + \Delta k(2z - L)] = 0 \quad (4.43)$$

$$\Delta k(2z - L) + 2(\delta_S - \delta_P) = m\pi \quad (4.44)$$

$$z = \frac{1}{2} \left[\frac{m\pi - 2(\delta_S - \delta_P)}{\Delta k} + L \right] \quad (4.45)$$

Now, it shall be noticed that condition-3 in combination with the condition $\alpha_{S0} - \alpha_{P0} = \frac{\pi}{2}$, in which polarizations of linearly polarized pump and Stokes waves are orthogonal, will result with $\xi = 0$. Hence, in such case there is no gain. In order to generate such a condition, we need to manipulate the polarization on both launch ends, the pump and the Stokes port, until we observe $\xi = 0$. The situation is depicted in Fig.-4.11. As with the earlier case, ξ undergoes periodic changes along the fiber length z and extremes are periodically located. If Δk is constant, ξ across Δkz -plane is a straight vertical line, exhibiting clear periodic characteristics. But if Δk is changing along the length, then ξ will be a curve undergoing slower or faster changes depending on Δk . In other words, perturbed Δk modulates ξ . The change rate of ξ

reveals the information that Δk changes along the length. This now suggests the following; applying the pure signal processing technique, for example Fourier transformation (FFT) on ξ , it can lead us to the conclusion on Δk values. From the practical point, this technique requires, if feasible, provision of several sampling points in order to profile Δk in each point of interest within one spatial resolution length. From the industrial point of view, this method is worth investigating if a BOTDA with spatial resolution in [cm] range is available, however, this is not our case for the time being.

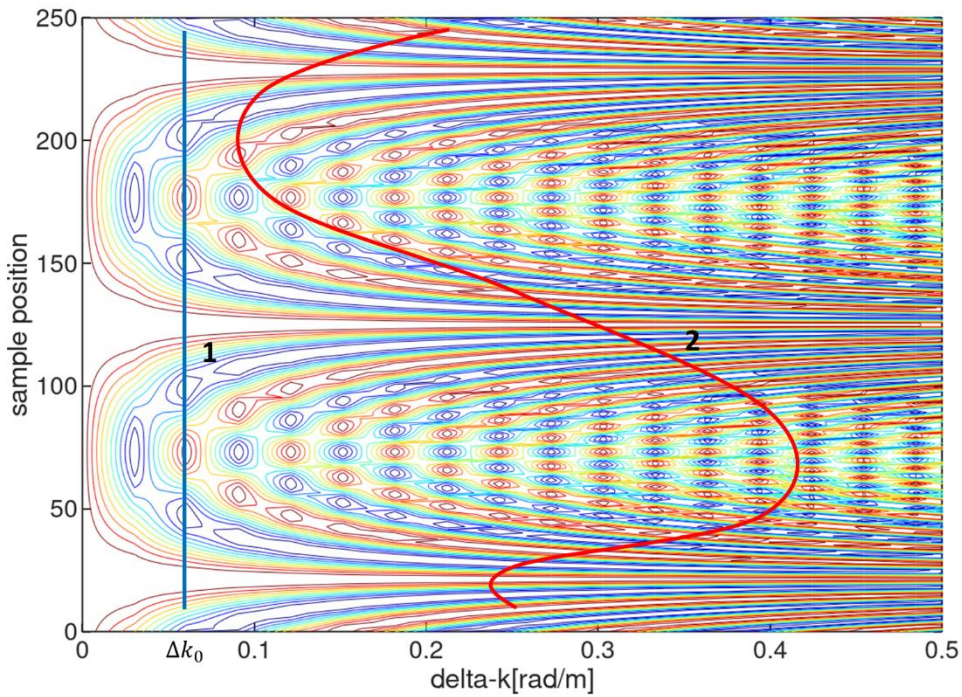


Figure-4.11: The constant Δk , $\Delta k = \Delta k_0$ – blue line (1), results with the polarization efficiency function ξ having regular sinusoidal periodicity, whereas varying Δk (2) causes frequency modulated ξ – red line (2). The distance between extremes is larger for lowest Δk values.

Therefore, we will continue with the method of Δk determining according to the idea of observing ξ and seeking extremes along the length of the fiber. The distance between two adjacent extreme positions in which ξ has a minimum ($\xi = 0$) is:

$$\Delta z = \underbrace{z(m+2)}_{\substack{\text{the reading of } \xi \\ \text{the right minimum} \\ \text{for } \Delta k_0}} - \underbrace{z(m)}_{\substack{\text{the reading of } \xi \\ \text{the left minimum} \\ \text{for } \Delta k_0}} \quad (4.46)$$

For the same $\Delta k = \Delta k_0$ we are confined with a vertical line in Δkz -plane and we have:

$$\Delta z = \frac{1}{2} \left[\frac{(m+2)\pi - 2(\delta_S - \delta_P)}{\Delta k_0} + L \right] - \frac{1}{2} \left[\frac{m\pi - 2(\delta_S - \delta_P)}{\Delta k_0} + L \right] \quad (4.47)$$

$$\Delta z = \frac{2\pi}{\Delta k_0} \quad (4.48)$$

In other words, $\Delta z \Delta k_0 = 2\pi$. Hence, the larger Δk_0 requires smaller Δz to jump from one minimum to the next minimum along the vertical line in Δkz -plane. For smaller Δk_0 it is just the opposite and larger Δz is required to make the phase shift of 2π .

Let us consider now one 2π shift in the arbitrary direction in Δkz -plane. For such transition from $(z_m, \Delta k_1)$ to $(z_{m+2}, \Delta k_2)$ and using (4.34) we can write:

$$\begin{aligned} \Delta z_{21} &= z_{m+2} - z_m \\ \Delta z_{21} &= \frac{1}{2} \left[\frac{(m+2)\pi - 2(\delta_S - \delta_P)}{\Delta k_2} + L \right] - \frac{1}{2} \left[\frac{m\pi - 2(\delta_S - \delta_P)}{\Delta k_1} + L \right] \end{aligned} \quad (4.49)$$

And with some manipulation we obtain:

$$\Delta k_2 = \frac{(m+2)\pi - 2(\delta_S - \delta_P)}{m\pi + 2\Delta k_1 \Delta z_{21} - 2(\delta_S - \delta_P)} \quad (4.50)$$

Expressed in another way, for Δz_{21} :

$$\Delta z_{21} = \frac{1}{2} \left\{ \left(\frac{1}{\Delta k_2} - \frac{1}{\Delta k_1} \right) [m\pi - 2(\delta_S - \delta_P)] + \frac{2\pi}{\Delta k_2} \right\} \quad (4.51)$$

The expression (4.51) can be easily tested. For example, if we set $\Delta k_1 = \Delta k_2 = \Delta k_0$ in (4.51) we will get (4.48) again. This now represents a more general case in Δkz -plane and Fig.-4.12 shows these general transitions in Δkz -plane.

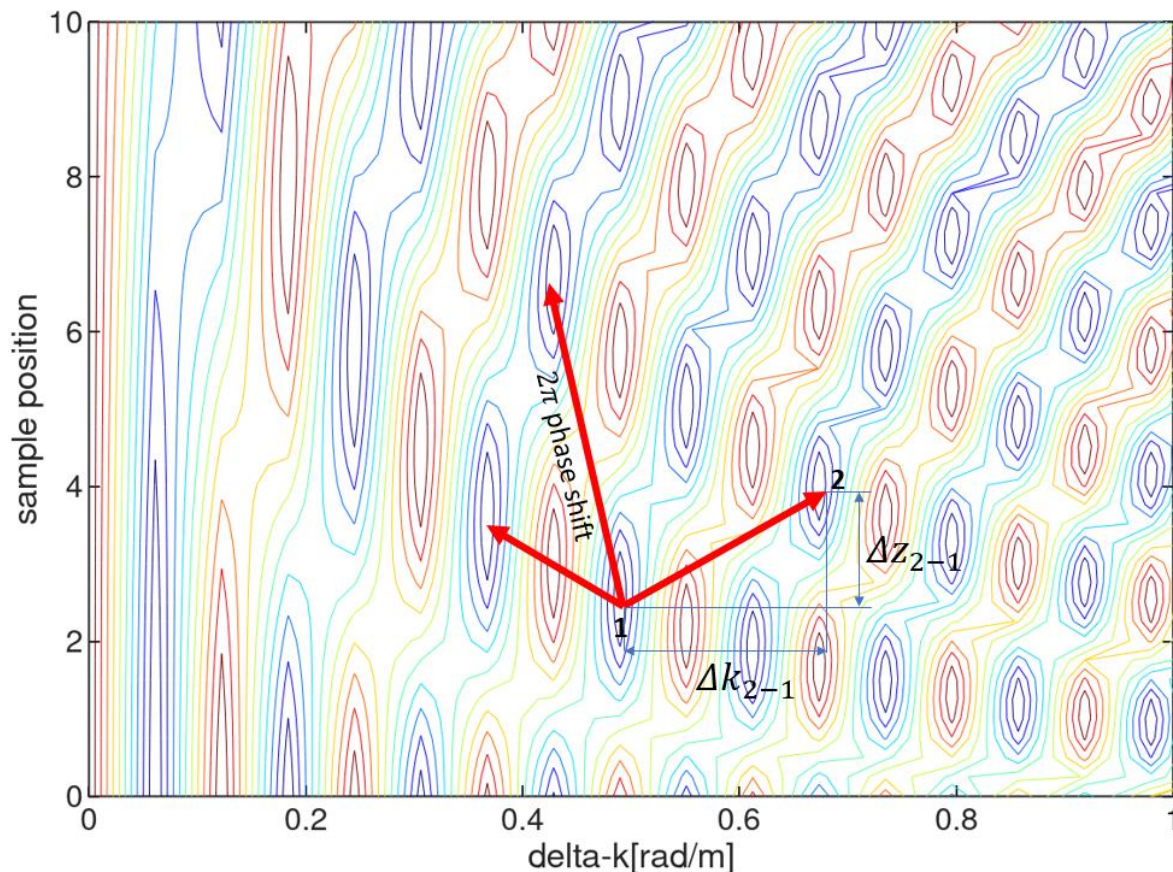


Figure-4.12: Graphical representation of general transition from one extreme to the other giving the phase shift of 2π radians. Increase in Δk must be compensated by decrease in Δz in order to maintain the same phase distance.

Let us now summarize the analysis so far, the measurement perspectives, and provide comments regarding the possible impact of the temperature in the measurements:

- Both concepts exploit Δkz -plane defined with (4.23). It is a plane on which polarization efficiency ξ makes its blueprint.
- The configuration of ξ in the Δkz -plane can be changed by changing polarization parameters α_{s0} , α_{p0} , and phase retardances δ_{p0} , and δ_{s0} at the inputs.
- With α_{s0} , α_{p0} , δ_{p0} constant and varying the Stokes wave phase δ_s this blueprint can be shifted vertically in Δkz -plane. At the same position z_0 and with the manipulation of the Stokes wave phase δ_s we can calculate Δk .

- Finding extremes in ξ is a method that can give Δk . The most convenient way of scanning the $\Delta k z$ -plane can be horizontal, by means of changing the phase of the Stokes wave, and vertical, by means of tracking the Brillouin gain signal across the length. The scanning can also be made in the arbitrary direction and the benefits then needs to be considered in a separate analysis.
- In the horizontal scanning method, we presumed that for the frequency span of the Brillouin interaction, Δk can be taken as independent from wavelength scanning but proportional to pressure change, because of the pressure-birefringence mechanism featured by the cable. Horizontal scanning can be conducted by setting an initial working point $(\Delta k_1, z_0)$ and then manipulating phase difference $\delta_S - \delta_P$ by changing and noting the δ_S (and leaving δ_P unchanged), until ξ undergoes the next extreme with the 2π shift. Knowing $(\Delta k_1, z_0)$, the overall loop length, and measuring δ_S we can calculate Δk_2 according to (4.36). From the practical point of view, an accurate measurement requires calibration of the sensor cable, measurement of Brillouin-Lorentzian profile, and manipulation of the phase of Stokes wave, and finally the calculation of Δk_2 . In the calibration process we determine the $\Delta k(p)$ characteristics along the whole length of the cable. The horizontal method includes only phase manipulation and it does not require data from more spatial sampling points. Hence, Δk_2 can be determined in just one sampling location.
- In the vertical scanning method, we must move along sampling points until we find the same phase – it means 2π phase shift. We measure the distance and calculate Δk_0 using (4.48). The transition to a larger Δk_0 value will make the 2π phase shift to appear sooner. In this case no phase shift is included and monitoring of ξ is sufficient. This is the main difference between the methods; methods using phase shift require only one sampling position to calculate Δk_2 , whereas methods requiring a series of sampling positions in profiling ξ require longer segments with constant Δk_0 values to calculate it. The first approach uses an additional device for phase manipulation, and the second spares the investment of the cost of the minimum resolution length required for acquisitions of data. As it is usually the case, the decision shall be made according to requirements from the application.

- Temperature impact: temperature change introduces the phase shift in polarization efficiency ξ along the fiber. When α_{S0} , α_{P0} , δ_{P0} , and δ_{S0} are constant, the form of the blueprint of ξ in the Δkz -plane shall remain the same and it will be only shifted vertically - as long as Δk is constant. Should Δk be affected by temperature change, and this coupling is due to the cable, the blueprint of ξ will also change. In that case our job is to make the cable with Δk dependent on pressure only and free from temperature impacts, at least in the temperature range of our interest.

3.4. Measurement set-up and results

This chapter will give an example of the measurement based on extraction method 2 described above. The measurement is conducted using a 24m long pressure chamber in which the cable prototype is installed and sealed and then integrated into BOTDA (Omnisens Vision Dual) [18] closed fiber loop configuration (Fig.-4.13). The pressure change p will change Δk in the optical fibers inside the cable, that will, in turn, give rise to the ripples in ξ .

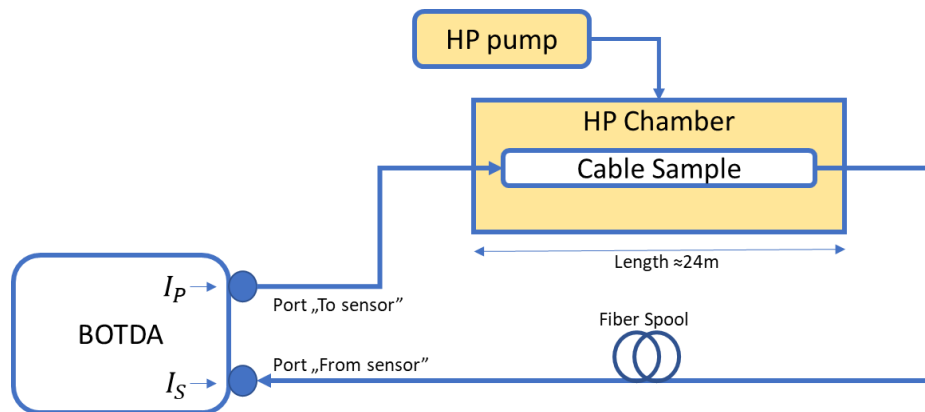


Figure-4.13: Measurement set-up for determination of distributed Brillouin gain dependence on pressure rate

The instrument performs the configuration first, and the measurement afterwards. In the configuration phase it seeks the maximum in the Brillouin interaction. Launching polarizations are adjusted and regulated to generate maximum gain. Once the maximum Brillouin interaction along the length is found, pump polarization is fixed and remains unchanged. The perturbances within the fiber, i.e. within the tested part of the fiber loop, can impact polarization properties of the pump light and cause variations in Brillouin gain. Since both lights are generated from the same laser source, the stable wavelength difference between the two lights is assured which is required for accurate wavelength scanning and quality of measurement results. During the measurement, the Stokes wave scans the fiber across the Brillouin interaction range, and measurement data are acquired.

The measurement is done in steps. In each step pressure is increased by 100bar. The applied pressure range is from 0 to 800bar. The spatial resolution and Stokes frequency scanning step was taken to be 1.02m and 2MHz, respectively, and the spatial sampling interval was 0.4m. So, we had 2 sampling points along 1 resolution length.

In order of avoid zero gain at certain locations along the cable, BOTDA samples the backscatter signal in characteristic axes and then averages the results. In this way polarization fading of the Brillouin signal is completely mitigated. The measurement concept and data analysis start with Brillouin gain processing. The equation (2.73) can be written in the form:

$$\underbrace{g_B[\Delta k(\Delta p)]}_{\text{measurement}} = \xi \cdot \underbrace{\Delta k(\Delta p)}_{\text{provision of } \Delta k} \cdot \underbrace{g_{Bmax}}_{\substack{\text{interaction} \\ \text{gain} \\ \text{maximum}}} \cdot \underbrace{f(\varepsilon, T)}_{\substack{\text{interaction} \\ \text{shape and position}}} . \quad (4.54)$$

Now taking the first derivative:

$$g'_B = g_{Bmax} \cdot f \cdot \xi' \quad (4.55)$$

Using (4.23) we can write:

$$\xi' = -\frac{1}{2}(2z - L)[\cos^2(\alpha_S - \alpha_P) - \cos^2(\alpha_S + \alpha_P)] \cdot \Delta k(\Delta p)' \cdot \sin[\Delta k(\Delta p)(2z - L) + 2(\delta_S - \delta_P)] \quad (4.56)$$

Expression (4.56) in combination with (4.55) gives:

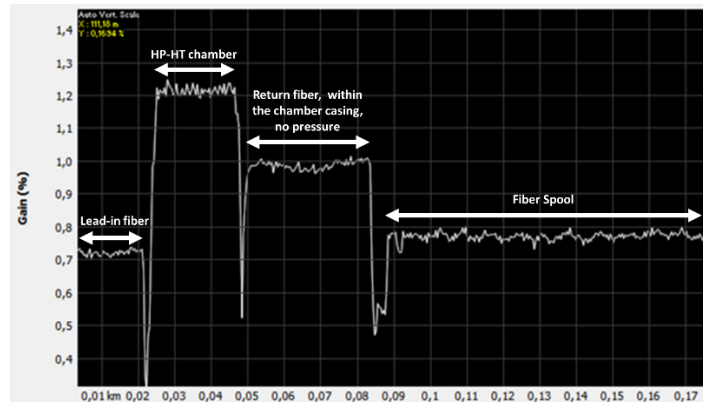
$$g'_B[\Delta k(p)] = \eta \cdot \xi'[\Delta k(p)] \quad (4.57)$$

Where η is defined as $\eta = g_{Bmax} \cdot f$ and includes everything except phase and launching polarization conditions.

This means that both g'_B and ξ' will share the same form and will undergo extremes for the same argument $\Delta k(p)$. Hence, they share the same blueprint in Δkz -plane. The only difference is the coefficient η .

Now, our task is to profile g_B in Δkz -plane and from that we will estimate ξ' . Fig.-4.14 roughly shows the spatial Brillouin profile and gain variations as a function of pressure change for the tested sample. For more precise measurements new measurement set-up must be arranged, this time with a finer pressure increase step. Pressure p is referenced to atmospheric pressure.

The results of the Brillouin gain are depicted in Fig.-4.15. At pressure levels between 0-100bar there is a uniform drop in Brillouin gain across the whole length. At higher pressure rates, Brillouin gain undergoes ripples.



(a)



(b)

Figure-4.14: Spatial profile of Brillouin gain as a function of pressure. The reference curve (a) shows loop segment details, and periodic variations (b) due to birefringence change. It was observed that variations are higher for low pressure values and lower on higher pressure values.

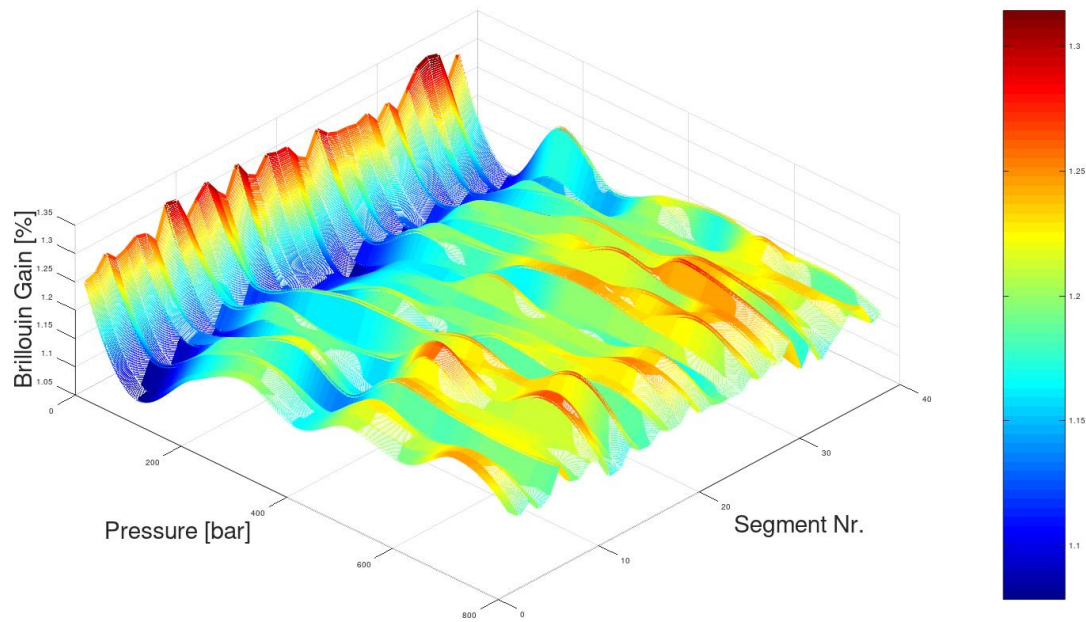
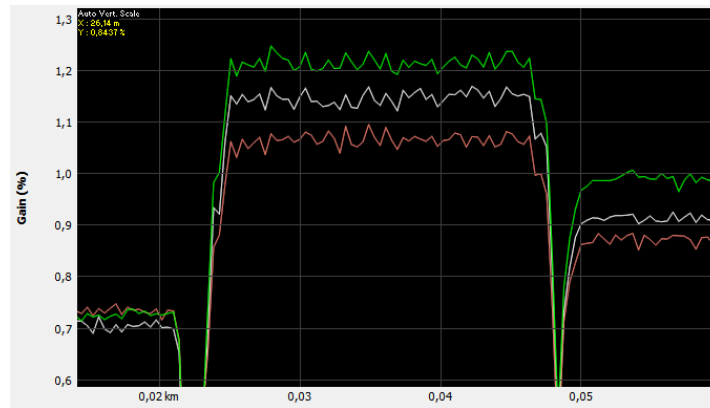


Figure-4.15: Brillouin gain with ripples due to birefringence as a result of applying the external pressure on the sample. The gain is dependent on pressure values on all positions along the sample.

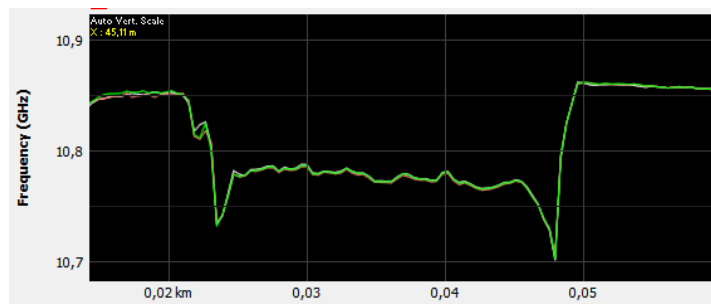
The change in Brillouin gain is uniform along the length in the chamber (Fig.-4.16), and the Brillouin-Lorentzian peaks (Fig.-4.16b) and the FWHM (Fig.-4.16c) remains unperturbed during the pressurization process. The pressurized segment changes its birefringence and it impacts Brillouin interaction of the rest of the fiber loop, meaning that the gain characteristics from pressure-free segments in the loop, on the left and right side of the chamber, will change. Since it changes the spatial distributions of the pump and the Stokes waves, the introduction of one birefringent segment into a birefringence-free loop impacts the Brillouin interaction along the entire fiber.

For our consideration, only ripples in the gain are of our interest. For that purpose, taking the derivative of the gain profile gives better insight into periodicity of the ripples as a result of applied pressure (Fig.-4.17). This 2π periodicity can be observed as a span between the colored segments having the same color transitions (yellow-red transition), as depicted in Fig.-4.17. The results presented graphically suggest that there is a difference in sensitivity between the segments of the cable inside the chamber and across the pressure range. Nevertheless, the most coherent and homogenous results for all segments are found in the pressure range around 100bar

(Fig.-4.18). It can be observed that the segments in the range nr. 0-10 have similar pressure sensitivity and follow the same pattern, as well as those above segment nr. 36.



(a)



(b)



(c)

Figure-4.16: Brillouin gain parameters for pressure rates 0bar (green line), 100bar (pink) and 800bar (white line); the spatial gain profile (a), peak frequency profile f_B (b), and the Brillouin-Lorentzian FWHM width profile Δf_B (c). Both f_B and Δf_B remain approximately unchanged in the process. The examined sample is located between 24m and 48m in the trace.

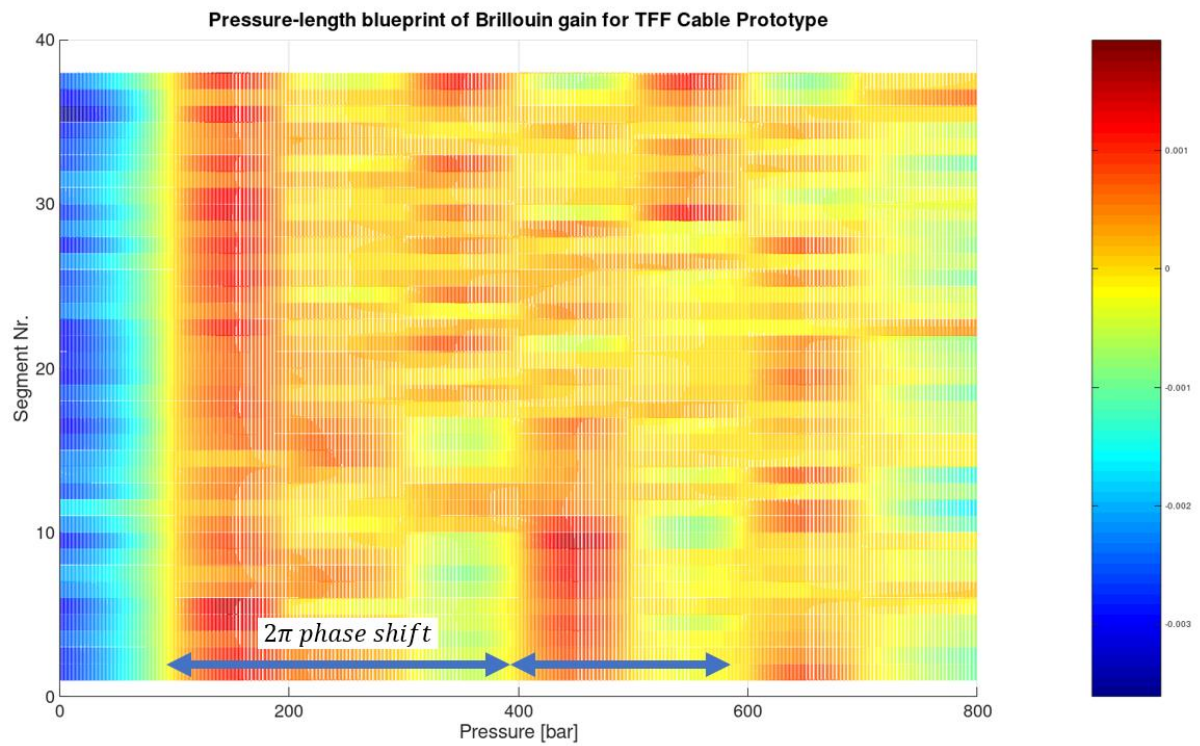


Figure-4.17: Mesh representation of Brillouin gain derivative in Δk_z -plane revealing 2π phase periods. The minimums are found in the transition zones from yellow to red, in the direction left to right. The distance from two adjacent minimums corresponds to 2π phase shift.

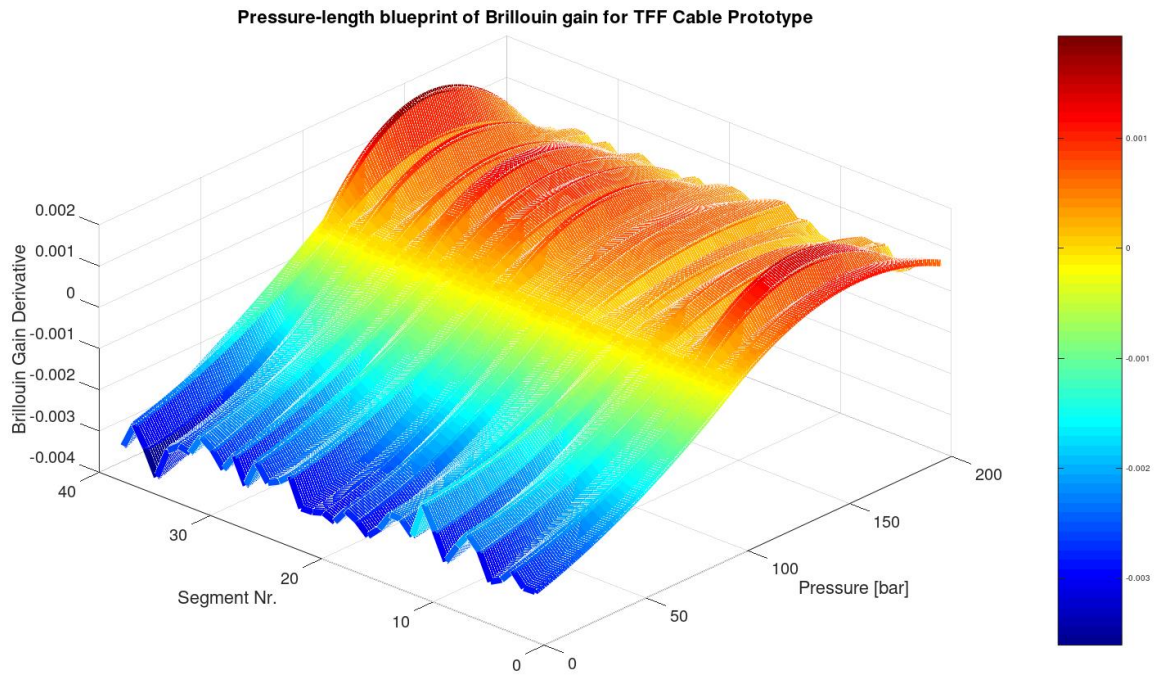


Figure-4.18: Brillouin gain derivative. The most homogenous results for all segments are found in the pressure range around 100bar

According to the results, approximate sensitivity can be calculated for the sample (Table-4.3).

TABLE-4.3: EVALUATION OF PRESSURE DISTRIBUTION ALONG THE SAMPLE IN THE PRESSURE CHAMBER

Segment nr. /range	Pressure range [bar]	Sensitivity rad/bar
0-10	100 - 380	1.65E(-2)
0-38	380 - 580	3.14E(-2)

The purpose of this chapter was to show and discuss the directions of development of fully distributed fiber optic pressure measurement systems. They are based on BOTDA measurements, but possibilities are not limited to one interrogation technique. It has the potential to be greatly improved in the future. For even better concepts and results, access to raw data from the BOTDA unit is necessary. Namely, some of the usable measurement data is are not available and remain hidden in the system hardware. In the time this thesis was being written, the high-pressure chamber was in the process of moving to a new location and unavailable for more tests with better precision. New activities on pressure measurements involving the approach with higher precision and advanced interrogation techniques (now based

on novel knowledge acquired) and data processing are planned in the near future. Without any doubts, with slight technical adaptation in commercially available BOTDA units, further improvement can be realized, especially in measurement precision and data processing. For that reason, we contacted the manufacturer of the BOTDA unit – the company Omnisens [18]. It can be said with confidence that further advances of distributed pressure measurements techniques will be made in the years ahead.

The other, larger part necessary for the success of the fiber optic fully distributed pressure sensing concept and its industrial acceptance lay in the hands of sensor cable manufacturers, especially in the quality and the precision of cables that present manufacturing technology can offer. In that respect, linear characteristics and the calibration of such cables are probably the largest challenge. If we denote the $\Delta k_2 - \Delta k_1$ transition distance and define sensitivity of the cable as $s_p = \frac{d}{dp} \Delta k$ then for some phase transition, φ we can write:

$$\varphi = \frac{2\pi}{\Delta k_2 - \Delta k_1} \cdot s_p \cdot (p_2 - p_1) \quad (4.58)$$

$$\underbrace{p_2}_{\text{calculated}} = \frac{\overbrace{\tilde{\varphi}}^{\text{reading from VR}}}{2\pi} \cdot \left(\underbrace{\Delta k_2}_{\text{measured}} - \underbrace{\Delta k_1}_{\text{reference}} \right) \cdot \frac{1}{\underbrace{s_p}_{\text{cable calibration}}} + \underbrace{p_1}_{\text{reference}} \quad (4.59)$$

In case we select the 2π phase transition from Δk_1 to Δk_2 , take that the reference pressure $p_1 = 0$, and calculate Δk_2 using the above described methods, we then get:

$$p_2 = \frac{\Delta k_2 - \Delta k_1}{s_p} \quad (4.60)$$

Once again $(\Delta k_1, p_1)$ must be known from calibration. Because this method belongs to a relative type of measurements for accurate pressure estimation, the cable calibration s_p is of major importance. The repetition of the same parameters on every meter along the length during the production process makes the calibration easier. If that cannot be accomplished, then the calibration process of long cable lengths would be very costly and challenging. Hence, one of the most important objectives in the pressure sensing cable design is the simplicity of the calibration process. The simpler the calibration, the lower the costs in production are and the easier is the acceptance from the industry.

4. BENDING OF THE CABLE

The availability of more tightly buffered off-centered fibers inside the metal encapsulation tube is growing in industry thus introducing new possibilities for cable bending detection and measurements. Bending measurement is based on principles of bar bending (Fig.-5.1) in which the cross-section above neutral axis is subjected to extension, while the cross-section below the neutral axis is subjected to compression. The line that is confined with the neutral axis plane is subjected to none of it, no compression and no extension and hence it will be not subjected to stress.

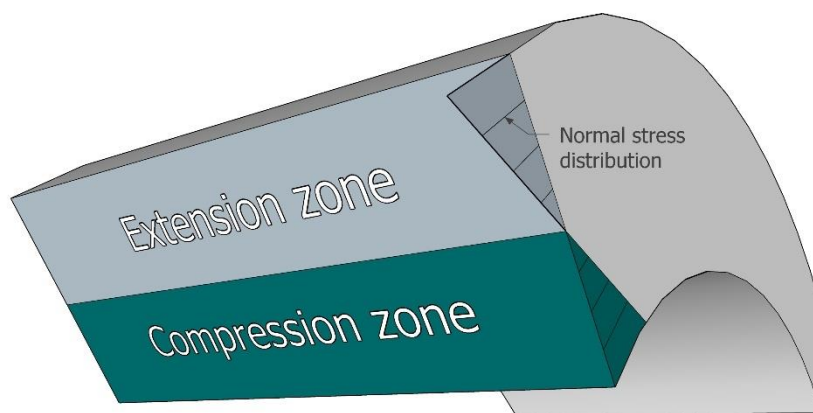


Figure 5.1: Bent bar and its normal stress distribution ϵ_n

In order to evaluate bending of fiber optic cable, the optical fibers shall be grouped into an extension and compression zones of the cable cross-section. In case they are located symmetrically with respect to neutral axis, the strain induced perturbations shall be equal in magnitude but antisymmetric, hence have the opposite signs. Such a cable is depicted in Fig. 5.2.

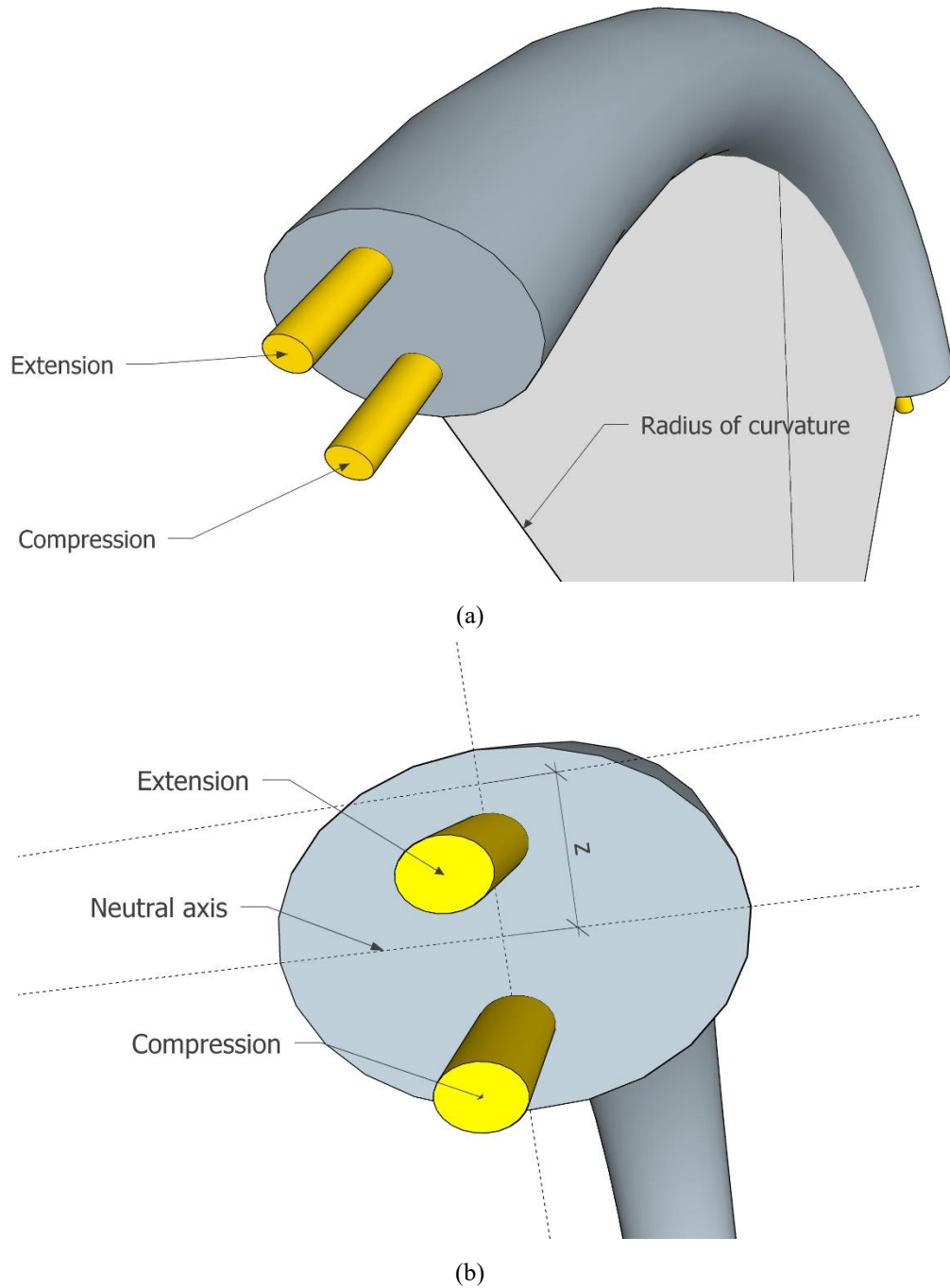


Figure 5.2: Concept of bar bending and detection using optical fibers

Normal strain in the beam can be expressed as follows.

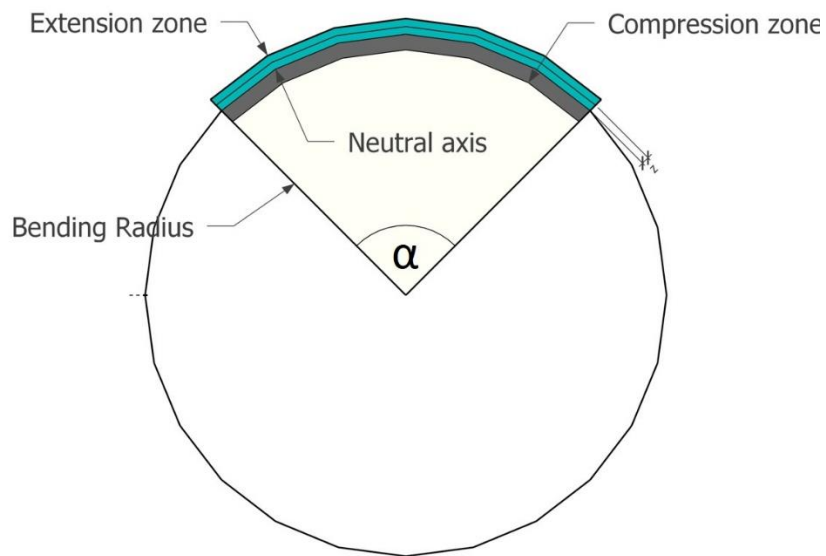


Figure 5.3: Model of a cable bend

The circumference of the circularly bended cable with radius ρ is calculated as (Fig.-5.3):

$$O = 2\rho\pi \quad (5.1)$$

Now, we use proportionalities that involve:

- arc l
- circumference O
- angle α

$$\frac{l}{O} = \frac{\alpha}{2\pi} \quad (5.2)$$

$$\frac{l}{2\rho\pi} = \frac{\alpha}{2\pi} \quad (5.3)$$

Here we obtain:

$$\alpha = \frac{l}{\rho} \quad (5.4)$$

Relative strain ε is defined as:

$$\varepsilon_r = \frac{\Delta l}{l} \quad (5.5)$$

Therefore, we can write:

$$\Delta l = \frac{dl}{d\rho} \Delta\rho \quad (5.6)$$

Combining (5.6) with (5.4) we have:

$$\Delta l = \frac{d}{d\rho} (\alpha\rho) \Delta\rho \quad (5.7)$$

So, we obtain:

$$\Delta l = \alpha \Delta\rho \quad (5.8)$$

Using (5.4) and (5.5) we get:

$$\Delta l = \frac{l}{\rho} \Delta\rho \quad (5.9)$$

$$\varepsilon_r = \frac{\Delta l}{l} = \frac{\Delta\rho}{\rho} \quad (5.10)$$

We can replace increment of the radius $\Delta\rho$ with the distance from the cable's neutral axis z :

$$\Delta\rho = z$$

$$\varepsilon_r = \frac{1}{\rho} z \quad (5.11)$$

As the radius of the curvature grows to infinity, normal strain decreases to zero. Table 5.1 and Fig.-5.4. show relative elongation due to bending in micro-strain units.

TABLE 5.1: RELATIVE ELONGATION IN ϵ AS A DEPENDENCE OF DISTANCE FROM NEUTRAL AXIS z WITH CABLE BENDING OD AS PARAMETER

z [mm]	Bending OD						
	2000 [mm]	1750 [mm]	1500 [mm]	1250 [mm]	1000 [mm]	750 [mm]	500 [mm]
0,10	100,00	114,29	133,33	160,00	200,00	266,67	400,00
0,20	200,00	228,57	266,67	320,00	400,00	533,33	800,00
0,30	300,00	342,86	400,00	480,00	600,00	800,00	1200,00
0,40	400,00	457,14	533,33	640,00	800,00	1066,67	1600,00
0,50	500,00	571,43	666,67	800,00	1000,00	1333,33	2000,00
0,60	600,00	685,71	800,00	960,00	1200,00	1600,00	2400,00
0,70	700,00	800,00	933,33	1120,00	1400,00	1866,67	2800,00
0,80	800,00	914,29	1066,67	1280,00	1600,00	2133,33	3200,00
0,90	900,00	1028,57	1200,00	1440,00	1800,00	2400,00	3600,00
1,00	1000,00	1142,86	1333,33	1600,00	2000,00	2666,67	4000,00

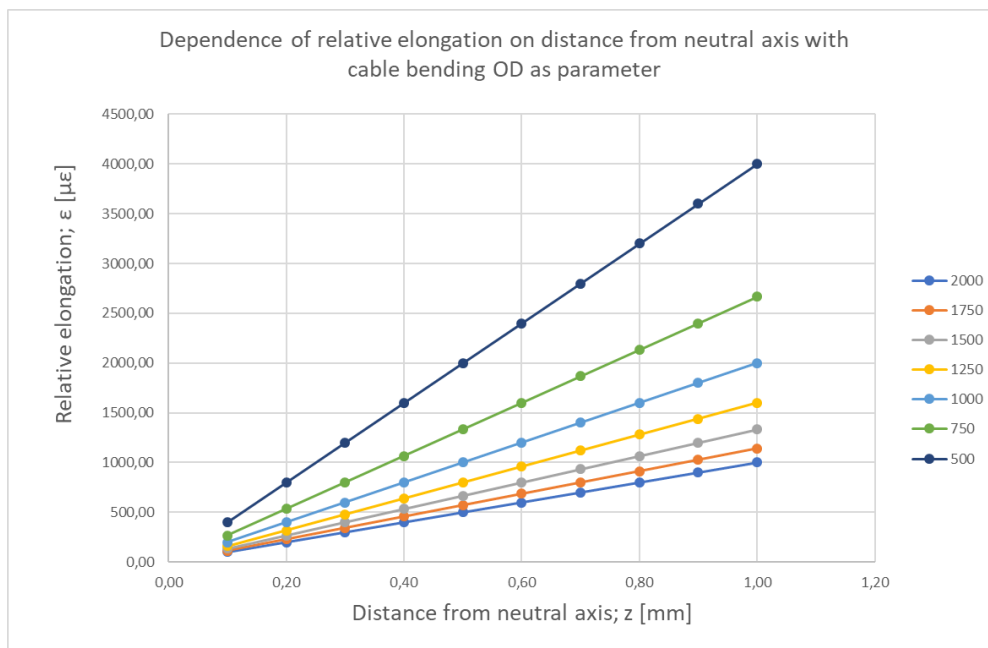


Figure 5.4: Relative elongation in dependence of distance from neutral axis z with cable bending OD as parameter

The bending of the cable with two fibers depicted in Fig.-5.4 is dependent on the azimuthal position of the fibers. The extension and compression is antisymmetric and as such it can be measured. The sensitivity of the configuration with 2 fibers is twice the one with one fibers and peaks at the farthest point within the compression or extension zones relative to the neutral axis. If both fibers are positioned in the neutral plane, the situation will change. In such case, the fibers are free from mechanical loads and the bending effect will be lost. The measurement results from both fibers shall be zero and no antisymmetric curves will be detected. This represents a drawback of such a concept. Since keeping/regulating the position of fibers in very

long production lengths is impossible, the information on cable bending at some locations can be lost.

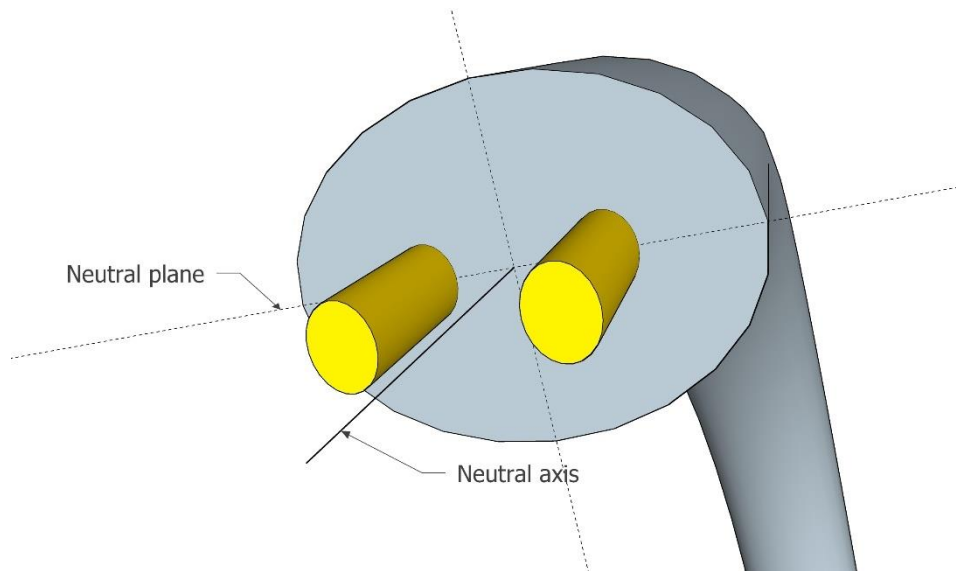
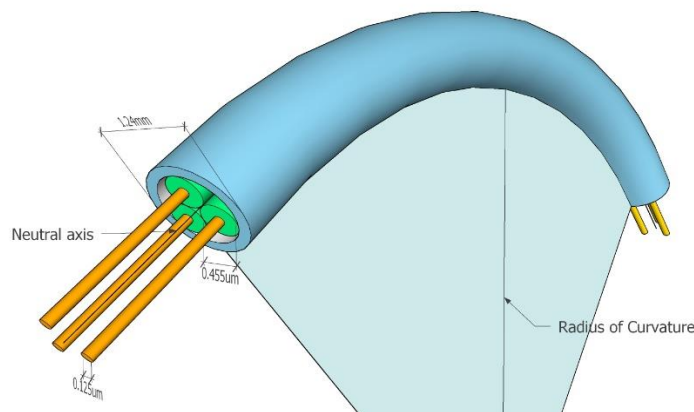
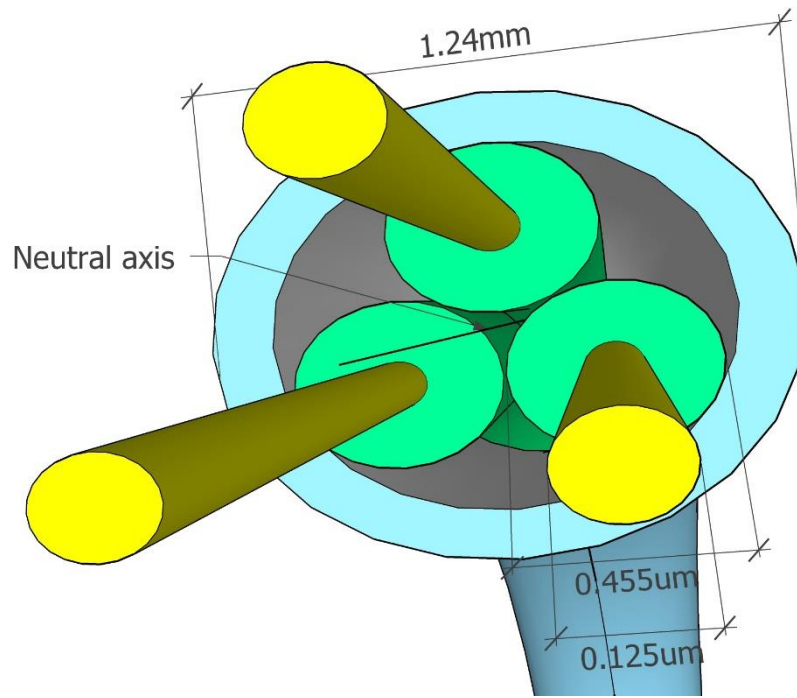


Figure 5.4: Configuration providing bending unperturbed optical fibers

With three fibers with an azimuthal offset angle of 120° , the situation is quite different (Fig.-5.4). In such configuration at least one fiber will always be in the compression and one in the extension zone assuring necessary antisymmetric balance in the measurement, no matter what azimuth angle optical fibers will take during cable production. Therefore, in this way there will always be available information on cable bending status presuming that all three fibers are interrogated. The cost of this additional option is a necessity for the introduction of the third fiber into the sensor cable and conducting one additional measurement. The concept with three fibers (Fig.-5.5) comes with some additional benefits.



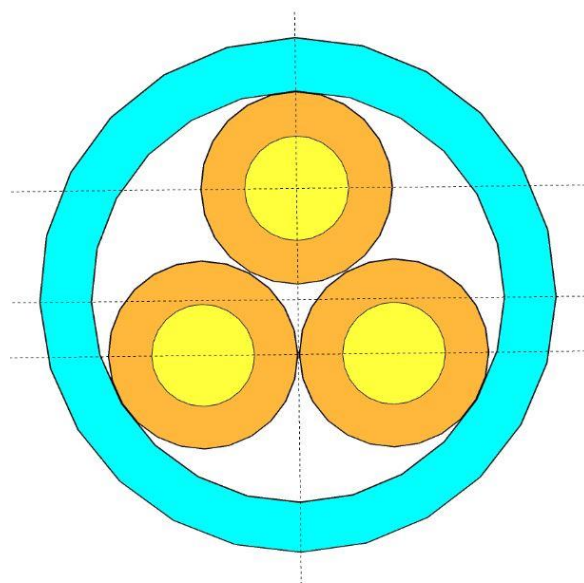
(a)



(b)

Figure 5.5: Trisens cable bended; (a) dimensions and (b) zoomed cross-section

In comparison with the two-fiber system, the three-fiber configuration introduces a difference in stress magnitude among the fibers (Fig.-5.6a). For the three-fiber system, the only position in which magnitudes of the two fibers can be equal in magnitude but opposite in sign is the position in which one fiber is positioned in the neutral plane (Fig. 5.6b).



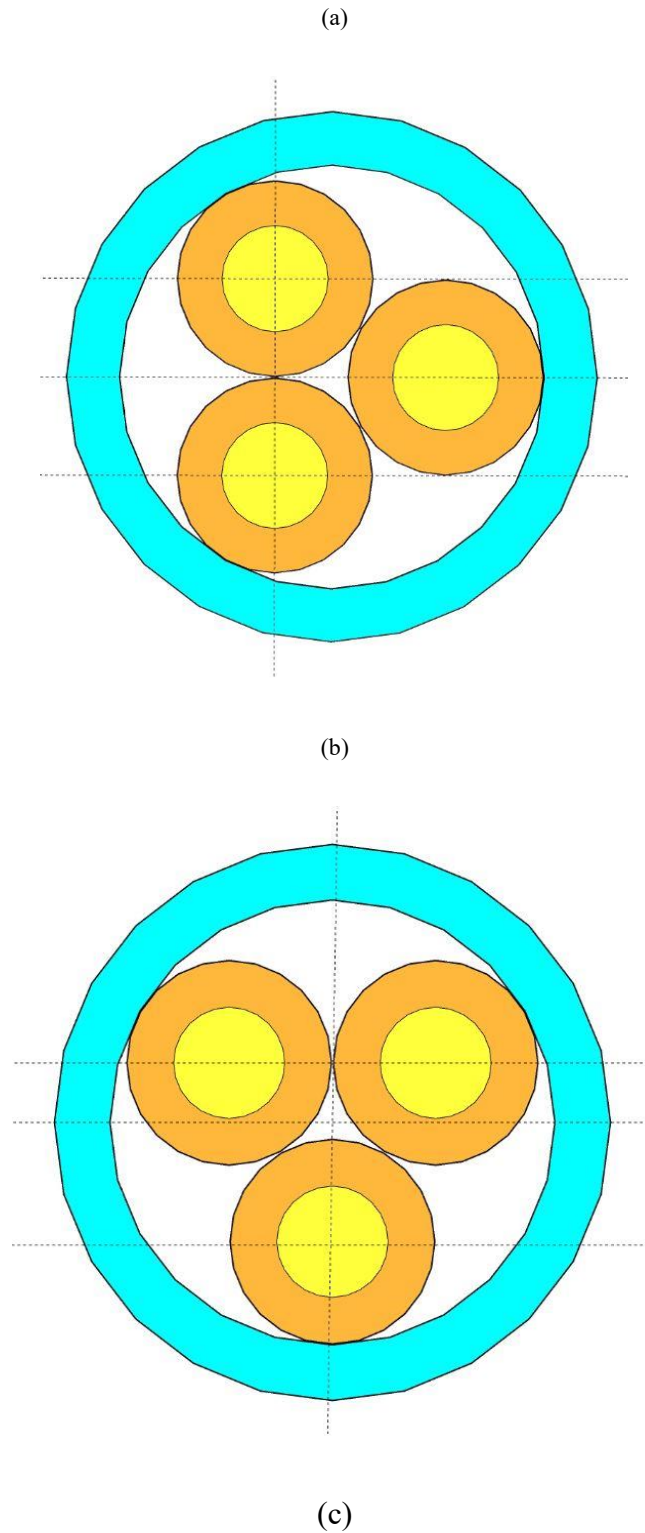
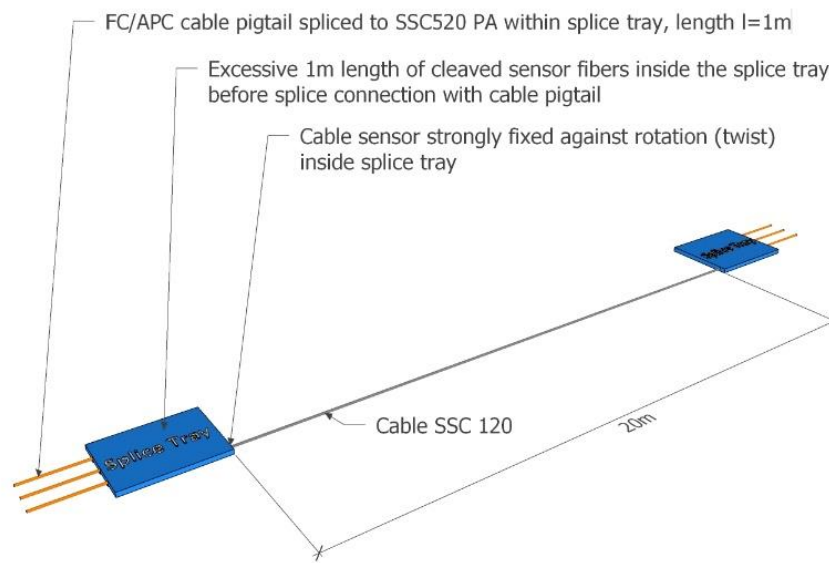


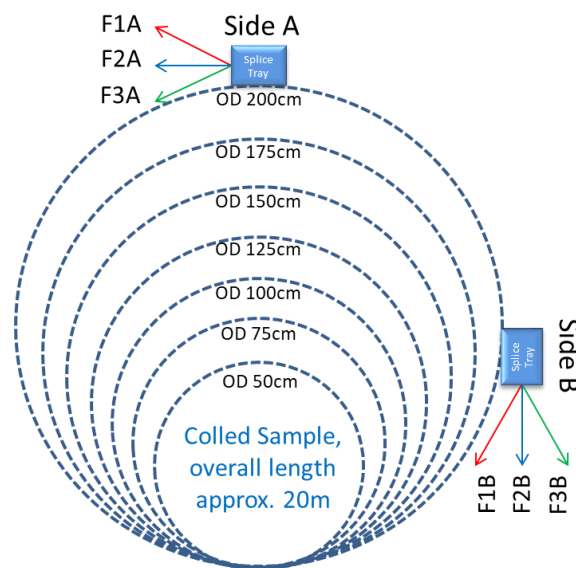
Figure 5.6: Azimuthal configuration of the cross-section and magnitudes in extension and compression zones; (a) magnitudes are different, (b) magnitudes are the same, and (c) same as (a) but with opposite sign

In other words, looking at the responses from the optical fiber, we can evaluate angles and magnitude of the bending the cable is subjected to. The bending measurement using BOTDA

is organized by coiling a 20m long cable segment (Fig. 5.7a). The diameters of the coils are 200cm, 175cm, 150cm, 125cm, 100cm, 75cm and 50cm (Fig. 5.7b). It was connected to the measurement set-up (Fig. 5.7c) by a fusion splice in a splice tray. The full Brillouin-Lorentzian profile measurement is shown in the upper-right picture bearing all information necessary for evaluation of the bending. The unit provides information on; Brillouin gain and width (FWHM), and frequency position of the peak. The latter is the most important parameter in the application as it bears information on the strain and the temperature. The information on strain is the focus of our measurements.



(a)



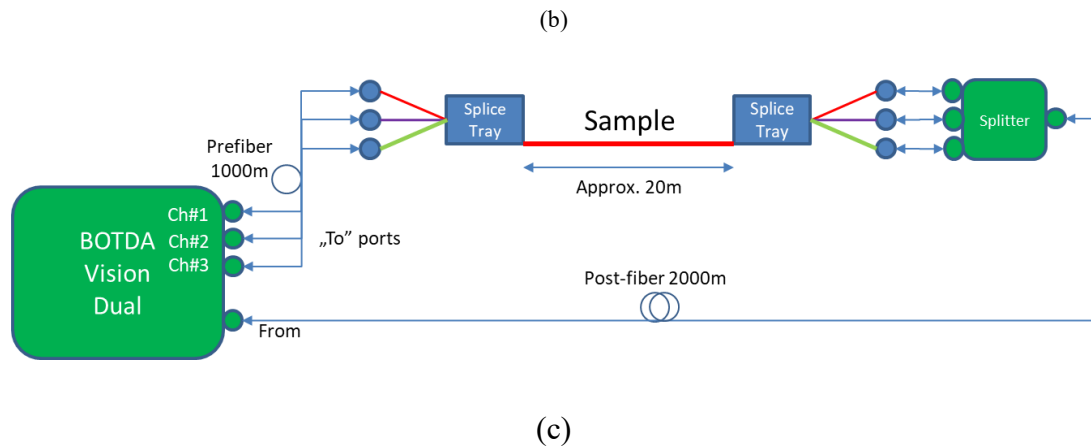


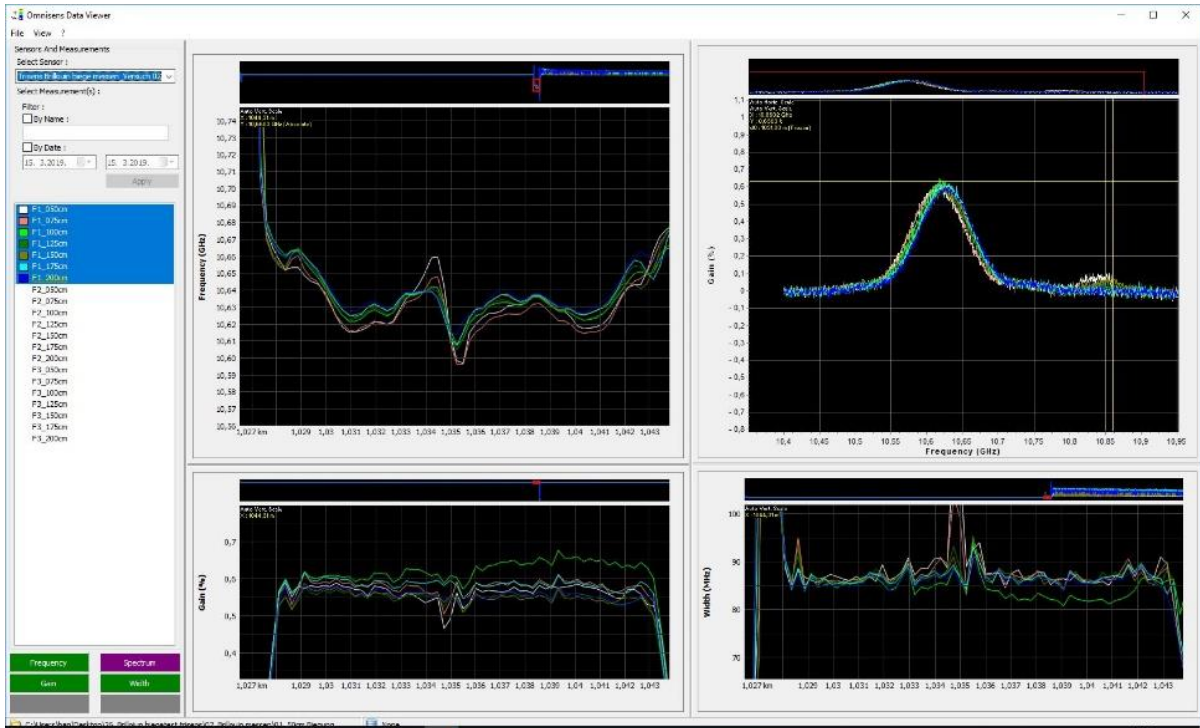
Figure 5.7: The samples and the measurement (a) the construction of the sample, (b) coiling/bending of the sample and (c) measurement set-up

Fig.-5.8 shows BOTDA measurement results from all three fibers with all details; the upper right pictures depict the Brillouin-Lorentzian profile and the rest of the figures show the details of it - the upper-left curve profiles frequency position of the peak, bottom-left shows the gain, and the bottom right shows FWHM width of the Brillouin-Lorentzian profile.

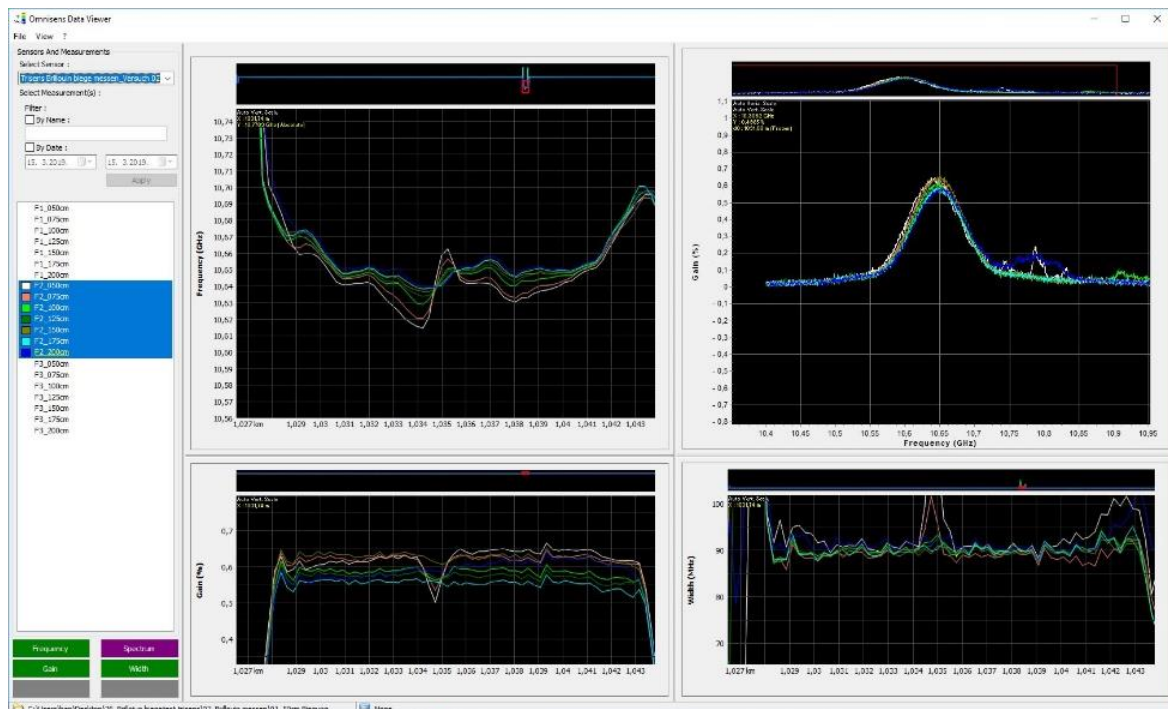
The coil is arranged in the following procedure;

- The straight cable sample is laid on the floor and the center is marked and taken for making the very first winding with the diameter required.
- The rest of the cable is coiled by coiling each side separately

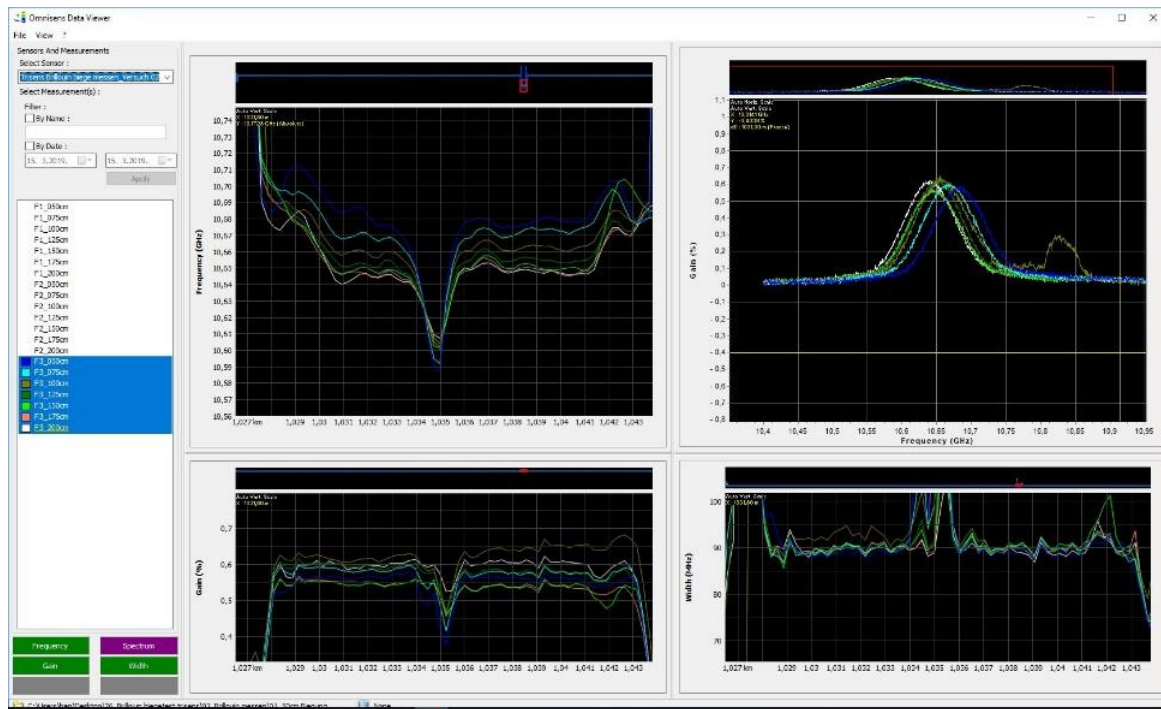
There is a very special event in the center of the Brillouin frequency peak measurement profile of the cable sample. It is the result of the cable twist in the first coil. The first coil is the cause of one additional effect – in the first twist the fibers exchange their azimuthal positions. What once was in the extension zone is now transferred to the compression zone, and vice versa. This is evident for all three fibers - with some difference due to inability to repeat the coiling process exactly in the same way with other diameters.



(a)



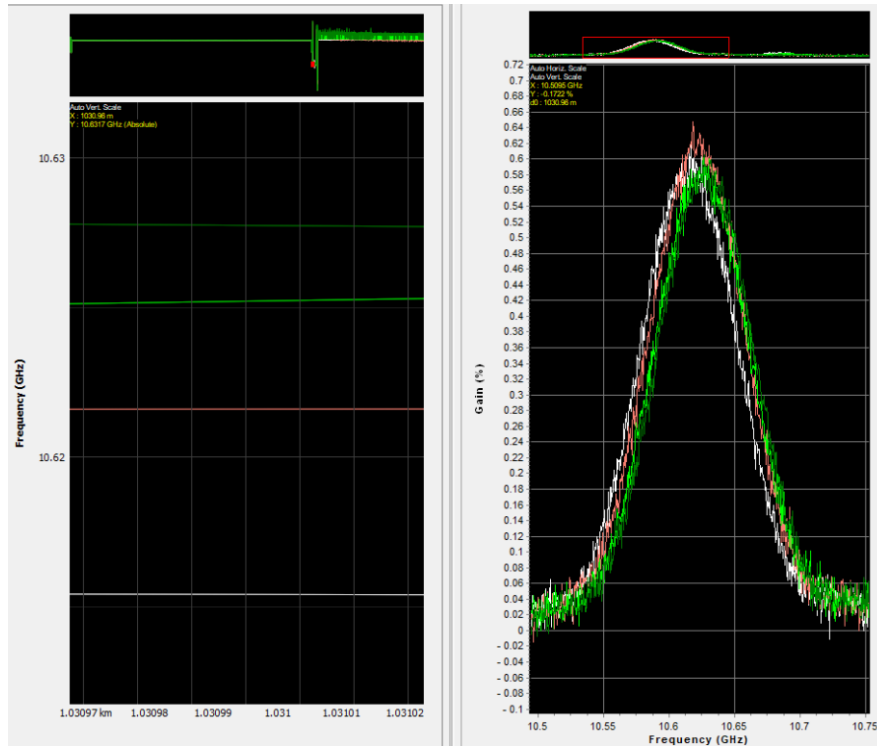
(b)



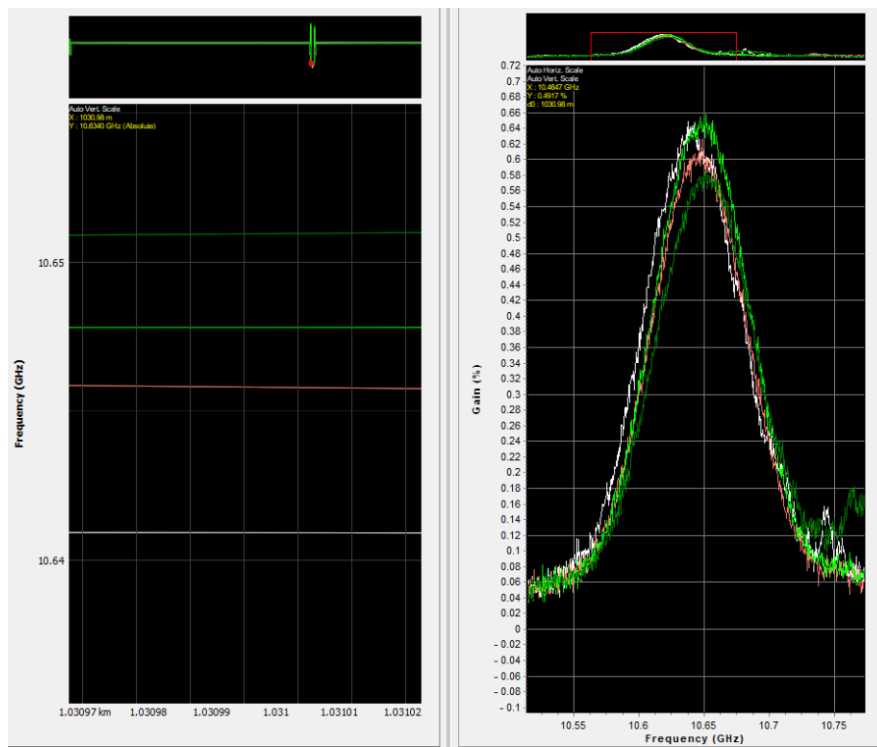
(c)

Figure 5.8: Visualized measurement results from all three fibers. The Brillouin-Lorentzian profile (“the bell”) can be seen in the upper-right picture. The rest of the pictures are a result of it; upper-left curve profiles movement of the peak, bottom-left shows gain and bottom-right shows width of Brillouin-Lorentzian profile; (a) fiber nr. 1, (b) fiber nr. 2 and (c) fiber nr. 3

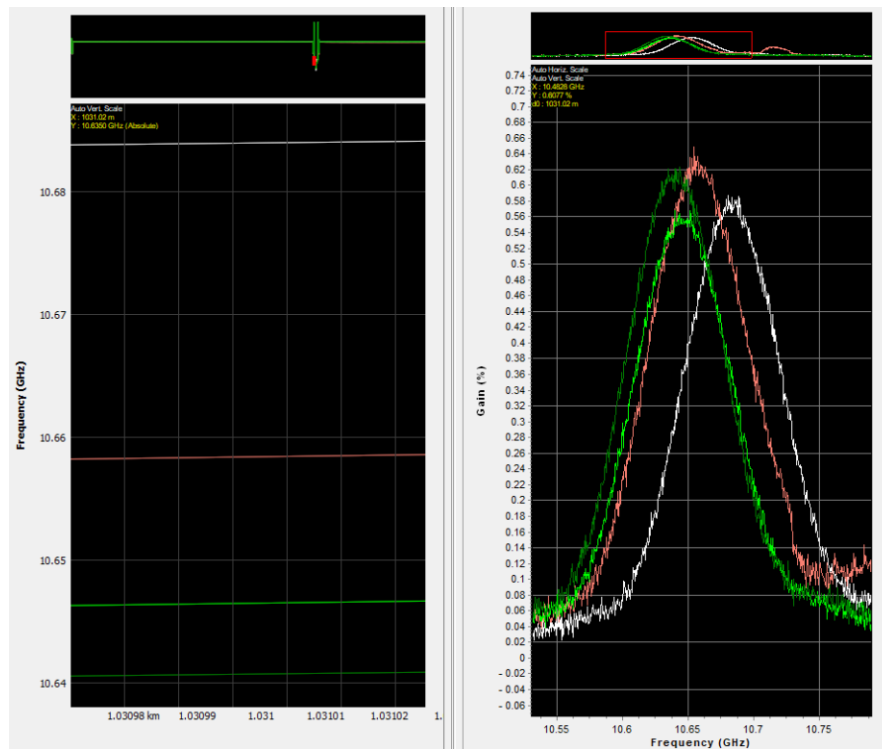
The changes in Brillouin-Lorentzian profiles due to change in diameters are clearly observed, especially the magnitude and direction of the shifts of Brillouin profile peaks. This change is different for different fibers. As an example, let’s consider location 1031m Fig.-5.9. with Table 5.3 giving quantitative information on the Brillouin peak shifts. The shifts vs. bending diameters summarized in Fig. 5.10. clearly show the opposite tendencies in Brillouin peak frequencies as a function of bending radius for the fibers. From Fig.-5.10 it can be concluded that the position of the fibers inside the sensing cable complies with Fig.-5.6a.



(a)



(b)



(c)

Figure 5.9: Brillouin profiles around the location 1031m for all three fibers; (a) Fiber-1, (b) Fiber-2 and (c) Fiber-3

It also makes sense to qualitatively compare these results with other perturbations to which the Brillouin peak shift is susceptible. These are strain and temperature. The relative shift for the coil with OD 50cm at the location 1031m is shown in Table 5.2, where the Brillouin profile for the 200cm bending is taken as a reference.

TABLE 5.2. BRILLOUIN PEAK FREQUENCY SHIFTS TRANSITION DUE TO BENDING AT THE LOCATION 1031M

Brillouin Peak/ Coil OD	200cm	150cm	100cm	50cm	Slope Sign
Fiber1	10.6277	10.6252	10.6216	10.6154	Negative
Fiber2	10.6509	10.6478	10.6458	10.6409	Negative
Fiber3	10.6405	10.6465	10.6585	10.6840	Positive

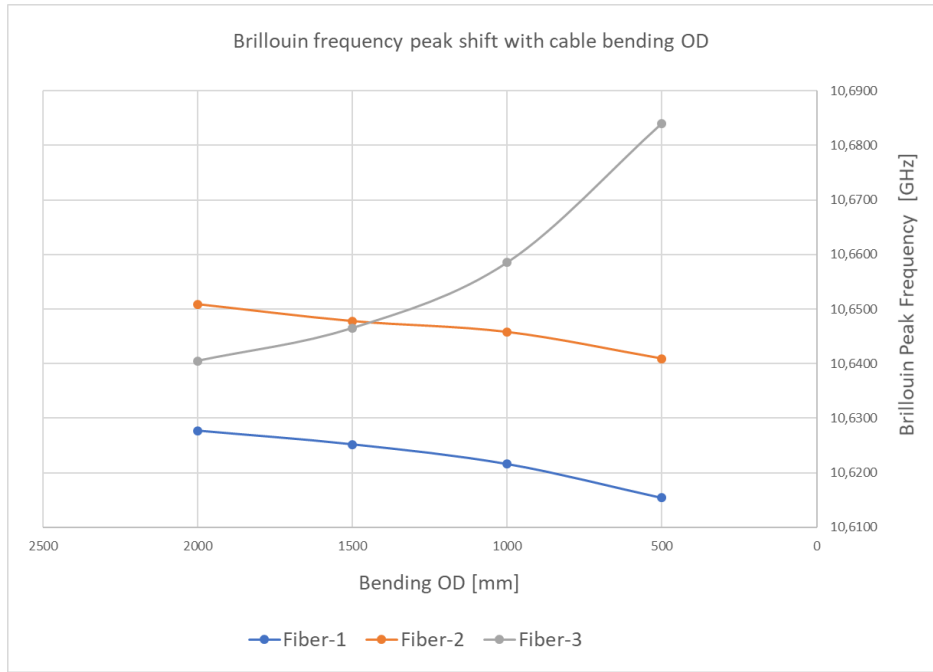


Figure 5.10: Brillouin frequency peak shift with bending at position 1031m

For the calculation of an equivalent reference, bare fiber sensitivity values of 0.05MHz/ $\mu\epsilon$ (500MHz/%) and 1MHz/ $^{\circ}\text{C}$ are used for strain and temperature, respectively.

$$\alpha \left(\frac{z}{\rho} - \frac{z}{\rho_{ref}} \right) = \Delta f$$

$$\underbrace{\alpha \left(1 - \frac{\rho}{\rho_{ref}} \right)}_{\alpha_{ref}} \frac{z}{\rho} = \Delta f$$

$$\alpha_{ref} \epsilon_r = \Delta f$$

$$\epsilon_r = \frac{1}{\alpha_{ref}} \Delta f$$

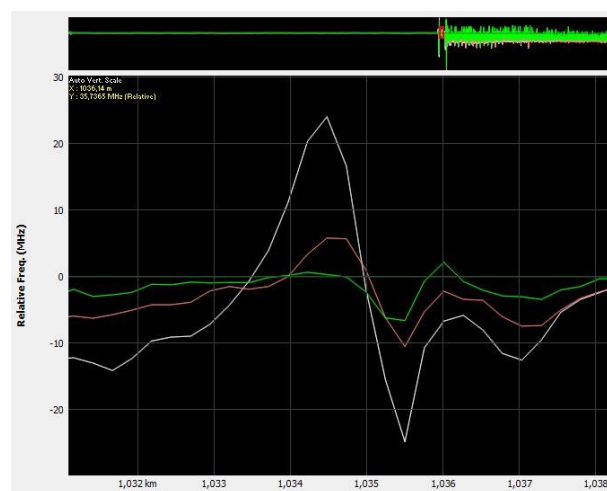
$$\alpha_{ref} = \frac{0.05\text{MHz}}{\mu\epsilon} \left(1 - \frac{0.5}{2} \right) = 0.0375 \frac{\text{MHz}}{\mu\epsilon}$$

Since the unit offers frequency scanning resolution of 100kHz (the Stokes wave) and maximum measurement accuracy of 2 $\mu\epsilon$, it now becomes clear that even much smaller bending diameters can be detected and measured.

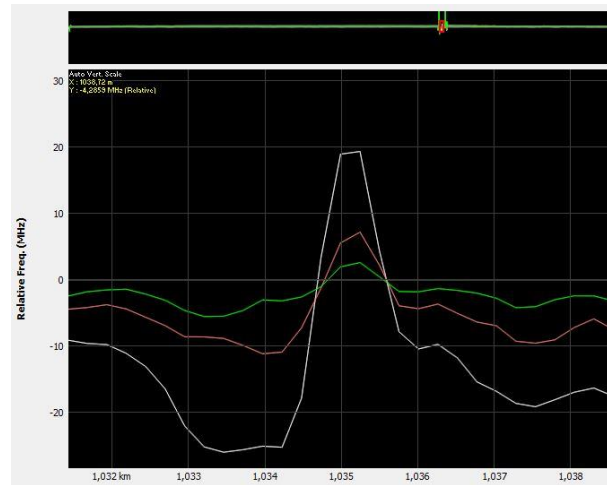
TABLE 5.3. RELATIVE FREQUENCY SHIFTS OF THE PEAK FOR THE COIL WITH OD 500MM TAKING OD 2000MCM AS A REFERENCE, AND EQUIVALENT SHIFTS OF STRAIN AND TEMPERATURE

Fiber nr.	Relative shift	Equivalent relative strain shift	Equivalent relative temperature shift
	[MHz]	[$\mu\epsilon$]	[$^{\circ}\text{C}$]
1	12,00	320,00	12,00
2	10,00	266,66	10,00
3	43,36	1156,26	43,36

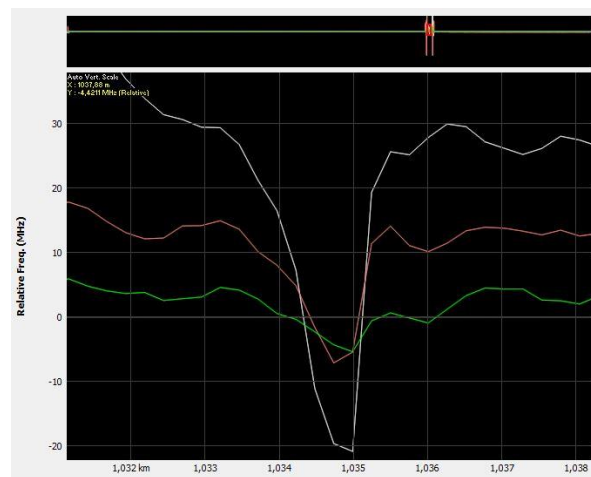
Comparing Table-5.1 and Table-5.3 and the dimensions of the cable from Fig.-5.5. discrepancy between the two can be noticed. For a given design, the relative strain in Table-5.3 is in magnitude much larger than the values listed in Table-5.1. For example, for a fiber with an outer diameter of $455\mu\text{m}$ to reach the strain magnitude of $867,20\mu\epsilon$ and taking measurement case with an outer diameter of 200cm as a reference, one must bend the cable more than of an outer diameter 50cm. This requires explanation. As already stated earlier, there is an event in the center of the sample in which the fibers make a transition from one zone to the other (Fig.-5.11). This transition is larger on smaller outer diameters, since the stress exerted to the fiber it larger. The white, red and green lines represent fibers that undergo bending of outer diameter of 50cm, 100cm and 150cm, respectively.



(a)



(b)



(c)

Figure 5.11: Transition of fibers from one strain zone to the opposite; white line OD 50cm, red line OD 100cm, green line OD 150cm, reference is OD 200cm; (a) fiber-1 (b) fiber-2 and (c) fiber-3

From the left side we can observe that with increasing frequencies on the ordinate axis, the order of the colors is the same for fibers 1 and 2 (white-red-green). For fiber 3 (Fig.-5.11c) it is just the opposite - the order is green-red-white. Each line slope reveals the reaction of the fiber to the twist. The stress increases or decreases depending whether the fibers are found in the extended or the compressed zone, just about before they change the zone in the center. The positive slope means stress on the fiber increases, while the negative slope means the fiber is compressed due to twist. This excessive stress that is added to the bending stresses is due to torsion. This effect peaks in the center where the color order is reversed in the center for a short length of 1m and then reversed again to its starting order. The reason for this is the twist

reaching a critical position in which fibers change zones. The total stress measured is the sum of bending and torsion stresses. From 5.10 we can calculate the bending induced relative elongation between OD 50cm and OD 200cm at amounts to $765\mu\epsilon$. The rest of the value measured $867,20\mu\epsilon$ belongs to the twist.

CONCLUSION

The cable design discussed in this thesis, with three tightly encapsulated optical fibers in a metal tubing with the outer diameter 1.22mm, is nowadays producible in relatively long lengths (presently 15km continuous length). Its linear strain characteristics is the reason for its adaptation and deployment into various geotechnical and geophysical, commercial and scientific applications for strain, temperature, acoustic, seismic and vibration measurements. In this thesis it was proven that the potential goes beyond these features and can now involve pressure and cable bending detection and measurement. It is not limited to one interrogation technique and can support all three categories: point-measurements, quasi-distributed, and fully fiber optic distributed interrogation techniques. Moreover, because it is based on three fibers, it has intrinsic capabilities for temperature compensation techniques required in many applications.

Within the very propulsive industrial discipline of fully distributed optical fiber measurement systems, providing data on temperature, strain, acoustic, seismic and vibration measurement, the missing piece still remains distributed optical fiber pressure sensing. There are two reasons for that: lack of adequate interrogation techniques and lack of adequate sensor cable. Although the fully distributed pressure interrogation techniques are proposed in the scientific community, their deployment in real applications, such as geophysical and geotechnical, are still limited. The reasons for this can be found on both sides; applications dealing with harsh conditions (high temperature ranges, hydrogen ingress problems in optical fibers, request on robust cable designs etc.), and interrogation techniques requiring very special optical fibers that are challenging to manufacture at industrial scales and to integrate into robust industrial cable designs. For that reason, two approaches were proposed in this thesis, both exploiting Stimulated Brillouin Scattering (SBS) effects and in particular a variation of the Brillouin gain.

SBS in optical fiber uses counter-propagating waves, the pump and the Stokes ones. It can be regarded as a heterodyne interferometric system with fully distributed passive interaction in each segment along the length of the fiber. The interaction takes place within a narrow wavelength range in which the change of the propagation constant is mostly dependent on the birefringence properties of the fiber, thus variation of the wavelength can be neglected. The interrogation methods proposed in this thesis exploit these possibilities. They are based on

investigation of the polarization efficiency of the SBS gain obtained from the Brillouin-Lorentzian gain profiles. It suggests using the standard BOTDA unit for performing measurements and it involves external passive manipulation of the Stokes wave at the input of the fiber loop. Polarization efficiency is dependent only on polarization parameters, propagation constant and phase differences among the pumping and the Stokes waves. Because of the cable design, the propagation constant is dependent mostly on external pressure only. Hence, all other external perturbations, including temperature and vibration, can make only indirect impact to the polarization efficiency through these parameters. The developments of such measurement strategies along with an appropriate calibration technique are crucial for its further industrial success and they are objectives of future research.

The industrial interests are obviously in one single cable design deployable in the field with single installation providing data for different measurands from multiple and independent distributed measurements. The multi-fiber cable design, proposed in this thesis, complies to these requirements. It is expected that further innovation in interrogation methods along with advances in optical fiber design together with precise production processes will offer even more features integrated in the small sized sensing cables. It can be said with good confidence - the cable concepts, as proposed in this thesis, will continue to be object of both academic and industrial research and will present a valuable asset toward cost-efficient digitalization of energy cables, large structures and linear assets in the near future.

REFERENCES

- [1] A. Rogers, "Distributed optical-fibre sensing," in Handbook of Optical Fibre Sensing Technology, J. M. Lopez-Higuera, Ed., chapter 14, John Wiley & Sons, New York, NY, USA, 2002.
- [2] Barrias A, Casas JR, Villalba S. "A Review of Distributed Optical Fiber Sensors for Civil Engineering Applications. *Sensors (Basel)*". May 23, 2016.
- [3] Bao X, Chen L. "Recent progress in distributed fiber optic sensors". *Sensors (Basel)*. 12(7):8601-39. doi: 10.3390/s120708601. Epub 2012 Jun 26.
- [4] Dakin, J.P., Pratt, D.J., Bibby, G.W., Ross, J.N.. „Distributed Optical Fibre Raman Temperature Sensor Using A Semiconductor Light Source And Detector“, *Electronics Letters*. 21. 569 - 570., 1985.
- [5] W. Hill, J. Kübler, M. Fromme, "Single-mode distributed temperature sensing using OFDR." Fourth European Workshop on Optical Fibre, SPIE Conference Proceedings (Vol. 7653, p. 765342). Porto, Portugal, September 8, 2010.
- [6] M.Niklès, L.Thévenaz, A. Fellay, M. Facchini, Ph.Robert, P. Salina, "A novel surveillance system for installed fiber optics cables using Brillouin interaction", *Proceedings IWCS '97*, pp. 658-664.
- [7] T.Horigushi, T.Karashima, M.Tateda, "A technique to measure distributed strain in optical fibers", *IEEE Photonics Technol. Lett.*, Vol.2, p 352, 1990.
- [8] X.Bao, J.Dhliwayo, N.Heron, D.J.Webb, D.A.Jackson, "Experimental and theoretical studies on a distributed temperature sensor based on Brillouin scattering", *IEEE J. Lightwave Technol.*, Vol. 13, p. 1340, 1995.
- [9] M.Niklès, L.Thévenaz, P. Salina, Ph.Robert, "Local Analysis of Stimulated Brillouin Interaction in installed fiber optics cables", *OFMC '96*, NIST Special Publication 905, pp.111-114.
- [10] Hong Cheng-Yu, Zhang Yi-Fan, Li Guo-Wei, Zhang Meng-Xi, Liu Zi-Xiong, "Recent progress of using Brillouin distributed fiber sensors for geotechnical health monitoring", *Sensors and Actuators* 2017.
- [11] Shatalin, S.V, Treschikov, V.N. and Rogers, A.J. „Interferometric optical time-domain reflectometry for distributed optical-fiber sensing“, *Applied Optics*, 37, 5600-5604, 1997.

- [12] Martens, S., T. Kempka, A. Liebscher, S. Lueth, and F. Möller, “Europe’s longest-operating on-shore CO₂ storage site at Ketzin, Germany: a progress report after three years of injection: Environmental Earth Sciences“, 67, no. 2, 323–334, 2012.
- [13] Marzetta, T. and M. Schoenberg, 1985, „Tube waves in cased boreholes: 55th Annual International Meeting“, SEG, Expanded Abstracts, 34–36
- [14] Mestayer, J., B. Cox, P. Wills, D. Kiyashchenko, J. Lopez, M. Costello, S. Bourne, G. Ugueto, R. Lupton, G. Solano, D. Hill, and A. Lewis, 2011, „Field trials of distributed acoustic sensing for geophysical monitoring“, 71st Annual International Meeting, SEG, Expanded Abstracts, <http://dx.doi.org/10.1190/1.3628095>.
- [15] LiosTech, <https://liostech.wordpress.com/tag/lios/page/3/>
- [16] NKT Photonics: <https://www.nktphotonics.com/lios/en/Sensornet>
- [17] Sesnornet: <https://www.sensornet.co.uk/>
- [18] Omnisens: <https://www.omnisens.com/index.html>
- [19] Febus Optics: <http://febus-optics.com/1/fr/frontpage/>
- [20] OZ Optics: https://www.ozoptics.com/products/fiber_optic_distributed.html
- [21] Neubrex Technologies: <http://www.neubrex.com/>
- [22] Silixa: <https://silixa.com/>
- [23] Fotech Solutions: <https://www.fotech.com/>
- [24] Optasense: <https://www.optasense.com/>
- [25] Rogers A. J.; 'Polarization-optical Time-domain Reflectometry: A New Technique for the Measurement of Field Distributions', 1981, Appl. Opt., Vol. 20, No. 6, pp 1060-1074.
- [26] John Redvers Clowes, “Fibre optic pressure sensor for downhole monitoring in the oil industry”, University of Southampton, Optoelectronic Research Center, Doctoral Thesis, 174pp, 2000.
- [27] Clowes, J.R. & Syngellakis, Stavros & Zervas, Michalis. (1998). „Pressure sensitivity of side-hole optical fiber sensors“. Photonics Technology Letters, IEEE. 10. 857 - 859. 10.1109/68.681509.

- [28] H. Xie, P. Dabkiewicz, R. Ulrich, and K. Okamoto, „Side-hole fiber for fiber-optic pressure sensing“, *Opt. Lett.* 11, 333-335 (1986).
- [29] Patent application WO2014082965; “Method for Locally Resolved Pressure Measurement”
- [30] Jansen, K & Dabkiewicz, Ph. (1987). „High Pressure Fiber-Optic Sensor with Side Hole Fiber“, *Proc SPIE.* 798. 56-60. 10.1117/12.941085.
- [31] A. Méndez and E. Diatzikis, "Fiber Optic Distributed Pressure Sensor Based on Brillouin Scattering," in *Optical Fiber Sensors, OSA Technical Digest (CD) (Optical Society of America, 2006)*, paper ThE46.
- [32] Yong Hyun Kim, Hong Kwon, Jeongjun Kim, and Kwang Yong Song, „Distributed measurement of hydrostatic pressure based on Brillouin dynamic grating in polarization maintaining fibers“, vol. 24, No. 19 | 19 Sep 2016 | *OPTICS EXPRESS* 21399
- [33] M.Niklès, L.Thévenaz, Ph.Robert, “Simple distributed fiber sensor based on Brillouin gain spectrum analysis”, *Optics Lett.*, Vol. 21, No. 10, p.758, 1996.
- [34] Luc Thevenasis, "Advanced Fiber Optics; Concepts and Technology," EPFL Press, 2011.
- [35] G. P. Agrawal, „Nonlinear Fiber Optics“, *Quantum Electronics -Principles and Applications*, Academic Press, Rochester, NY, USA, 1995.
- [36] Dennis Derickson; ‘Fiber Optic Test and Measurements’, Book, Prentice Hall 1998, ISBN 013-534330-5
- [37] Alan Rogers; ‘Polarization in Optical Fibers’, Book, Artech House Inc., ISBN-13: 978-1-58053-534-2
- [38] J. Neil Ross; 'Birefringence measurement in optical fibers by polarization-optical time-domain reflectometry', *Applied Optics*, Vol. 21, Issue 19, pp. 3489-3495, October 1982.
- [39] Smith, A M; ‘Birefringence induced by bends and twists in single-mode optical fiber’, *Applied Optics*, Vol. 19 Issue 15, pp.2606-2611 (1980)
- [40] Ulrich, R; Simon, A; 'Polarization optics of twisted single-mode fibers', *Applied Optics*, Vol. 18 Issue 13, pp.2241-2251 (1979)
- [41] Z.B. Ren, Ph. Robert, P. –A. Parrate; ‘Temperature dependence of bend- and twist-induced birefringence in a low-birefringence fiber’, *Optics Letters*, Vol. 13, No. 1, January 1988.

- [42] Thierry Chartier, Ammar Hideur, Cafer Özkul, Francois Sanchez and Guy M. Staphan; 'Measurement of singlemode optical fibers', OSA Applied Optics, Vol. 40, No. 30, October 2001.
- [43] Mendez and T.F. Morse; 'Specialty optical fibers handbook', Book, Academic Press, ISBN 13: 978-0-12-369406-5, 2007.
- [44] Shadaram, Mehdi; Hippenstiel, Ralph; 'Fourier analysis of the complex envelope of the echos in an OFDR', OSA Applied Optics, Vol. 25 Issue 7, pp.1083-1086, 1986.
- [45] Brian J. Soller, Dawn K. Gifford, Matthew S. Wolfe and Mark E. Froggatt; 'High resolution optical frequency domain reflectometry for characterization of components and assemblies', OSA Optics Express, Vol. 13, No. 2, 2005
- [46] Mehdi Shadaram, William L. Kuriger; "Using the optical frequency domain technique for the analysis of discrete and distributed reflections in an optical fiber", OSA Applied Optics, Vol. 23, No. 7, 1 April 1984
- [47] D. Garus, K. Krebber, F. Schliep, and T. Gogolla, "Distributed sensing technique based on Brillouin optical-fiber frequency-domain analysis," Optics Letters, vol. 21, no. 17, pp. 1402–1404, 1996.
- [48] D. Garus, T. Gogolla, K. Krebber, and F. Schliep, "Brillouin optical-fiber frequency-domain analysis for distributed temperature and strain measurements", Journal of Lightwave Technology, vol. 15, no. 4, pp. 654–662, 1997.
- [49] K. Y. Song, K. Lee, and S. B. Lee, "Tunable optical delays based on Brillouin dynamic grating in optical fibers," Optics Express, vol. 17, no. 12, pp. 10344–10349, 2009.
- [50] K. Y. Song, W. Zou, Z. He, and K. Hotate, "Optical time-domain measurement of Brillouin dynamic grating spectrum in a polarization-maintaining fiber", Optics Letters, vol. 34, no. 9, pp. 1381–1383, 2009.
- [51] J. M. Lopez-Higuera, L. Rodriguez Cobo, A. Quintela Incera, and A. Cobo, "Fiber optic sensors in structural health monitoring," Journal of Lightwave Technology, vol. 29, no. 4, pp. 587–608, 2011.
- [52] F. Bastianini, A. Rizzo, N. Galati, U. Deza, and A. Nanni, "Discontinuous Brillouin strain monitoring of small concrete bridges: comparison between near-to-surface and "smart" FRP fiber installation techniques," in Proceedings of the Smart Structures and Materials 2005: Sensors and Smart Structures Technologies for Civil, Mechanical, and Aerospace Systems (SPIE '05), pp. 612–623, March 2005.

- [53] Robert Boyd; "Nonlinear Optics", 3rd Edition, Academic Press, 2010., ISBN: 9780123694706
- [54] Torsten Gogolla and Katerina Kriebber, "Distributed Beat Length Measurement in Single-Mode Optical Fibers Using Stimulated Brillouin-Scattering and Frequency-Domain Analysis"; Journal of Lightwave Technology, Vol. 18, no. 3, March 2000.
- [55] M. Niklès, L. Thévenaz and P. Robert, "Brillouin gain spectrum characterization in single-mode optical fibers," J. Lightwave Technol., vol. 15, no. 10, pp. 1842-1851, 1997
- [56] A. Rogers, "Distributed optical-fibre sensors for the measurement of pressure, strain and temperature," Phys Rep, vol. 169, p. 99–143, 1988.
- [57] [A. Fellay, L. Thévenaz, M. Facchini, M. Niklès and P. Robert, "Distributed sensing using stimulated Brillouin scattering: Towards ultimate resolution," in Proc. 12th Opt. Fiber Sensors OSA Tech., vol. 16, pp. 324- 327, 1997.
- [58] T. Horiguchi, K. Shimizu, T. Kurashima and M. Tateda, "Development of a distributed sensing technique using Brillouin scattering," J. Lightwave Technol., vol. 13, no. 7, pp. 1296-1302, 1995.
- [59] X. Bao, A. Brown, M. DeMerchant and J. Smith, "Characterization of the Brillouin loss spectrum of single-mode fibers by use of very short (<10ns) pulses," Opt. Lett., vol. 24, no. 8, pp. 510-512, 1999.
- [60] A. Kobayakov, M. Sauer and D. Chowdhury, "Stimulated Brillouin scattering in optical fibers," Adv. Opt. Photonics, vol. 2, pp. 1-59, 2009.
- [61] A. Fellay, L. Thévenaz, M. Facchini, M. Niklès, P.A. Robert, "Distributed sensing using stimulated Brillouin scattering: toward ultimate resolution", Proc. of the 12th Conference on Optical Fiber Sensors, Williamsburg Virginia, p. 324-327 (1997).
- [62] Exfo OTDRs: <https://www.exfo.com/en/products/field-network-testing/otdr-iolm/>

BIOGRAPHY



General information:

Born: Male, December 1st 1972, Split - Croatia
Citizenship: Croatian
Residence: Fra Bone Razmilovića 7, HR-21000 Split, Croatia
Mob.: +385 91 201 4586
Email: petar.basic72@gmail.com

Professional experience:

Within his own consultancy company STE d.o.o. Petar Bašić is responsible for customer consultancies, proposition of solutions and organization of trainings and workshops on test and measurement concepts in the field of fiber optics for clients. Since 2010 he has been involved in the development of specialty fiber optic cables based on stainless steel tubing and specialty optical fibers for sensing and measurement purposes, as well as in the proposition, design and realization of testing facilities for specialty cable prototypes. He invented and introduced in the industry the Triple-Fiber-FIMT (Fiber-In-Metal-Tube) and the Triple-Stranded-Tubing concept for multipurpose fiber optic distributed measurements. He is involved in the proposition and completion of patent registration procedures, design, realization and application of specialty optical fibers, development of laboratory set-ups for R&D purposes and specialty measurements, as well as the processing and interpretation of results. From 1998 to 2006 he worked as a consultant and areas sales manager in the telecommunication industry for clients abroad with focus on fiber optic broadband communication systems and Fiber-To-The-Home projects. He was involved in the analysis of business models and roll-out plans, development of network infrastructure models based on customer's visions and business plans. He led trainings on network components, installation and measurements according to customers' requirements and organization of after sales activities.

Education

Faculty of Electrical Engineering and Computing, University of Zagreb

- 1997. Completion of undergraduate studies (Dipl. Eng. Degree)
- 2007. Completion of postgraduate studies (Master of Science Degree)

Personal information

Petar Bašić is happily married and father of three; two daughters and one son. His free time passions are fishing, diving and sailing.

Publications

Peer-reviewed journal articles:

- Petar Bašić, Rudolf Halmetschlager, “Fiber Optic Sensors Based on Hollow Capillary Tube with Three Tightly Encapsulated Optical Fibers”, *Automatika*, Vol. 60, No. 4, pp. 368-377, 2019.

Conference papers:

- Petar Bašić, “Fiber Optic Sensor Cable Based on Hollow Capillary Tube with Three Tightly Encapsulated Optical Fibers,” Proceedings of 2nd International Colloquium on Smart Grid Metrology, Split, Hrvatska, 9.-12. 04. 2019.
- Nino Rozić, Marin Despalatovic, Petar Bašić, Elis Sutlović, “Electric Machine Vibration Measurements Based on Fiber Optic Sensor Technology – Preliminary Results,” Proceedings of 2nd International Colloquium on Smart Grid Metrology, Split, Hrvatska, 9.-12. 04. 2019.
- Krešo Žmak, Zvonimir Šipuš, Petar Bašić, „A New Approach to Remote Fiber Testing in Optical Networks, “ Proceedings of the 17th International Conference on Applied Electromagnetics and Communications (ICECOM 2003), Dubrovnik, Hrvatska, 01-03.10.2003. pp. 278-281.

Patent applications:

- Rudolf Halmetschlager, Petar Bašić, “Method for Locally Resolved Pressure Measurement,” Patent application, Pub. No. WO2014082965, International App. No. PCT/EP2013/074627.

ŽIVOTOPIS

Opće informacije:

Datum rođenja: 01. prosinca 1972. god., Split
Državljanstvo: Hrvatsko
Adresa boravišta: Fra Bone Razmilovića 7, HR-21000 Split, Hrvatska
Mob.: +385 91 201 4586
E-pošta: petar.basic72@gmail.com

Profesionalno iskustvo:

U vlastitoj savjetodavnoj tvrtki STE d.o.o. Petar Bašić danas je zadužen za savjetovanje klijenata, predlaganje rješenja i organizaciju internih treninga i radionica za testne i mjerene koncepte iz područja optičkih vlakana za klijente. Od 2010. godine bavi se razvojem specijalnih svjetlovodnih kabela na bazi cijevi od nehrđajućeg čelika te specijalnim optičkim vlaknima za potrebe senzorskog i mjernog sustava, kao i predlaganjem, projektiranjem i realizaciji ispitnih postrojenja za specijalne kabele. On je izumio i uveo u industriju koncepte čelične cjevčice sa triju stiješnjenim optičkim vlaknima (Triple-Fiber-FIMT) kao i čelične cijevi s trima stiješnjenim spiralnim unutarnjim cjevčicama (Triple-Stranded-Tubes FIMT) za višenamjenska optička distribuirana mjerenja. Uključen je u predlaganje i dovršenje postupaka za registraciju patenta, projektiranje, realizaciju i primjenu specijalnih optičkih vlakana, razvoj laboratorijskih postavki za potrebe istraživanja i razvoja i specijalističkih mjerenja te obradu i interpretaciju rezultata. Od 1998. do 2006. radio je kao konzultant i voditelj prodaje u telekomunikacijskoj industriji za klijente u inozemstvu s fokusom na optičke širokopolasne komunikacijske sustave i projekte svjetlovod do doma (Fiber-To-The-Home). Sudjelovao je u analizi poslovnih modela i planova razvoja, razvoju modela mrežne infrastrukture na temelju vizija i poslovnih planova korisnika. Vodio je treninge o mrežnim komponentama, instalacijama i mjerenjima prema zahtjevima kupca i organizaciji poslije-prodajnih aktivnosti.

Obrazovanje:

Fakultet elektrotehnike i računarstva Sveučilišta u Zagrebu

- 1997. završio dodiplomski studij (dipl. inž.)
- 2007. završen poslijediplomski studij (magistar znanosti)

Personal information:

Petar Bašić je sretno oženjen i otac troje, dvije kćeri i jednog sina. Njegova strast su ribolov, ronjenje i jedrenje.